CYANIDE-BRIDGED POLYNUCLEAR COMPOUNDS OF MOLYBDENUM(III) AND RHENIUM(II)

A Dissertation

by

DAVID K. KEMPE

Submitted to the Office of Graduate and Professional Studies of
Texas A&M University
in partial fulfillment of the requirements for the degree of

DOCTOR OF PHILOSOPHY

Chair of Committee,	Kim R. Dunbar
Committee Members,	Timothy R. Hughbanks
	David P. Barondeau
	Joseph H. Ross, Jr.
Head of Department,	Simon W. North

August 2019

Major Subject: Chemistry

ABSTRACT

Since the discovery of $[Mn_{12}O_{12}(CH_3COO)_{16}(H_2O)_4]$, research in the area of molecular magnetism has been directed at designing single molecule magnets (SMMs) whose slow paramagnetic relaxation occurs with long relaxation times and at relatively high temperatures. Both polynuclear and mononuclear compounds have been studied with respect to the fundamental characteristics required to make SMMs viable options for device applications including memory storage, spintronics, and quantum computing. In recent years much progress has been made with respect to mononuclear magnets, but approaches that incorporate knowledge of strong anisotropy in exchange coupled systems are still underexplored. Specifically, anisotropic exchange represents an important option for improving the properties of polynuclear SMMs. Despite growing interest in the topic, lack of numerous examples of such systems have hampered progress in this area. This dissertation describes studies of new molecules and synthetic techniques to systematically study conditions that lead to Ising-type anisotropic exchange in heavier transition element molecules.

By drawing on previous work with the cyanometallate moieties $[Mo^{III}(CN)_7]^{4-}$ and $[(triphos)Re^{II}(CN)_3]^-$, new precursors and synthetic strategies were developed to aid research in the area of anisotropic exchange interactions. Mo-Ln chains with the formula $\{K[Ln(tmphen)_2(H_2O)_2Mo^{III}(CN)_7]\}$ were characterized structurally and magnetically, and revealed that more work could lead to interesting Mo-Ln nanomagnets. A cyanometallate wheel with the formula $[Mo^{III}(CN)_7]_6[Ni(L)]_{12}\cdot 24H_2O$ demonstrated that incorporating $[Mo^{III}(CN)_7]^{4-}$ into known architectures can improve magnetic properties. A new, heteroleptic Mo^{III} cyanometallate was isolated that will facilitate synthesis of new molecules. Three new compounds that incorporate Re^{II} and V^{II} demonstrate the requirements for observing anisotropic exchange with $[(triphos)Re^{II}(CN)_3]^-$. Future work with these strategies will be helpful for investigating the importance of anisotropic exchange as an alternative for the design of single molecule magnets with higher barriers for both the d and f-block elements.

ACKNOWLEDGEMENTS

I would like to thank Professor Kim Dunbar for providing me with the environment and resources to learn and grow for the last several years. I am tremendously grateful for the space, time, funding, and instruction that I have received from you that helped me develop as a person and a scientist.

I also want to express my thanks to my committee for their support of my research. Professors Tim Hughbanks, David Barondeau, Don Naugle, and Joe Ross, thank you for your time and effort to help me through this process.

Thank you to the Dunbar group for all the support over the years. It has been wonderful working alongside all of you and getting to know the members of this group, including undergraduate students, graduate students, postdocs, visiting scholars, and senior researchers. Thank you to everyone who mentored and supported me during my time here, and I wish you the best for your careers and lives!

Thanks to Professor Greg Powell for helping me my find my passion for science and encouraging me to go to graduate school. I appreciate the support and encouragement that I continue to get from you many years after I left your lab! Thanks for being an excellent mentor and role model.

Thank you to my friends and family (Kempe and Fullerton sides). I deeply appreciate the efforts that everyone made to support and encourage me. Special thanks to my parents, who have provided unconditional support for me over the years. I would not have made it without you.

Most of all, thank you to my wife, Becca, who has stood by me for every bit of this process. Your patience and understanding are incredible. I look forward to many more happy years together.

CONTRIBUTORS AND FUNDING SOURCES

This work was supervised by a dissertation committee consisting of my advisor Professor Kim Dunbar, and my committee members, Professor Timothy Hughbanks and Professor David Barondeau of the Department of Chemistry, and Professor Donald Naugle of the Department of Physics.

The computational studies in chapter 3 were completed by Dr. Kuduva R. Vignesh, of the Department of Chemistry.

All other work for the dissertation was completed by the student, under the advisement of Kim R. Dunbar of the Department of Chemistry.

This work was also made possible in part by the US Department of Energy under Grant Number DE-SC0012582 and the Robert A. Welch Foundation under Grant Number A-1449. Its contents are solely the responsibility of the authors and do not necessarily represent the official views of the US Department of Energy or the Welch Foundation.

TABLE OF CONTENTS

Page

ABSTRACT ii

ACKNOWLEDGEMENTS iv

CONTRIBUTORS AND FUNDING SOURCES vi

TABLE OF CONTENTS vii

LIST OF FIGURES ix

LIST OF TABLES xv

CHAPTER I INTRODUCTION 1

- Single Molecule Magnetism 1
- Cyanide Ligand and the Building Block Approach 9

CHAPTER II CYANIDE BRIDGED CHAINS OF LANTHANIDE AND MOLYBDENUM IONS 21

- Background 21
- Experimental Details 24
  - Synthesis 24
  - Infrared Spectroscopy 27
  - Crystallography 30
  - Magnetic measurements 43
- Conclusions and Future Studies 58

CHAPTER III PREPARATION AND REACTIONS OF SEVEN COORDINATE MOLYBDENUM(III) COMPOUNDS* 59

- Background 59
- Experimental Details 62
  - Synthesis 62
  - Crystallography 65
  - Cyclic Voltammetry 79
  - Magnetic Measurements 81
  - Infrared Spectroscopy 86

Calculations 87
Conclusions and Future Studies 93

CHAPTER IV COMPOUNDS CONTAINING ORBITALLY DEGENERATE RHENIUM(II) 95

Background 95
Experimental Details 97
Synthesis 97
Crystallography 99
Magnetic Measurements 110
Conclusions and Future Studies 119

CHAPTER V CONCLUSIONS AND FUTURE WORK 121

REFERENCES 124

LIST OF FIGURES

Page

Figure 1. Structure of the molecule $[Mn_{12}O_{12}(CH_3COO)_{16}(H_2O)_4]$ along the tetragonal axis (c axis). The manganese ions are reported as large grey spheres, oxygen in black, and carbon as small grey spheres. Only oxygen atoms of water molecules have been drawn for the sake of clarity. Reprinted with permission from reference 7, copyright 2006 Oxford University Press............2

Figure 2. Structure of $[(Cp^{iPr5})Dy(Cp^*)]^+$, the SMM with the highest known T_b to date, and the relaxation mechanism of the complex. Blue arrows show the most probable relaxation pathway, while red arrows show other pathways with non-negligible contributions. Adapted with permission from reference 13, copyright 2018 American Association for the Advancement of Science.....3

Figure 3. Hysteresis loops for various types of magnets. Reprinted with permission from reference 7, copyright 2006 Oxford University Press and reference 14, copyright 2001 John Wiley & Sons. 5

Figure 4. Structures of some notable molecules with large spin ground states. Left: structure of $[Mn^{III}_{12}Mn^{II}_7(\mu_4O)_8(\mu_3,\eta^1N_3)_8(L)_{12}(MeCN)_6]^{2+}$. Reprinted with permission from reference 14, copyright 2006 John Wiley & Sons. Right: structure of $[Mn(dpop)(H_2O)_2]_2[\{Mo(CN)_7\}_8\{Mn(dpop)\}_{10}\{Mn(dpop)(H_2O)\}_4]$. Reprinted with permission from reference 15, copyright 2010 John Wiley & Sons. 8

Figure 5. Depiction of the orthogonality principle in cyanide-bridged compounds. Top: symmetry allowed overlap leads to antiferromagnetic exchange due to paired spins. Bottom: orthogonal magnetic orbitals lead to ferromagnetic exchange. 11

Figure 6. Molecular structure of $[L_{NNN}CoGdCoL_{NNN}]^+$ with both a side and axial view. The red dashed line denotes the local anisotropy axis on Co, and the red and green arrows show the local magnetic moments on Co and Gd in one of the components of the ground state Kramer's doublet. Reprinted with permission from reference 27 Copyright 2013 American Chemical Society...12

Figure 7. Schematic diagram showing possible structures from reactions of a hexacyanometallate and a metal complex with a pentadentate blocking ligand. Note that the stoichiometry can, hypothetically, control the outcome of the reaction. Reprinted with permission from reference 32, copyright 2009 John Wiley & Sons. 14

Figure 8. Electronic structure of $[\mathrm{Mo^{III}(CN)_7}]^{4-}$: (a) 4d orbital energies in a D_{5h} pyramid, (b) energy spectrum of $\mathrm{Mo^{III}}$ in D_{5h} geometry, (c) energy spectrum of $\mathrm{Mo^{III}}$ in this geometry with spin-orbit coupling applied. The orbital composition of the ground $\varphi(\pm1/2)$ and excited $\chi(\pm1/2)$ Kramers doublets is shown, (d) the splitting of the 4d orbital energies in distorted complexes of $[\mathrm{Mo^{III}(CN)_7}]^{4-}$. Reprinted with permission from reference 28, copyright 2003 American Chemical Society...17

Figure 9. Structures of $[\mathrm{Mn(L_1)(H_2O)}]_2[\mathrm{Mo(CN)_7}]\cdot 2\mathrm{H_2O}$ and $[\mathrm{Mn(L_1)(H_2O)}]_2[\mathrm{Mn(L)}]_2\text{-}[\mathrm{Mo(CN)_7}]_2$. The red circle on the left shows the water molecules that can be removed by dehydration and the red arrows show the new coordination bonds that form because of that process. Reprinted with permission from reference 39, copyright 2017 Americal Chemical Society. 18

Figure 10. (a) structures of $\mathrm{L_{N5Me}}$, $\mathrm{L_{N3O2}}$, and $\mathrm{L_{DAPSC}}$ (b), (c), and (d) structures of each ligand incorporated in to a $\mathrm{Mn_2Mo}$ trinuclear compound. Reprinted with permission from reference 38, copyright 2013 American Chemical Society. 18

Figure 11. Left: Plot of $[\{\mathrm{MnCl}\}_4\{\mathrm{Re(triphos)(CN)_3}\}_4]$ with thermal ellipsoids drawn at the 25% probability level. Carbons in the phenyl rings of the triphos ligands are shown with arbitrary radius, and hydrogen atoms omitted for clarity. Reprinted with permission from reference 41, copyright 2007 American Chemical Society. Right: Z-axes of the local and molecular frames and the network of exchange pathways for the $\mathrm{Mn_4Re_4}$ cube. Reprinted with permission from reference 29, copyright 2007 Elsevier..........20

Figure 12. Structure of *catena*-$[\mathrm{Fe^{II}(ClO_4)_2\{Fe^{III}(bpca)_2\}}]\mathrm{ClO_4}$ and spin arrangment of the high-spin $\mathrm{Fe^{II}}$ and low-spin $\mathrm{Fe^{III}}$ centers contained therein. The $\mathrm{O_A}$ and $\mathrm{O_B}$ labels show the two different types of oxygen ligands for the high spin $\mathrm{Fe^{II}}$ centers. Reproduced with permission from reference 46, copyright 2005 American Chemical Society. 22

Figure 13. Thermal ellipsoid plots of $\{[\mathrm{Sm(tmphen)_2(H_2O)_2Fe(CN)_6}]\cdot\mathrm{MeOH}\cdot 13\mathrm{H_2O}\}_\infty$ (left) and $\{[\mathrm{Sm(tmphen)_2(H_2O)_2Cr(CN)_6}]\cdot\mathrm{MeOH}\cdot 9\mathrm{H_2O}\}_\infty$ (right) drawn at the 50% probability level. The atoms from solvent molecules have been omitted for the sake of clarity. Reproduced with permission from reference 66, copyright 2007 Royal Society of Chemistry...24

Figure 14. IR spectrum for 1. The peaks at 2098 and 2048 are typical for bridging and terminal cyanide ligands, respectively. The features from 1700-1500 are attributed to the aromatic tmphen ligands. 27

Figure 15. IR spectrum for 2. The peaks at 2110 and 2046 are typical for bridging and terminal cyanide ligands, respectively. The features from 1700-1500 are attributed to the aromatic tmphen ligands. 28

Figure 16. IR spectrum for 3. The peaks from 2120-2033 are typical for bridging and terminal cyanide ligands, respectively. The features from 1700-1500 are attributed to the aromatic tmphen ligands. 28

Figure 17. IR spectrum for 4. The peaks at 2098 and 2048 are typical for bridging and terminal cyanide ligands, respectively. The features from 1700-1500 are attributed to the aromatic tmphen ligands. 29

Figure 18. IR spectrum for 5. The peaks at 2109 and 2097 are typical for bridging and terminal cyanide ligands, respectively. The features from 1700-1500 are attributed to the aromatic tmphen ligands. 29

Figure 19. Repeating unit of 1. Only the major component of the $\{Mo(CN)_7\}$ fragment is shown. Hydrogen atoms are omitted for clarity. Ellipsoids drawn at the 50% probability level. 33

Figure 20. Asymmetric unit of 2. Only the major component of the $\{Mo(CN)_7\}$ fragment is shown. Hydrogen atoms are omitted for clarity. Ellipsoids drawn at the 50% probability level. 35

Figure 21. Asymmetric unit of 3. Only the major component of the $\{Mo(CN)_7\}$ fragment is shown. Hydrogen atoms are omitted for clarity. Ellipsoids drawn at the 50% probability level. 35

Figure 22. Asymmetric unit of 4. Only the major component of the $\{Mo(CN)_7\}$ fragment is shown. Hydrogen atoms are omitted for clarity. Ellipsoids drawn at the 50% probability level. 38

Figure 23. Asymmetric unit of 5. Only the major component of $\{Mo(CN)_7\}$ is shown. Hydrogen atoms are omitted for clarity. Ellipsoids drawn at the 50% probability level. 40

Figure 24. Magnetic susceptibility data of 1...44

Figure 25. Reduced magnetization plot for 1 with applied fields of 1-7 T in the 2-4 K range. 44

Figure 26. In-phase and out-of-phase susceptibility data for 1, measured at 2 K with applied static DC fields from 0-2000 Oe...45

Figure 27. Magnetic susceptibility data of 2...47

Figure 28. Reduced magnetization plot for 2 with applied fields of 1-7 T in the 2-4 K range. 47

Figure 29. In-phase and out-of-phase susceptibility data for 2, measured at 2 K with applied static DC fields from 0-2000 Oe. 48

Figure 30. Magnetic susceptibility data of 3 50

Figure 31. Reduced magnetization plot for 3 with applied fields of 1-7 T in the 2-4 K range. 50

Figure 32. In-phase and out-of-phase susceptibility data for 3, measured at 2 K with applied static DC fields from 0-2000 Oe. 51

Figure 33. Magnetic susceptibility data of 4 53

Figure 34. Reduced magnetization plot for 4 with applied fields of 1-7 T in the 2-4 K range. 53

Figure 35. In-phase and out-of-phase susceptibility data for 4, measured at 2 K with applied static DC fields from 0-2000 Oe. 54

Figure 36. Magnetic susceptibility data of 5 56

Figure 37. Reduced magnetization plot for 5 with applied fields of 1-7 T in the 2-4 K range. 56

Figure 38. In-phase and out-of-phase susceptibility data for 5, measured at 2 K with applied static DC fields from 0-2000 Oe. 57

Figure 39. Local geometry of the molybdenum atoms in 7 (Mo1, Mo2, and Mo3 left to right). 67

Figure 40. Structure of 7. The nickel atoms are green, molybdenum atoms are teal, carbon atoms are grey, nitrogen atoms are blue, and oxygen atoms are red. Hydrogen atoms are omitted for the sake of clarity. 68

Figure 41. Crystal structure of 9. Ellipsoids are drawn at the 50% probability level. 72

Figure 42. Crystal structure of 10. Only one configuration of the disordered $[NEt_4]^+$ is shown. Ellipsoids are drawn at the 50% probability level. 74

Figure 43. Two views of the two $[Mo^{III}(DAPB)(CN)_2]^-$ fragments in the unit cell of 11. The ellipsoids are drawn the 50% probability level. 77

Figure 44. Cyclic voltammograms of 9 in CH_2Cl_2 (DCM). 80

Figure 45. Magnetic susceptibility plots of 7 (black dots) and 8 (red dots).....................83

Figure 46. 1.8K magnetization data for 7. The solid black line is a guide for the eyes...84

Figure 47. Reduced magnetization data for 7. Solid lines are a guide for the eye...........84

Figure 48. In-phase and out-of-phase susceptibility data for 7, measured at 2 K with applied static DC fields from 0-2000 Oe...85

Figure 49. IR spectra for 7 and 8. Large peaks at 2900, 1460, and 1377 are from the Nujol® used in the mull. The lower spectrum is zoomed in on the cyanide stretching region...86

Figure 50. One-half of the 7 complex, depicted above, was used for DFT calculations to compute the exchange interactions. 89

Figure 51. CASSCF computed d-orbital ordering for Mo^{III} ions in 7............................90

Figure 52. The two Ni centers $\{Ni(CN)_2\}$ (left) and $\{Ni(CN)(H_2O)\}$ (right) used for CASSCF calculations. 91

Figure 53. CASSCF-computed d-orbital ordering for Ni^{II} ions in 7..............................91

Figure 54. Plot of the asymmetric unit in 12. Ellipses are drawn at the 50% probability level. 101

Figure 55. Full molecule of 12. Ligands are drawn in a wireframe mode to emphasize the structure of the cyanide-bridged core. 101

Figure 56. Plot of the asymmetric unit in 13. Ellipses are drawn at the 50% probability level. 104

Figure 57. Full molecule of 13. Ligands are drawn in a wireframe mode to emphasize the structure of the cyanide and oxide-bridged core. 104

Figure 58. Thermal ellipsoids drawn at the 50% probability level and wireframe model of 14. 108

Figure 59. Magnetic susceptibility plot of 12 from 300 K – 2 K in an applied field of 1000 Oe..112

Figure 60. Magnetization data at 1.8 K of 12 at fields up to 7 T (70,000 Oe). 112

Figure 61. Reduced magnetization data for 12. Solid lines are a guide for the eye.......114

Figure 62. In-phase and out-of-phase susceptibility data for 12, measured at 2 K with applied static DC fields from 0-2000 Oe. 115

Figure 63. Magnetic susceptibility data for 13 from 300 K – 2K with an applied field of 1000 Oe. 117

Figure 64. Magnetization data at 1.8 K for 13 at fields up to 7 T................................117

Figure 65. In-phase and out-of-phase susceptibility data for 13, measured at 2 K with applied static DC fields from 0-2000 Oe. 118

Figure 66. Reduced magnetization data for 13. Solid lines are a guide for the eye.......119

LIST OF TABLES

Page

Table 1. Crystal data and structure refinement for 1..32

Table 2. Crystal data and structure refinement for 2..36

Table 3. Crystal data and structure refinement for 3..37

Table 4. Crystal data and structure refinement for 4..39

Table 5. Crystal data and structure refinement for 5..41

Table 6. Selected bond lengths and angles for the LnMo chains. All distances are given in Å and angles are given in degrees (°). 42

Table 7. SHAPE results for crystallographically independent Mo^{III} centers in 7...........67

Table 8. Crystal data and structure refinement for 7..69

Table 9. Comparison of the unit cell parameters for 7 and 8...70

Table 10. Crystal data and structure refinement for 8..71

Table 11. Crystal data and structure refinement for 9..73

Table 12. Crystal data and structure refinement for 10..75

Table 13. Crystal data and structure refinement for 11..78

Table 14. Comparison of bond angles of Mo with the chelating ligand DAPB. The O-Mo-O angles are wider in each case, but the angles are generally close to the ideal for a pentagonal bipyramid (72°)...79

Table 15. Different spin configurations employed for extracting *J* values and its corresponding energies from DFT calcualtions in 7. Black arrows denote “spin-up” and red arrows denote “spin-down.” 90

Table 16. Values of g, *D* (in cm^{-1}) and *E/D* values for both Ni and Mo centers in 7 computed from *ab initio* CASSCF calculations...92

Table 17. CASSCF computed energies (cm^{-1}) and contributions to the *D* value from the first four excited states for Ni^{II} ions in complex 7....................................92

Table 18. Crystal data and structure refinement for 12. 102

Table 19. Crystal data and structure refinement for 13. 105

Table 20. V-L bond distances for compound 14. 108

Table 21. Crystal data and structure refinement for 14. 109

CHAPTER I

INTRODUCTION

Single Molecule Magnetism

In the 21st century, research into the potential applications of nanotechnology, including new types of nanomaterials, has exploded. Molecular magnets have attracted considerable interest from both chemists and physicists since 1993, when single molecule magnet (SMM) behavior was discovered in $[Mn_{12}O_{12}(CH_3COO)_{16}(H_2O)_4]$ (Figure 1).[1-2] The structure – first reported in 1980 – is interesting due to the arrangement of Mn^{IV} and Mn^{III} ions, with four Mn^{IV} atoms comprising a cubane-like structure in the core surrounded by the eight acetate-bridged Mn^{III} ions in the outer ring. At the time of publication, Lis predicted that if there was significant magnetic communication between the twelve manganese centers in the molecule, the magnetic properties would prove to be interesting. However, further development would have to wait more than a decade. In 1991, EPR and magnetization studies performed by Gatteschi and coworkers corroborated that $[Mn_{12}O_{12}(CH_3COO)_{16}(H_2O)_4]$ has an $S = 10$ ground state and that the sign of the zero-field splitting term, D, is negative.[3] In the same work, AC susceptibility measurements were also performed and it was determined that the out of phase component of the AC susceptibility was frequency dependent, which was previously seen in spin glasses and superparamagnets but had never been observed in a molecular system. Two years later, in 1993, additional work cemented the molecular origin of the phenomenon in $[Mn_{12}O_{12}(CH_3COO)_{16}(H_2O)_4]$.[4-5] In particular, the discovery of magnetic hysteresis,

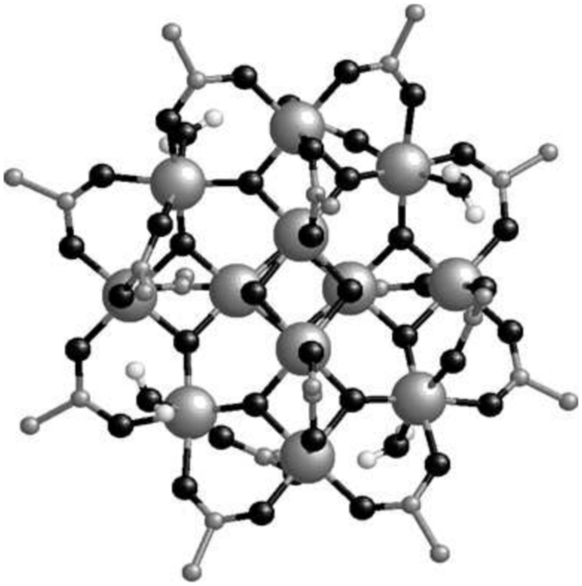

Figure 1. Structure of the molecule $[Mn_{12}O_{12}(CH_3COO)_{16}(H_2O)_4]$ along the tetragonal axis (c axis). The manganese ions are reported as large grey spheres, oxygen in black, and carbon as small grey spheres. Only oxygen atoms of water molecules have been drawn for the sake of clarity. Reprinted with permission from reference 7, copyright 2006 Oxford University Press.

complete with steps, was convincing evidence that the origin of the effect was molecular in nature. The ability to induce magnetic memory effects in a single molecule was, at the time, unprecedented. These materials, along with single-chain magnets (SCMs), are potentially useful for applications where their small size and magnetic properties could lead to novel uses, such as spin carriers in spintronic devices and quantum computers.[6-12] The problem with including SMMs or SCMs in devices is that their most interesting property, magnetic memory, only expresses itself at very low temperatures. The blocking temperature, T_b, is a value that researchers have used to help compare the molecular

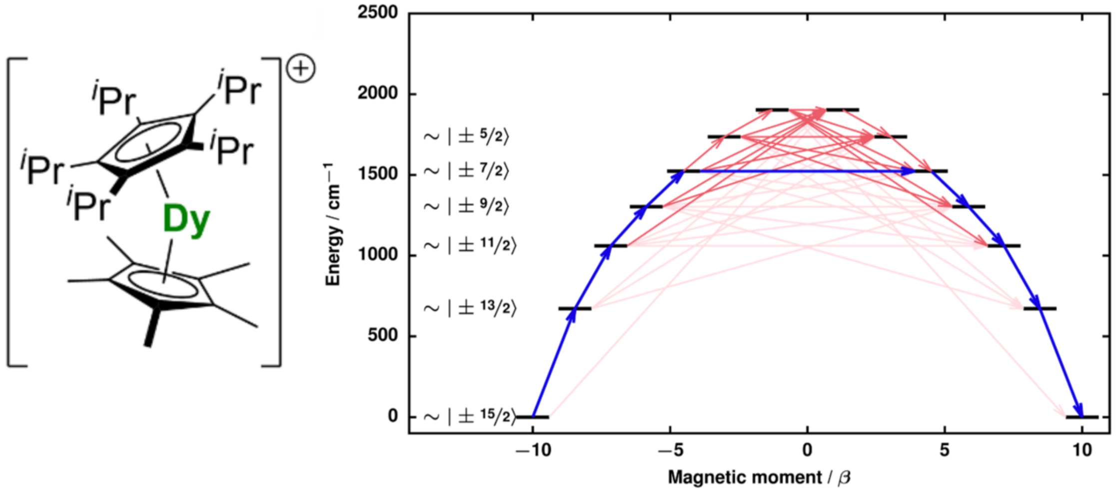

Figure 2. Structure of [(Cp^{iPr5})Dy(Cp*)]$^+$, the SMM with the highest known T_b to date, and the relaxation mechanism of the complex. Blue arrows show the most probable relaxation pathway, while red arrows show other pathways with non-negligible contributions. Adapted with permission from reference 13, copyright 2018 American Association for the Advancement of Science.

magnets by quantifying the magnetic memory effect. T_b defined as either the highest observed temperature for magnetic hysteresis or the temperature at which the magnetic relaxation time, τ, equals 100s for a particular SMM.[7] The T_b value is ~4K for Mn$_{12}$-acetate[1] and 80K for the current record-holding molecule, [(Cp^{iPr5})Dy(Cp*)]$^+$ (Cp^{iPr5} = penta-iso-propylcyclopentadienyl, Cp* = pentamethylcyclopentadienyl).[13] Also shown in Figure 2 are the relaxation pathways that constitute the barrier to reversal of the magnetization in [(Cp^{iPr5})Dy(Cp*)]$^+$. This barrier between the spin pointing up or pointing down is the key characteristic that allows molecules to function as SMMs. While classical magnets also have barriers to reversal of the magnetization, the origin of that barrier is different for SMMs. To help explain that difference, it is helpful to make a side-by-side comparison of classical magnets and SMMs.

In a typical bulk magnet, the spins are organized into magnetic domains, areas where the spins are aligned along a common axis. Domain walls – areas where the spins are intermediate between two domains – split the domains within this material, but the walls themselves have a finite thickness. When a sufficient field is applied, the domain that aligns with that field grows (by moving the domain walls) until it dominates the majority of the magnet's area, giving rise to the net magnetic moment of the material. One of the key measurements that can be used to verify the existence of magnetic memory is the measurement of magnetic hysteresis. In this measurement, the sample is placed in a magnetic field that is swept positive to negative and back along a single direction. In materials that exhibit magnetic memory, the material will stay magnetized even when there is no applied field. In bulk magnets, there can be steps in the hysteresis loop as domain walls change size and move to minimize the magnetic energy in the sample (Figure 3).[7,14] When the particle is so small that it can no longer accommodate domain walls, the entire particle adopts a single domain. For these "single domain particles," hysteresis loops do not have well-pronounced steps because the spins are compelled to flip as a unit or not at all. As shown in Figure 3, SMMs also exhibit magnetic hysteresis.

The origin of the magnetic behavior in SMMs, however, is distinct from that of classic magnets. Magnetic memory arises because of an energy barrier to

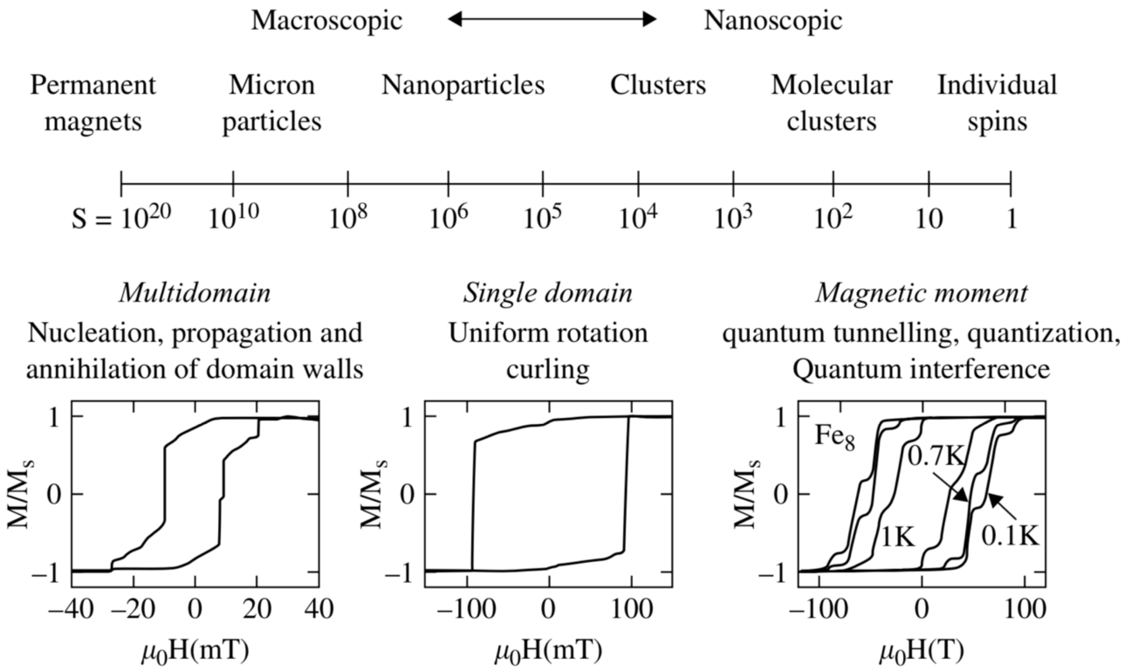

Figure 3. Hysteresis loops for various types of magnets. Reprinted with permission from reference 7, copyright 2006 Oxford University Press and reference 14, copyright 2001 John Wiley & Sons.

reversal of the magnetization. In bulk magnets, that energy barrier is linked to the large number of spins that communicate with each other in the material. In both multidomain and single domain magnets, cooperativity is key to understanding the data. Each spin has a local magnetic field that exerts magnetic force on its neighbors, making alignment of their magnetic axes energetically favorable. These interactions between spins are the origin of the barrier to reversal of the magnetization. But in SMMs, each molecular spin carrier has magnetic anisotropy that arises from its own electronic environment, meaning that they have a fundamentally different origin to their magnetic behavior than classical magnets. As seen in Figure 3, there are steps in the hysteresis loops of SMMs; these steps imply that the magnets can flip independently of each other. While single domain particles are compelled to act as a unit due to the lack of domain walls, SMMs have no such restriction. Rather than originating from the cooperativity between spin carriers, the barrier in most transition metal SMMs such as $[Mn_{12}O_{12}(CH_3COO)_{16}(H_2O)_4]$ (those that have only quenched or second order spin-orbit coupling) is defined as $U = S^2|D|$ or $U = \frac{1}{2}S^2|D|$ for integer and half-integer spin systems, respectively, where S is the ground state spin and D is the axial zero-field splitting parameter. The parameter D typically has a negative value in SMMs. A negative value of D imparts axial anisotropy to the magnetic moment, giving it a directional bias along one axis. The energy barrier responsible for the magnetic memory effect is a barrier between the moment pointing up or down along that easy axis. So, in SMMs, the origin of the barrier is present in each and every SMM, rather than being a result of the collection of spin carriers. Each spin carrier has local anisotropy and its own spin that can respond independently to the environment. While this fundamental difference in the origin of magnetic behavior is interesting, the low temperature necessary to observe this behavior imposes a significant restriction on implementation of SMMs in technological applications. As mentioned above, the record T_b for molecular magnets remains 80 K, barely higher than the boiling temperature of liquid nitrogen. Finding molecules with higher T_b would help propel research forward in this area.

There are three main parameters that help researchers compare SMMs: T_b - which was mentioned above, U - the theoretical size of the barrier to reversal of magnetization, and U_{eff} - the observed barrier to reversal of the magnetization. U_{eff} is always smaller than

U in SMMs. SMMs typically do not perform as well as the parameter U would suggest because U does not adequately address the full complexity of magnetic relaxation in nanomagnets. U describes what is known as the “thermal barrier” to relaxation of the magnetization, but there are other mechanisms by which SMMs can reverse their magnetization. One of the most significant of these is quantum tunneling of the magnetization (QTM), which limits the performance of SMMs by allowing spins to tunnel through the barrier. This can happen only when a pair of degenerate states, one of each side of the barrier, exists so that the magnetization can tunnel between the two. The phenomenon of quantum tunneling explains why “steps” exist in the hysteresis loops of SMMs; only some magnetic fields meet the requisite conditions for tunneling to occur. Quantum tunneling and other non-thermal relaxation mechanisms result in a measured U_{eff} that is lower than U. Nonetheless, efforts to increase the barrier height have been a major focus in the field of nanomagnets. Because of the exponential dependence of the barrier on *S*, early research focused on making large molecules with the largest ground spin state possible. The molecule with the largest spin ground state known to date is $[Mn^{III}_{12}Mn^{II}_{7}(\mu_4O)_8(\mu_3,\eta^1N_3)_8(L)_{12}(MeCN)_6]Cl_2\cdot 10MeOH\cdot MeCN$ (L = 2,6-bis-(hydroxy-methyl)-4-methylphenol) with a $S = 83/2$.[15] The largest spin ground state for a cyanide-bridged molecule is $S = 31$, held by the molecule $[Mn(dpop)(H_2O)_2]_2$-$[\{Mo(CN)_7\}_8\{Mn(dpop)\}_{10}\{Mn(dpop)(H_2O)\}_4]\cdot xH_2O$ (dpop = 2,13-dimethyl-3,6,9,12,18-pentaazabicyclo-[12.3.1]octadeca-1(18),2,12,14,16-pentaene) prepared in the Dunbar group (Figure 4).[16] Despite the impressive *S* values for such molecules, neither of these two molecules exhibit SMM behavior. A paper published by Oliver Waldmann

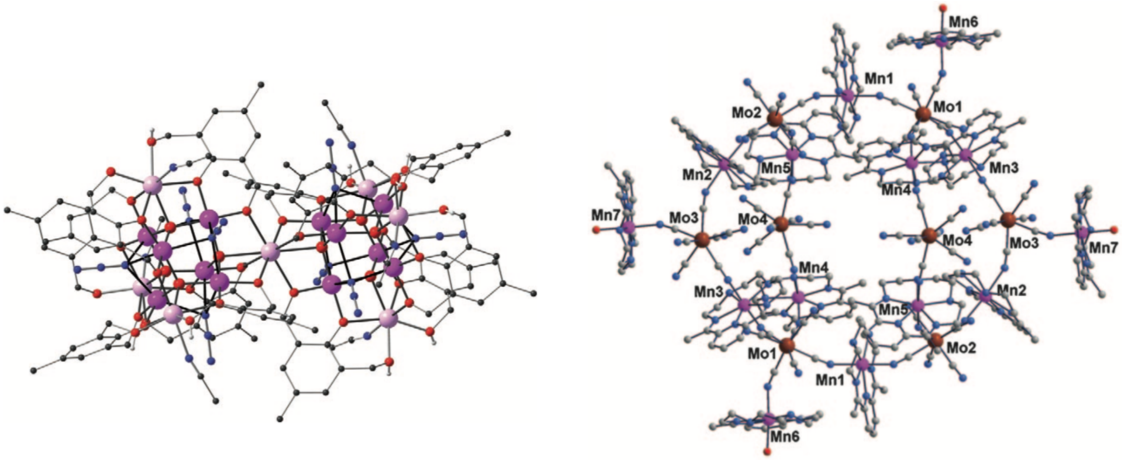

Figure 4. Structures of some notable molecules with large spin ground states. Left: structure of $[\mathrm{Mn^{III}}_{12}\mathrm{Mn^{II}}_{7}(\mu_4\mathrm{O})_8(\mu_3,\eta^1\mathrm{N}_3)_8(\mathrm{L})_{12}(\mathrm{MeCN})_6]^{2+}$. Reprinted with permission from reference 14, copyright 2006 John Wiley & Sons. Right: structure of $[\mathrm{Mn(dpop)(H_2O)_2}]_2[\{\mathrm{Mo(CN)_7}\}_8\{\mathrm{Mn(dpop)}\}_{10}\{\mathrm{Mn(dpop)(H_2O)}\}_4]$. Reprinted with permission from reference 15, copyright 2010 John Wiley & Sons.

explains why maximizing *S* is not a generally successful strategy for making high temperature SMMs.[17] *D* and *S* are not truly independent variables; *D* is inversely proportional to *S* so that U_{eff}, the observed barrier, is proportional to S^0. Waldmann notes that researchers who focused on increasing the value of *D* were seeing more success in raising T_b, which helped shift the focus of the field. Later, a groundbreaking paper from the Ruiz research group elucidated the origin of *D* and extrapolated their prediction to all first-row transition metals.[18] There has been incredible progress in this line of work from synthetic groups and computational groups, leading to new transition metal magnets that outperform the earliest examples.[19-20] However, the predictions by Ruiz and coworkers are limited to first-row transition metals. The story is more complicated for metal centers with significant spin-orbit coupling, such as heavier transition metals and f-block metals.

The anisotropy in compounds with these heavy metals can no longer be properly described by *S* and *D*; they have first order spin-orbit coupling such that spin is no longer a good quantum number, so the magnetic states are better described in terms of M_J levels.[21] Much of the recent work in the field focused on lanthanides, which have significant spin-orbit coupling, complicating the interpretation of their magnetic properties.[22] The shift to lanthanide chemistry, though, does extend and improve the work on mononuclear SMMs, since a single lanthanide center often has significantly improved magnetic properties than a single transition metal center. Most record-holding compounds are lanthanide based, and many have only one metal center. Research into polynuclear compounds, however, could provide new insights into how to build high temperature SMMs that may be suitable for technological applications. In this work, particular attention will be paid to polynuclear structures bridged by cyanide.

Cyanide Ligand and the Building Block Approach

One ligand that has a long history of mediating relatively strong and predictable exchange between metal centers is cyanide. As a result, cyanide-bridged materials have been a staple of molecular magnetism almost since its inception. Some of the most impressive extended networks in magnetism are Prussian Blue analogues, which are infinite networks composed of divalent and trivalent metal centers bridged by cyanide. Arguably the most impressive compound of this type, $V^{II}[Cr^{III}(CN)_6]_{0.86}\cdot 2.8\ H_2O$, exhibits magnetic ordering above room temperature.[23] In order to utilize these properties for applications, it is necessary to understand them at a basic level. The spin Hamiltonian proposed by Heisenberg, Dirac, and Van Vleck is the Hamiltonian that we still use today to understand most coupling between two metal centers:

$$(1)\ \mathcal{H} = -2JS_{\mathrm{M}}S_{\mathrm{M'}}$$

where J is the magnitude of the magnetic interaction between the two spins S_{M} and $S_{\mathrm{M'}}$. When J is positive, the coupling is ferromagnetic (the spins align parallel to each other) and when J is negative, the coupling is antiferromagnetic (the spins align antiparallel to each other). Larger J values necessarily mean that the energy gap between magnetic states is larger i.e. the interaction is stronger between those spins. Cyanide mediates this coupling because its orbitals overlap with the magnetic orbitals on S_{M} and $S_{\mathrm{M'}}$. This phenomenon is known as superexchange in cases where the bridging ligand is diamagnetic.[24-25] When the symmetry of the magnetic orbitals is such that they can mix with the same orbital on the CN^- ligand, this results in antiferromagnetic exchange. If the mixing is symmetry forbidden, then the result is ferromagnetic coupling (Figure 5). These simple rules, known generally as the "Goodenough-Kanamori rules" can be used to rationalize superexchange and are particularly effective in the case of cyanide-bridged complexes. In large compounds, the complexity of the Hamiltonian increases as a function of the number of magnetic centers:

$$(2)\ \mathcal{H} = \Sigma[-2J_{ij}(S_{\mathrm{M}})_i(S_{\mathrm{M'}})_j]$$

However, the symmetry of the structure often simplifies the expression, in practice. For metal pairs that are symmetry equivalent, the same J is often used to describe the coupling between those pairs. Large values of J lead to a more isolated ground state in the molecule,

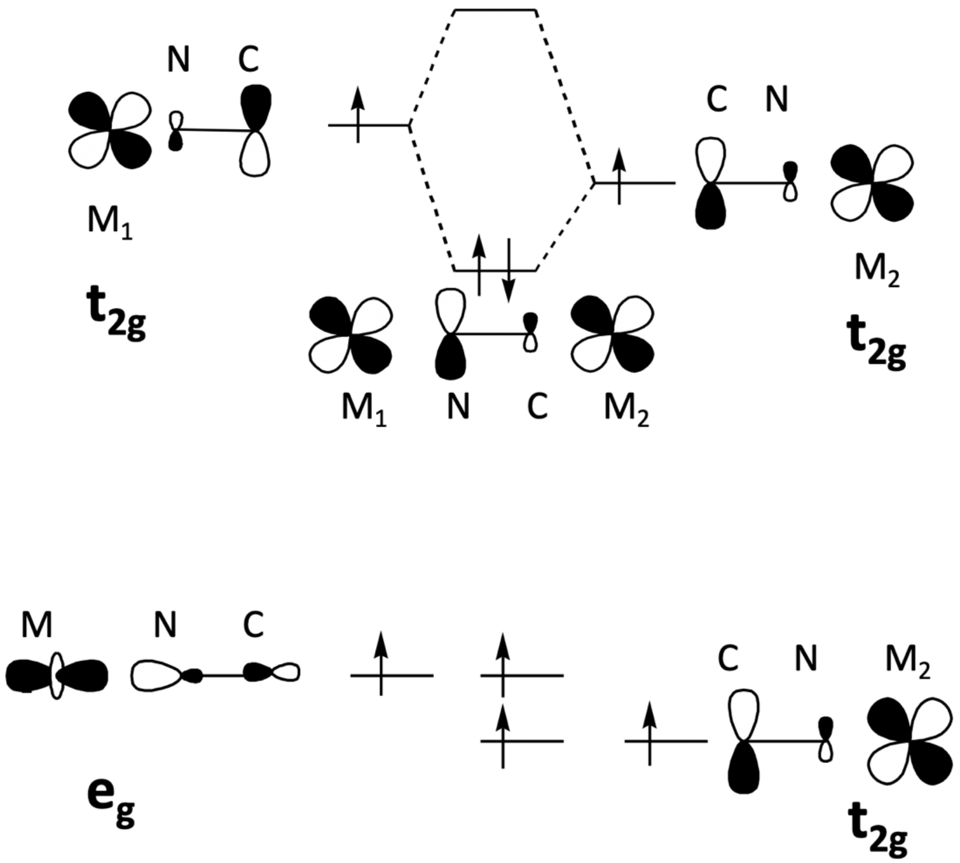

Figure 5. Depiction of the orthogonality principle in cyanide-bridged compounds. Top: symmetry allowed overlap leads to antiferromagnetic exchange due to paired spins. Bottom: orthogonal magnetic orbitals lead to ferromagnetic exchange.

which is important for magnetic properties in polynuclear compounds because it mitigates the population of excited states. Compounds with large coupling and appropriate anisotropy can exhibit SMM behavior — although since the community began focusing on maximizing the anisotropy of single metal atoms, fewer examples of polynuclear SMMs are being reported. Nonetheless, some design principles have emerged. In the series with the formula $[\mathrm{L_{NNN}CoLnCoL_{NNN}}]\mathrm{NO_3}$ (L = N,N′,N″-tris(2-hydroxy-3-methoxy-

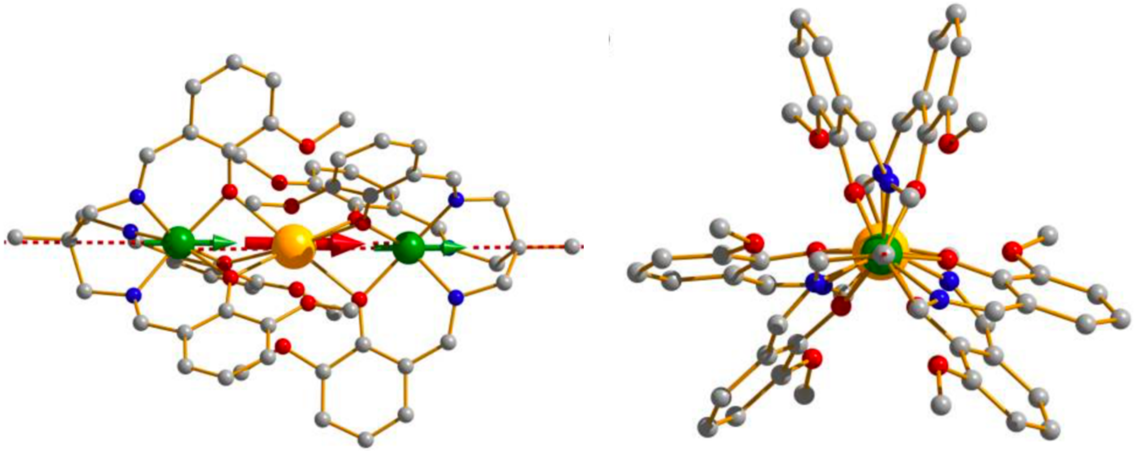

Figure 6. Molecular structure of $[L_{NNN}CoGdCoL_{NNN}]^+$ with both a side and axial view. The red dashed line denotes the local anisotropy axis on Co, and the red and green arrows show the local magnetic moments on Co and Gd in one of the components of the ground state Kramer's doublet. Reprinted with permission from reference 27 Copyright 2013 American Chemical Society.

benzili-dene)-2-(aminomethyl)-2-methyl-1,3-propanediamine; Ln = Gd, Tb, Dy),[26-27] all three compounds in the series are SMMs, but $[L_{NNN}CoGdCoL_{NNN}]NO_3$ is the best SMM (Figure 6). The authors of the work conclude that the isotropic nature of Gd makes it the best match to the anisotropic Co centers. For the Tb and Dy analogues, the conflicting magnetic axes of the lanthanide and Co ions interfere with the anisotropy barrier to reversal of the magnetization. While this realization is valuable, these particular compounds are not particularly impressive examples of SMMs. Increased coupling and a better source of anisotropy would certainly lead to better results.

Anisotropic exchange has emerged as a strategy to improve the properties of polynuclear SMMs by introducing anisotropy to the coupling, rather than relying on localized sources of single ion anisotropy.[21,28-30] Anisotropic exchange is not a novel phenomenon, but very few SMMs that exhibit this specific kind of exchange exist. Despite its rarity, it is possible to intentionally design molecules that exhibit anisotropic exchange.[31] The most important requirement is the existence of an orbitally degenerate electronic ground state for a metal center with significant spin-orbit coupling. In orbitally degenerate compounds, the first order spin-orbit interaction renders S an invalid quantum number. The magnetic properties of these building blocks are often described in terms of pseudo-spin states and fictitious spins to simplify the explanation while acknowledging the limitations of S in that context. Coupling that involves such a metal center splits J into J_x, J_y, and J_z. When J_z is large and $J_x \approx J_y \approx 0$, the anisotropic coupling gives rise to an easy axis in a distinctly different way than D does for mononuclear transition metal SMMs. This easy-axis anisotropy is referred to as “Ising type” anisotropy. Since the barrier originates from J_z, its height is also dependent on the magnitude of the coupling. Theoretically, stronger coupling leads to a larger barrier in anisotropically coupled systems, but there are not yet experimental results to back up this claim. It is important to study molecules that exhibit this type of anisotropy in detail to determine its potential for developing high temperature SMMs. Because the primary requirement for anisotropic exchange is an orbitally degenerate metal center, it is possible to take advantage of the building block approach[32-33] to make these types of SMMs.

The central idea of the building block approach is using discrete compounds as components of a larger structure. Cyanide chemistry represents this approach very well, as cyanometallates are stable and constitute excellent linkers for polynuclear compounds. Many geometries can be accessed for a single cyanometallate based solely on the shape and denticity of the blocking ligands on the second metal complex (Figure 7). Pairing two

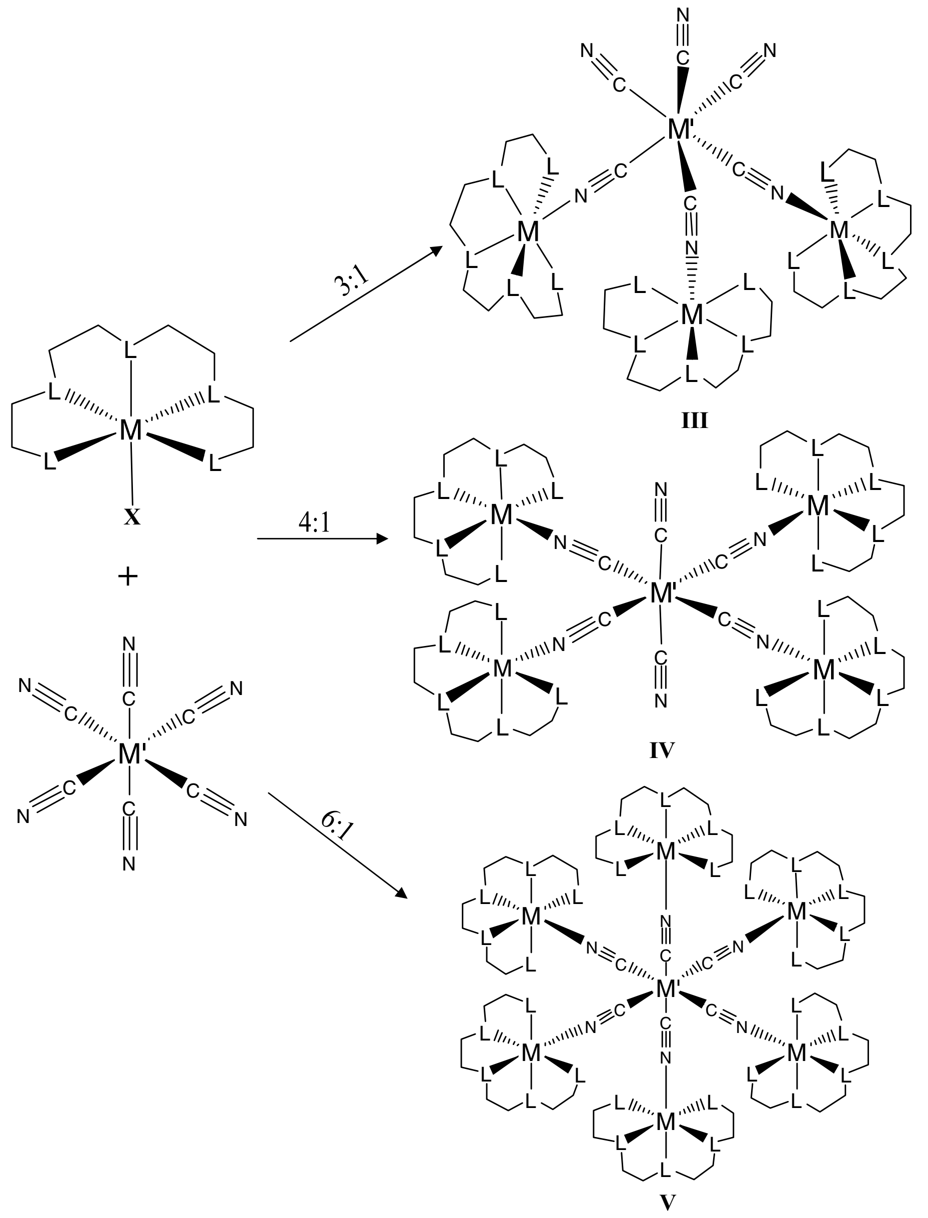

Figure 7. Schematic diagram showing possible structures from reactions of a hexacyanometallate and a metal complex with a pentadentate blocking ligand. Note that the stoichiometry can, hypothetically, control the outcome of the reaction. Reprinted with permission from reference 32, copyright 2009 John Wiley & Sons.

building blocks that will form a specific geometry allows one to design a structure that takes advantage of each component's unique properties. This strategy is especially attractive from the perspective of engendering anisotropic exchange; the ability to choose an orbitally degenerate building block greatly simplifies many of the key challenges when designing systems that exhibit Ising-type anisotropic exchange. Two building blocks that have been previously used in the Dunbar group are standout candidates for this strategy, namely $[Mo^{III}(CN)_7]^{4-}$ and $[(triphos)Re^{II}(CN)_3]^{-}$ (triphos = 1,1,1-Tris(diphenylphosphinomethyl)ethane). What makes these building blocks good candidates for engendering anisotropic exchange is their orbitally degenerate ground state and the presence of cyanide ligands that allow for reliable coordination to other metal centers. These compounds have been used to synthesize impressive molecules with interesting magnetic properties.[16,34-39] However, most of these molecules do not have the ideal geometry for maximizing anisotropic exchange. Thus, one of the major thrusts of research on anisotropic exchange-coupled complexes is the development of reliable methods to synthesize compounds with the correct geometry for Ising-type anisotropic exchange. The requirements for Ising-type anisotropic exchange vary by building block, so the explanations must be treated as separate cases.

The main goal for designing SMMs that incorporate $[Mo^{III}(CN)_7]^{4-}$ is to maintain an undistorted pentagonal bipyramidal arrangement of CN^- ligands and to coordinate metal complexes to the apical CN^- ligands. For Mo^{III}, with its d^3 electron count, pentagonal bipyramidal symmetry leads to an orbitally degenerate pseudo-$S = ½$ ground state (Figure 8). If that symmetry is broken, the orbital degeneracy is quenched and anisotropic exchange will be minimized or quenched. Evidence for this claim can be found in the molecules $[Mn(L_1)(H_2O)]_2[Mo(CN)_7]\cdot 2H_2O$ and $[Mn(L_1)(H_2O)]_2[Mn(L)]_2[Mo(CN)_7]_2$ (Figure 9).[39] These molecules are interchangeable by the addition and removal of water in the crystals, but, while the former trinuclear molecule exhibits SMM behavior, the latter hexanuclear one does not, despite theoretical predictions that these ladder-type compounds should exhibit better magnetic behavior than their trinuclear counterparts.[40] The lack of SMM behavior in the hexanuclear molecule occurs because the distortion of the pentagonal bipyramid of $[Mo^{III}(CN)_7]^{4-}$ quenches the orbital degeneracy of that moiety and eliminates the easy axis of magnetization. The coordination of metal centers to the axial cyanide ligands is equally important, as shown by the three compounds $[Mn(L_{N5Me})(H_2O)]_2[Mo(CN)_7]\cdot 6H_2O$ (L_{N5Me} = 2,2'-(((1*E*,1'*E*)-pyridine-2,6-diylbis(ethan-1-yl-1-ylidene))bis(azaneylylidene))bis(*N*-methylethan-1-amine), $[Mn^{II}(L_{N3O2})(H_2O)]_2$-$[Mo^{III}(CN)_7]\cdot 7H_2O$ (L_{N3O2} = (2*E*,12*E*)-2,13-dimethyl-6,9-dioxa-3,12-diaza-1(2,6)-pyridinacyclotridecaphane-2,12-diene), and $[Mn(L_{DAPSC})(H_2O)]_2[Mo(CN)_7]$-$\cdot 6H_2O\cdot MeCN]$ (L_{DAPSC} = (2*E*,2'*E*)-2,2'-(pyridine-2,6-diylbis(ethan-1-yl-1-ylidene))-bis(hydrazine-1-carboxamide) (Figure 10).[38] The latter two compounds have Mn^{II} coordinated to the apical cyanide ligands of $[Mo^{III}(CN)_7]^{4-}$ and exhibit no SMM behavior, while the former has Mn^{II} coordinated to the apical cyanide ligands and shows the highest temperature hysteresis loops for any cyanide-bridged SMM compound. Theoretical work shows that coupling to apical CN^- ligands of $[Mo^{III}(CN)_7]^{4-}$ can induce Ising-like anisotropic exchange.[28] If the anisotropic exchange has sufficient contribution from J_{xy}, then an easy axis does not develop and SMM behavior is not observed. As shown with the

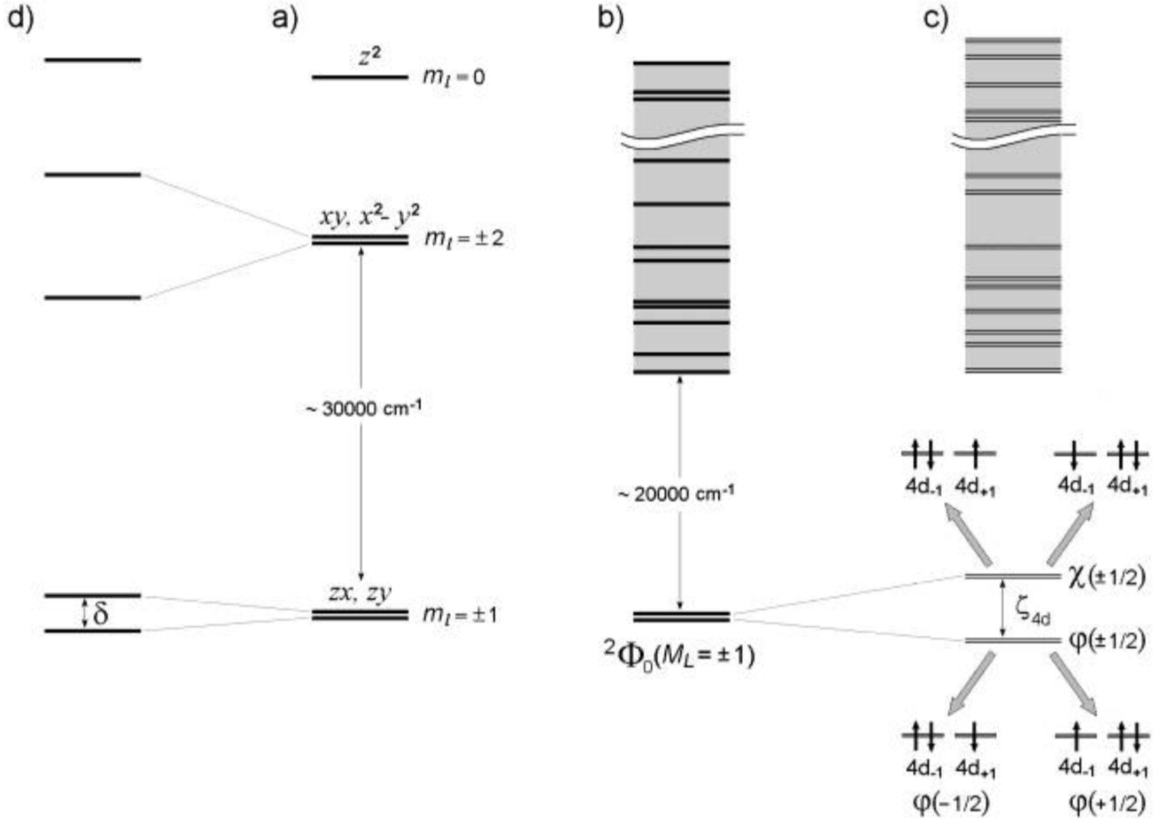

Figure 8. Electronic structure of $[Mo^{III}(CN)_7]^{4-}$: (a) 4d orbital energies in a D_{5h} pyramid, (b) energy spectrum of Mo^{III} in D_{5h} geometry, (c) energy spectrum of Mo^{III} in this geometry with spin-orbit coupling applied. The orbital composition of the ground $\varphi(\pm1/2)$ and excited $\chi(\pm1/2)$ Kramers doublets is shown, (d) the splitting of the 4d orbital energies in distorted complexes of $[Mo^{III}(CN)_7]^{4-}$. Reprinted with permission from reference 28, copyright 2003 American Chemical Society.

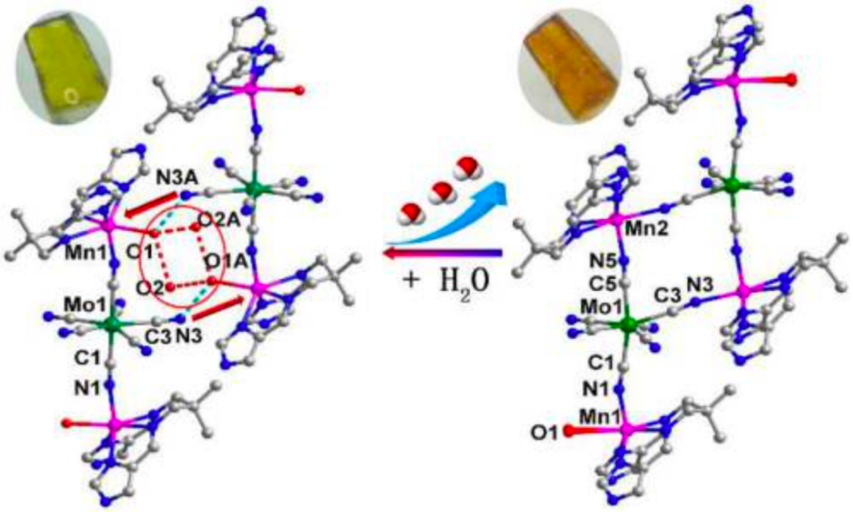

Figure 9. Structures of $[Mn(L_1)(H_2O)]_2[Mo(CN)_7]\cdot 2H_2O$ and $[Mn(L_1)(H_2O)]_2[Mn(L)]_2$-$[Mo(CN)_7]_2$. The red circle on the left shows the water molecules that can be removed by dehydration and the red arrows show the new coordination bonds that form because of that process. Reprinted with permission from reference 39, copyright 2017 Americal Chemical Society.

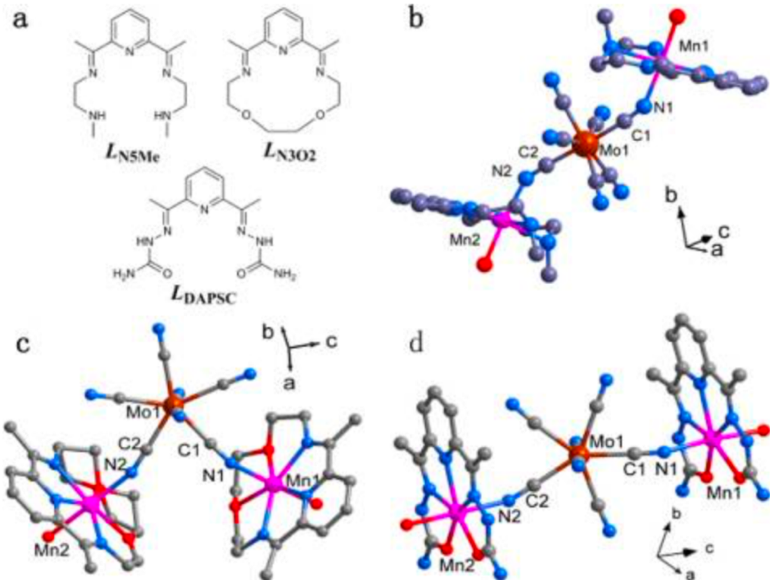

Figure 10. (a) structures of L_{N5Me}, L_{N3O2}, and L_{DAPSC} (b), (c), and (d) structures of each ligand incorporated in to a Mn_2Mo trinuclear compound. Reprinted with permission from reference 38, copyright 2013 American Chemical Society.

molecules in Figure 10, even changes to the ligands on the 3d metal can change the coordination geometry in unpredictable ways. Thus, the biggest barrier to creating better SMMs with $[Mo^{III}(CN)_7]^{4-}$ is the synthetic challenge involved. In the subsequent chapters, this work will demonstrate those challenges through the lens of some reactions of $[Mo^{III}(CN)_7]^{4-}$ and propose some guidelines for improving the SMM behavior of molecules that incorporate this moiety. This work also introduces a new building block, $[Mo^{III}(DAPB)(CN)_2]^-$ ($DAPBH_2$ = diacetylpyridinebis(benzoylhydrazone)) that may improve the properties of future Mo^{III}-based exchange coupled systems by imposing a pentagonal bipyramidal geometry on Mo^{III} that is more rigid than the geometry in $[Mo^{III}(CN)_7]^{4-}$.

The moiety $[(triphos)Re^{II}(CN)_3]^-$ has different requirements than $[Mo^{III}(CN)_7]^{4-}$ for Ising-type anisotropic exchange. Due to the influence of the trigonal crystal field, the ground state of $[(triphos)Re^{II}(CN)_3]$ is orbitally degenerate,[34] allowing for the observation of spin-orbit coupling. The small separation of the ground state and the first excited state also leads to a large amount of temperature independent paramagnetism (TIP) in all reported compounds of $[(triphos)Re^{II}(CN)_3]^-$. The only reported SMMs that contain this moiety are the molecular cube $[\{MnCl\}_4\{Re(triphos)(CN)_3\}_4]$ and the trigonal bipyramidal molecules $(Et_4N)_2[((triphos)Re(CN)_3)_2(Ln(NO_3)_3)_3]\cdot 4MeCN$ (Ln = Dy, Tb).[36-37,41] The trigonal bipyramidal molecules are understood to be SMMs based solely on the magnetic properties of the lanthanide ions; the rhenium center does not significantly contribute to those properties. In the molecular Mn_4Re_4 cube, which is the first known example of a 5d transition metal SMM, anisotropic exchange is responsible for the

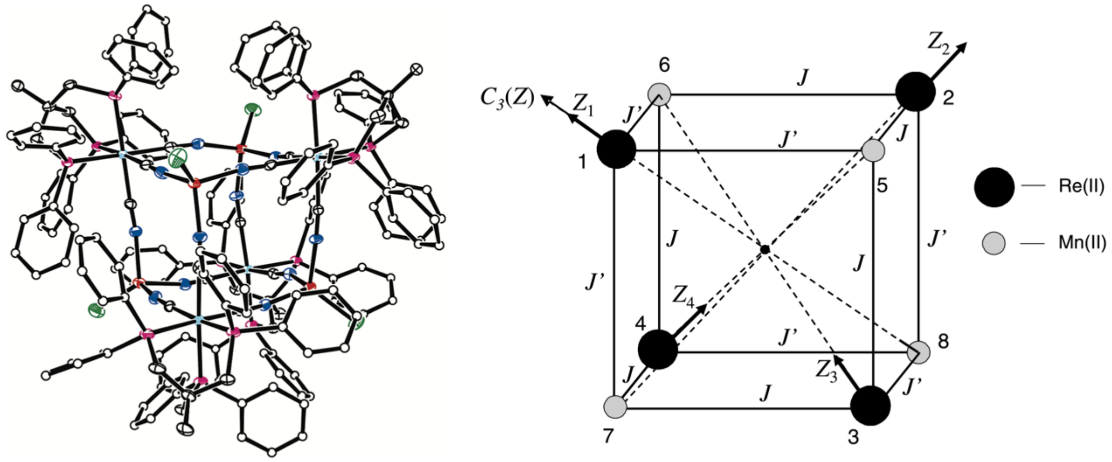

Figure 11. Left: Plot of $[\{MnCl\}_4\{Re(triphos)(CN)_3\}_4]$ with thermal ellipsoids drawn at the 25% probability level. Carbons in the phenyl rings of the triphos ligands are shown with arbitrary radius, and hydrogen atoms omitted for clarity. Reprinted with permission from reference 41, copyright 2007 American Chemical Society. Right: Z-axes of the local and molecular frames and the network of exchange pathways for the Mn_4Re_4 cube. Reprinted with permission from reference 29, copyright 2007 Elsevier.

observed SMM behavior.[29] Magnetic axes develop on the C3 axis of each $[(triphos)Re^{II}(CN)_3]^-$ moiety, so each diagonal of the cube has a magnetic axis (Figure 11). The net magnetic moment in the ground state is significantly reduced due to partial cancellation of those individual magnetic moments. Theoretically, SMM properties of a molecule that incorporates $[(triphos)Re^{II}(CN)_3]^-$ could be improved by ensuring that anisotropic exchange occurs along one unique axis in a molecule. To date, there are no molecules that incorporate this building block with strong coupling and all $[(triphos)Re^{II}(CN)_3]^-$ sharing one magnetic axis. This work will show that it is possible to synthesize such a compound and provides evidence that such a strategy will lead to new advanced in the area of anisotropic exchange coupled systems.

CHAPTER II

CYANIDE BRIDGED CHAINS OF LANTHANIDE AND MOLYBDENUM IONS

Background

While the attention and focus on SMMs has occupied much of the work in the field of molecular magnetism, significant work has also been carried out in the area of single chain magnets (SCMs). SCMs were first proposed by Glaber in 1963[42] and finally realized by Gatteschi and coworkers in 2001.[43] SCMs are excellent candidates to study the effects of magnetic coupling and anisotropy on magnetic behavior and also offer an opportunity to study multi-functionality through optical, conducing, and other properties.[44-45] Like SMMs, SCMs can be made using a variety of strategies. They can be made from one building block or multiple building blocks; as long as the magnetic units in the chain communicate via exchange, there is a chance to observe interesting properties. Notably, the anisotropy in the chain can be different from the anisotropy of the building blocks. In the case of *catena*-$[Fe^{II}(ClO_4)_2\{Fe^{III}(bpca)_2\}]ClO_4$, the selected building blocks exhibit easy-plane anisotropy, but the resulting chain has easy-axis anisotropy, which the authors attribute to the twisting of the easy planes with respect to each other (Figure 12).[46] Because of the difficulty in predicting how building blocks with arrange themselves in a 1D chain, it is challenging to predict the resulting magnetic properties. As such, it is important to investigate 1D chains with different types of building blocks.

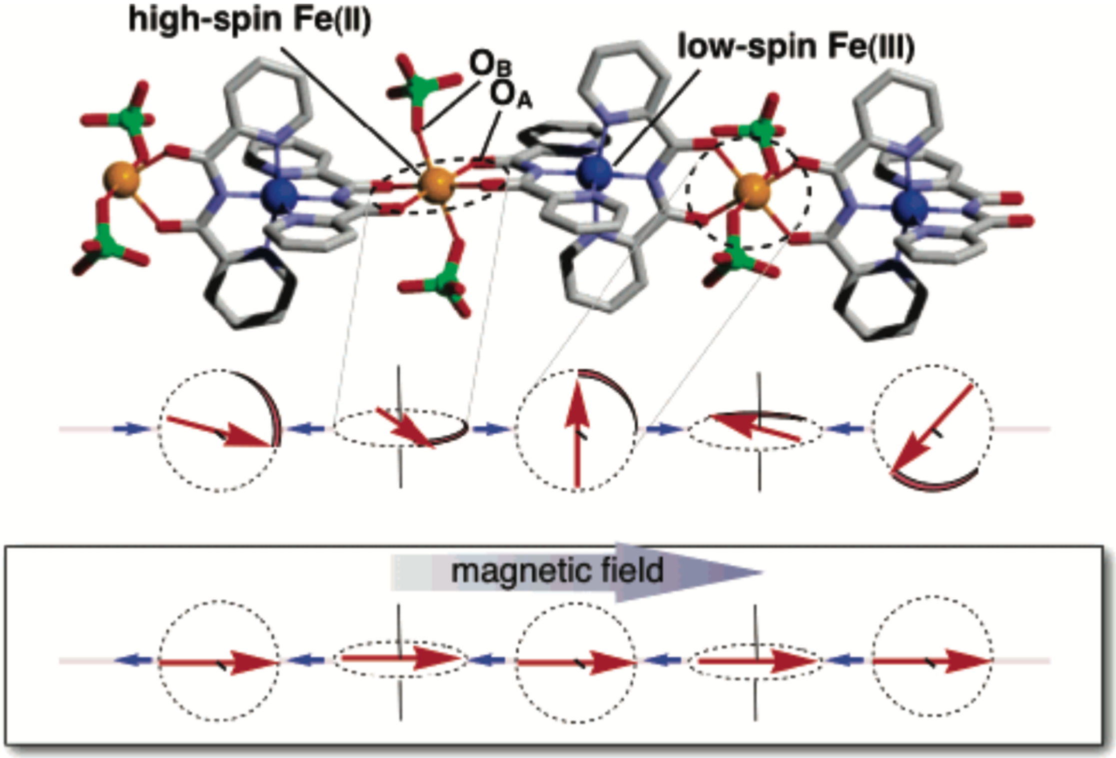

Figure 12. Structure of *catena*-[$Fe^{II}(ClO_4)_2\{Fe^{III}(bpca)_2\}$]$ClO_4$ and spin arrangment of the high-spin Fe^{II} and low-spin Fe^{III} centers contained therein. The O_A and O_B labels show the two different types of oxygen ligands for the high spin Fe^{II} centers. Reproduced with permission from reference 46, copyright 2005 American Chemical Society.

In the case of SCMs, often there is one cyanide containing building block and one other metal center, in order to take advantage of the cyanide ligand's ability to mediate magnetic coupling. While many cyanide-bridged SCMs have been made using octahedral cyanometallates,[47-52] there are none reported that utilize a 7-coordinate derivative. This is an important area because 7-coordinate geometries can lead to unexpected arrangements of atoms, which, as shown above, can heavily influence the behavior of the resulting chain. While there are a number of 3D and 2D coordination polymers that incorporate $[Mo^{III}(CN)_7]^{4-}$,[53-65] there are no reported 1D chains that incorporate this anion. Many of those reports note that the seven coordinate structure of $[Mo^{III}(CN)_7]^{4-}$ reduces the symmetry present in the system as compared to six-coordinate cyanometallates that are frequently used in preparation of these Prussian Blue analogs. The lower symmetry leads to increased anisotropy and more interesting magnetic properties. Those qualities provide a solid rationale for looking into the synthesis of new 1D chains that incorporate $[Mo^{III}(CN)_7]^{4-}$. Our group previously reported a variety of lanthanide-3d chains that provided us with inspiration for this work. We decided to synthesize new compounds analogous to $\{[Sm(tmphen)_2(H_2O)_2Fe(CN)_6]\cdot MeOH\cdot 13H_2O\}_\infty$ and $\{[Sm(tmphen)_2\text{-}(H_2O)_2Cr(CN)_6]\cdot MeOH\cdot 9H_2O\}_\infty$ (tmphen = 3,4,7,8-tetramethyl-1,10-phenanthroline).[66] These compounds (Figure 13) were found to exhibit ferromagnetic exchange between the 3d and 4f metal centers and showed signs of glassy behavior. With similar conditions using $[Mo^{III}(CN)_7]^{4-}$, it may be possible to observe SCM behavior, particularly if anisotropic exchange can be induced between the orbitally degenerate Mo^{III} center and the lanthanide ion. As a result of this work, a new series of chains with the formula $\{K[Ln(tmphen)_2(H_2O)_2Mo^{III}(CN)_7]$ was synthesized to investigate the effect of installing $[Mo^{III}(CN)_7]^{4-}$ in a 1D magnetic chain.

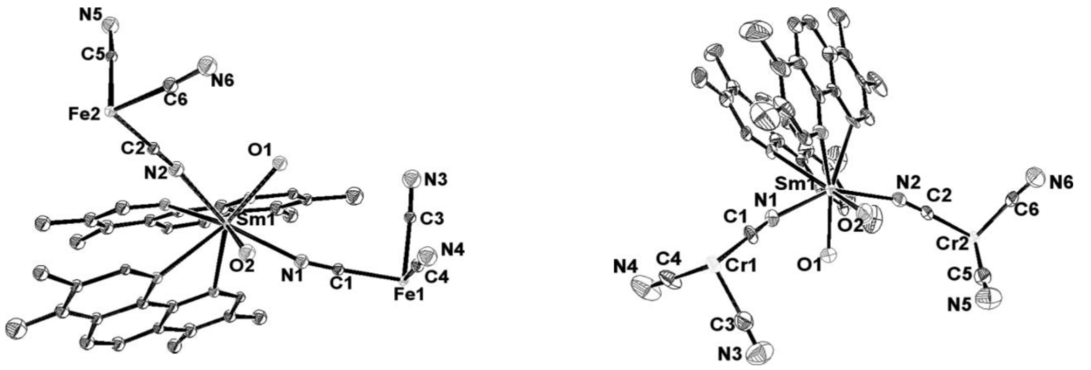

Figure 13. Thermal ellipsoid plots of $\{[Sm(tmphen)_2(H_2O)_2Fe(CN)_6]\cdot MeOH\cdot 13H_2O\}_\infty$ (left) and $\{[Sm(tmphen)_2(H_2O)_2Cr(CN)_6]\cdot MeOH\cdot 9H_2O\}_\infty$ (right) drawn at the 50% probability level. The atoms from solvent molecules have been omitted for the sake of clarity. Reproduced with permission from reference 66, copyright 2007 Royal Society of Chemistry.

Experimental Details

Synthesis

Syntheses were performed under air free conditions in a nitrogen filled glove box. Solvents were deoxygenated by sparging with argon gas on a Schlenk line. $K_4[Mo^{III}(CN)_7] \cdot 2H_2O$ was synthesized using literature methods.[67] All other chemicals were used as received from commercial sources.

$\{K[Gd(tmphen)_2(H_2O)_2Mo^{III}(CN)_7]\}$ (**1**) – 47 mg tmphen (0.2 mmol) and 37mg $GdCl_3$ (0.1 mmol, anhydrous basis) were dissolved in a mixture of 2 mL H_2O, 2 mL DMF, and 1 mL MeCN. This solution was added dropwise to a solution of 50 mg (0.1 mmol) sample of $K_4[Mo^{III}(CN)_7] \cdot 2H_2O$ dissolved in 2 mL H_2O and 2 mL DMF. The yellow solution of $K_4[Mo^{III}(CN)_7] \cdot 2H_2O$ gradually turned orange over the course of the addition. After being left to stand overnight, X-ray quality dark orange crystals were harvested by filtration and washed with DMF and Et_2O, 20 mg, 20% yield. Samples were dried under vacuum prior to submission for elemental analysis and SQUID measurements. Found: C, 46.45; H, 4.47; N, 15.66%. Calculated for $\{K[Gd(tmphen)_2(H_2O)_2Mo^{III}(CN)_7]\} \cdot 2H_2O \cdot MeCN$: C, 46.45; H, 4.09; N, 15.85%.

$\{K[Tb(tmphen)_2(H_2O)_2Mo^{III}(CN)_7]\}$ (**2**) – 47 mg tmphen (0.2 mmol) and 37 mg $TbCl_3$ (0.1 mmol, anhydrous basis) were dissolved in a mixture of 2 mL H_2O, 2 mL DMF, and 1 mL MeCN. This solution was added dropwise to a solution of 50 mg (0.1 mmol) sample of $K_4[Mo^{III}(CN)_7] \cdot 2H_2O$ dissolved in 2 mL H_2O and 2 mL DMF. The yellow solution of $K_4[Mo^{III}(CN)_7] \cdot 2H_2O$ gradually turned orange over the course of the addition. After being left to stand overnight, X-ray quality dark, orange crystals were harvested by filtration and washed with DMF and Et_2O, 23 mg, 23% yield. Samples were dried under vacuum prior to submission for elemental analysis and SQUID measurements. Found: C, 47.05; H, 4.55; N, 15.71%. Calculated for $\{K[Tb(tmphen)_2(H_2O)_2Mo^{III}(CN)_7]\} \cdot H_2O \cdot MeCN$: C, 46.89; H, 4.22; N, 15.62%.

$\{K[Dy(tmphen)_2(H_2O)_2Mo^{III}(CN)_7]\}$ (**3**) – 48 mg tmphen (0.2 mmol) and 38 mg $DyCl_3$ (0.1 mmol, anhydrous basis) were dissolved in a mixture of 4 mL H_2O, 4 mL DMF, and 2 mL MeCN. This solution was added dropwise to a solution of 50 mg (0.1 mmol) sample of $K_4[Mo^{III}(CN)_7] \cdot 2H_2O$ dissolved in 4 mL H_2O and 4 mL DMF. The yellow solution of $K_4[Mo^{III}(CN)_7] \cdot 2H_2O$ gradually turned orange over the course of the addition. After being left to stand overnight, X-ray quality dark, orange crystals were harvested by filtration and washed with DMF and Et_2O, 46 mg, 23% yield. Samples were dried under vacuum prior to submission for elemental analysis and SQUID measurements. Found: C, 46.88; H, 4.89; N, 15.26%. Calculated for $\{K[Dy(tmphen)_2(H_2O)_2Mo^{III}(CN)_7]\} \cdot H_2O \cdot DMF$: C, 46.73; H, 4.20; N, 15.57%.

$\{K[Ho(tmphen)_2(H_2O)_2Mo^{III}(CN)_7]\}$ (**4**) – 48 mg tmphen (0.2 mmol) and 38 mg $HoCl_3$ (0.2 mmol, anhydrous basis) were dissolved in a mixture of 4 mL H_2O, 4 mL DMF, and 2 mL MeCN. This solution was added dropwise to a solution of 50 mg (0.1 mmol) sample of $K_4[Mo^{III}(CN)_7] \cdot 2H_2O$ dissolved in 4 mL H_2O and 4 mL DMF. The yellow solution of $K_4[Mo^{III}(CN)_7] \cdot 2H_2O$ gradually turned orange over the course of the addition. After being left to stand overnight, X-ray quality dark, orange crystals were harvested by filtration and washed with DMF and Et_2O, 40 mg, 20% yield. Samples were dried under vacuum prior to submission for elemental analysis and SQUID measurements. Found: C, 49.45; H, 4.67; N, 14.00%. Calculated for $\{K[Ho(tmphen)_2(H_2O)_2Mo^{III}(CN)_7]\} \cdot 2Et_2O$: C, 49.56; H, 4.96; N, 13.53%.

$\{K[Er(tmphen)_2(H_2O)_2Mo^{III}(CN)_7]\}$ (**5**) – 48 mg tmphen (0.2 mmol) and 38 mg $ErCl_3$ (0.1 mmol, anhydrous basis) were dissolved in a mixture of 4 mL H_2O, 4 mL DMF, and 2 mL MeCN. This solution was added dropwise to a solution of 50 mg (0.1 mmol) sample of $K_4[Mo^{III}(CN)_7] \cdot 2H_2O$ dissolved in 4 mL H_2O and 4 mL DMF. The yellow solution of $K_4[Mo^{III}(CN)_7] \cdot 2H_2O$ gradually turned orange over the course of the addition. After being left to stand overnight, X-ray quality dark, orange crystals were harvested by filtration and washed with DMF and Et_2O, 45 mg, 22% yield. Samples were dried under vacuum prior to submission for elemental analysis and SQUID measurements. Found: C, 50.43; H, 4.32; N, 12.94%. Calculated for $\{K[Er(tmphen)_2(H_2O)_2Mo^{III}(CN)_7]\} \cdot 2Et_2O$: C, 49.46; H, 4.95; N, 13.5%.

Infrared Spectroscopy

Infrared spectra were collected on a Nicolet 740 Fourier transform IR spectrometer. Samples were prepared and measured as a Nujol® mulls between KBr plates.

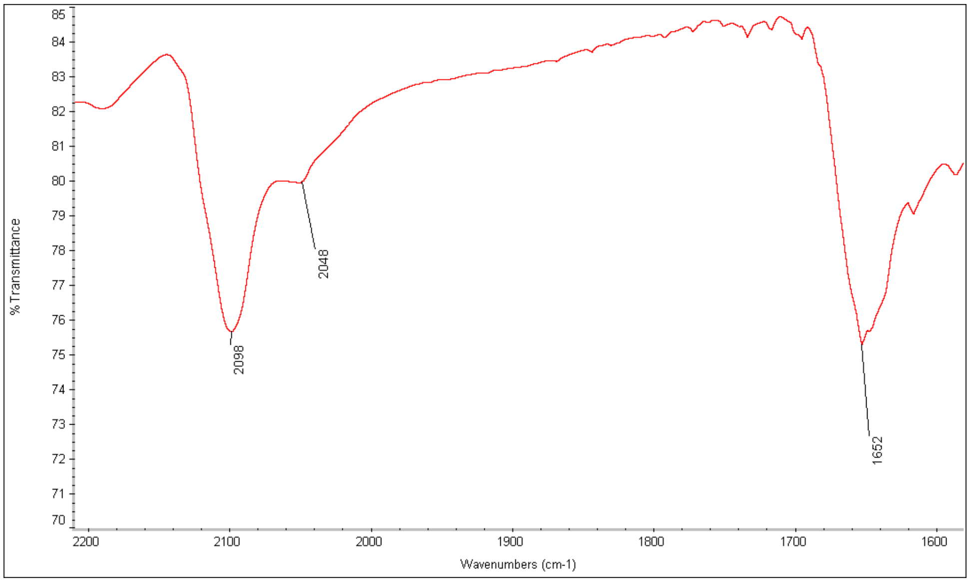

Figure 14. IR spectrum for **1**. The peaks at 2098 and 2048 are typical for bridging and terminal cyanide ligands, respectively. The features from 1700-1500 are attributed to the aromatic tmphen ligands.

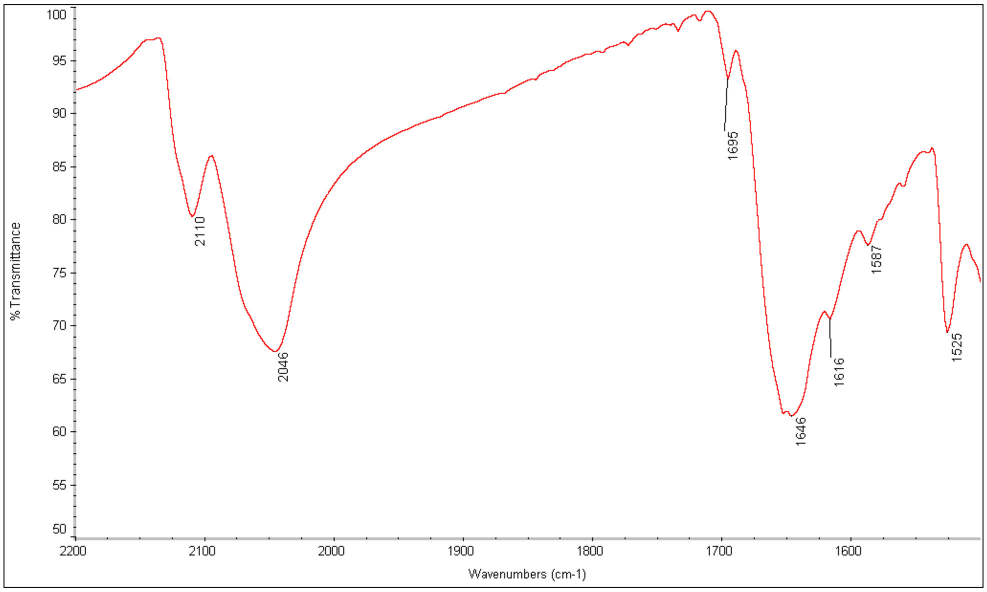

Figure 15. IR spectrum for **2**. The peaks at 2110 and 2046 are typical for bridging and terminal cyanide ligands, respectively. The features from 1700-1500 are attributed to the aromatic tmphen ligands.

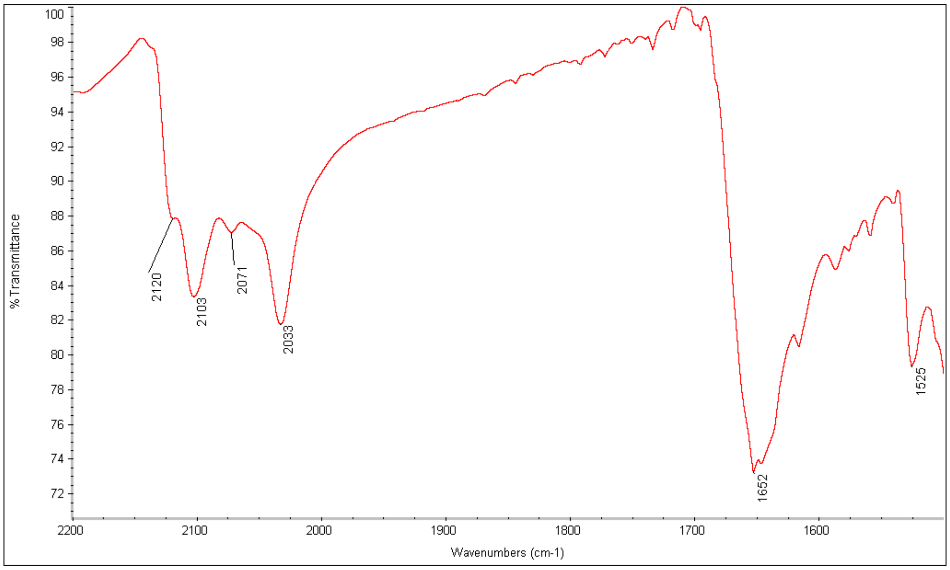

Figure 16. IR spectrum for **3**. The peaks from 2120-2033 are typical for bridging and terminal cyanide ligands, respectively. The features from 1700-1500 are attributed to the aromatic tmphen ligands.

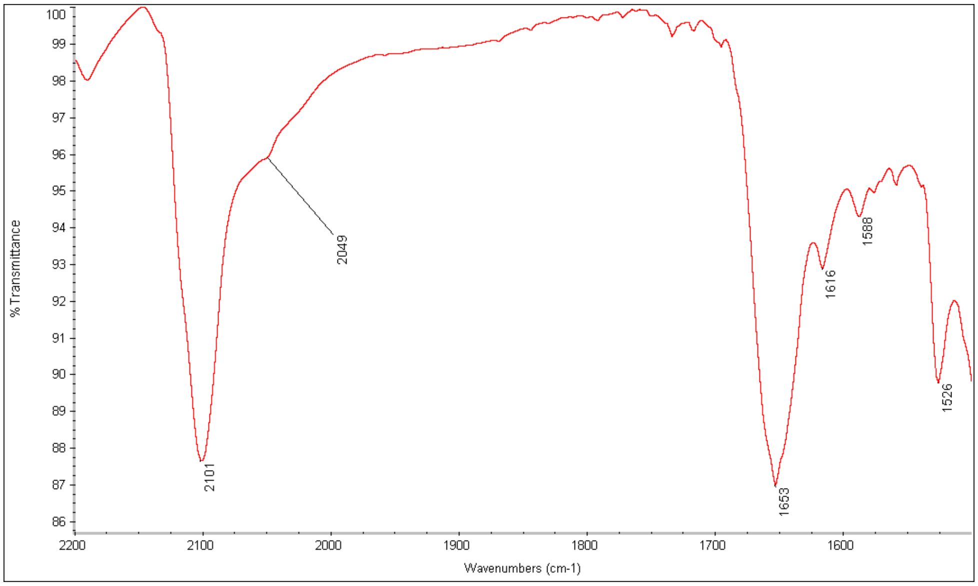

Figure 17. IR spectrum for **4**. The peaks at 2098 and 2048 are typical for bridging and terminal cyanide ligands, respectively. The features from 1700-1500 are attributed to the aromatic tmphen ligands.

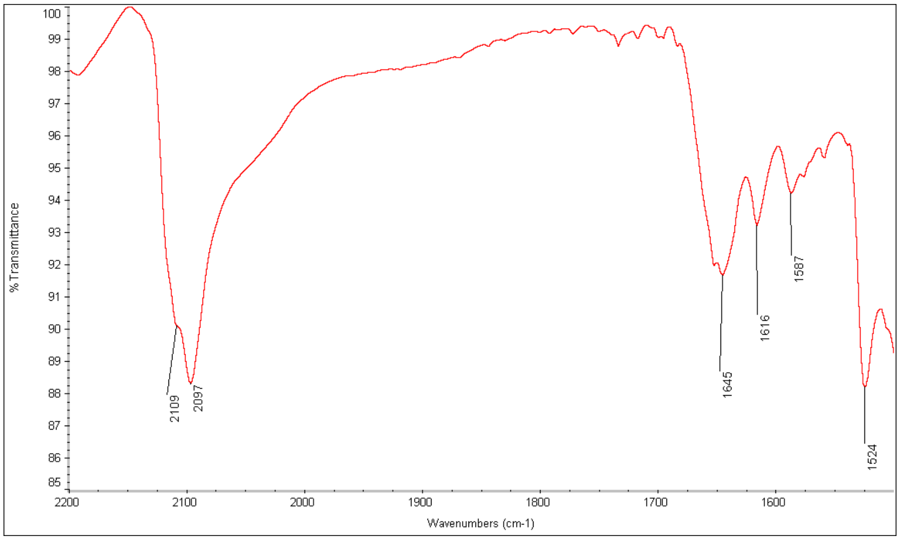

Figure 18. IR spectrum for **5**. The peaks at 2109 and 2097 are typical for bridging and terminal cyanide ligands, respectively. The features from 1700-1500 are attributed to the aromatic tmphen ligands.

Crystallography

Single crystals of the Ln-Mo chains were selected under Paratone® oil with a MiTGen microloop. Reflection data were collected on a Bruker D8-VENTURE diffractometer equipped with a IμS Cu microsource ($\lambda = 1.54178$ Å) and under a stream of N_2 gas a 100 K. The frames were integrated and a semi-empirical absorption correction was applied using SADABS[68] within the software package included in the APEX3 software suite.[69] The structure was solved using SHELXT[70] and refined using SHELXL;[71] OLEX2 was used as an interface for the solution and refinement.[72] Small Q-peaks in the structure that were consistent with the behavior of disordered solvent were removed using the SQUEEZE routine of the PLATON software package.[73] Hydrogen atoms were placed in calculated positions.

The structures all contain a highly disordered $[Mo(CN)_7]^{4-}$ moiety. Several methods of modeling were attempted; the $\{Mo(CN)_7\}$ fragment fit best with the data. When $\{Mo(CN)_6\}$ was used instead, both the geometry and areas of electron density around the Mo centers suggested that some cyanide ligands were unaccounted for. The geometry of the Mo center is significantly distorted from pentagonal bipyramidal. The geometry is between that of a pentagonal bipyramid and a capped trigonal prism. The lanthanide ions have the geometry of a flattened square antiprism. The vertices of the two square faces in the antiprism are occupied by two nitrogen atoms from the tmphen ligand, one nitrogen atom from the cyanide ligand, and one oxygen atom from the water ligand. As mentioned above, the two square faces are closer together than in a perfect square antiprism, giving the geometry a "squashed" appearance. While the structures all crystallized with identical unit cells, the refinements have some variation based on what fit best with each data set.

GdMo – The {Mo(CN)$_7$} fragment is disordered in a 81:19 ratio. The Mo-C bond lengths for the major component ranged from 2.15(3) Å to 2.406(19) Å. The Mo-C bond lengths in the minor component ranged from 2.13(2) Å to 2.43(2) Å. The Gd-N bonds from tmphen are 2.548(4) Å and 2.543(4) Å, while the bond lengths of the Gd-N from cyanide and Gd-O are 2.71(5) Å and 2.369(4) Å, respectively. Selected bond angles around the lanthanide centers are described in Table 6. The SADI restraint was used to restrain the cyanide bond lengths to each other. This was necessary to maintain the stability of the {Mo(CN)$_7$} fragment – the lack of this restraint led to chemically unreasonable refinement results. The SIMU restraint was similarly used to model the thermal parameters on the {Mo(CN)$_7$} fragments; even with this restraint, the ISOR was needed to obtain a reasonable thermal parameter for nitrogen atom N8B. Additional details can be found in Table 1.

Table 1. Crystal data and structure refinement for **1**.

Identification code	GdMo
Empirical formula	$C_{39}H_{36}GdMoN_{11}O_2$
Formula weight	943.98
Temperature/K	100.0
Crystal system	monoclinic
Space group	C2/c
a/Å	21.1413(9)
b/Å	20.1562(7)
c/Å	13.5598(5)
α/°	90
β/°	110.624(2)
γ/°	90
Volume/Å^3	5407.9(4)
Z	4
ρ_{calc}g/cm^3	1.159
μ/mm^{-1}	10.033
F(000)	1876.0
Crystal size/mm^3	0.3 × 0.2 × 0.1
Radiation	CuKα (λ = 1.54178)
2Θ range for data collection/°	8.774 to 145.524
Index ranges	$-26 \le h \le 26$, $-24 \le k \le 24$, $-16 \le l \le 12$
Reflections collected	33504
Independent reflections	5345 [R_{int} = 0.0540, R_{sigma} = 0.0388]
Data/restraints/parameters	5345/493/453
Goodness-of-fit[a] on F^2	1.069
Final R indexes [I>=2σ (I)]	R_1[b] = 0.0565, wR_2[c] = 0.1569
Final R indexes [all data]	R_1[b] = 0.0593, wR_2[c] = 0.1602
Largest diff. peak/hole / e Å^{-3}	1.35/-0.79

[a] Goodness-of-fit = $\{\Sigma [w(Fo^2 - Fc^2)^2]/(n-p)\}^{1/2}$, where n is the number of reflections and p is the total number of parameters refined.

[b] $R = \Sigma || Fo | - | Fc || / \Sigma | Fo |$

[c] $wR = \{\Sigma [w(Fo^2 - Fc^2)^2] / \Sigma w(Fo^2)^2]\}^{1/2}$

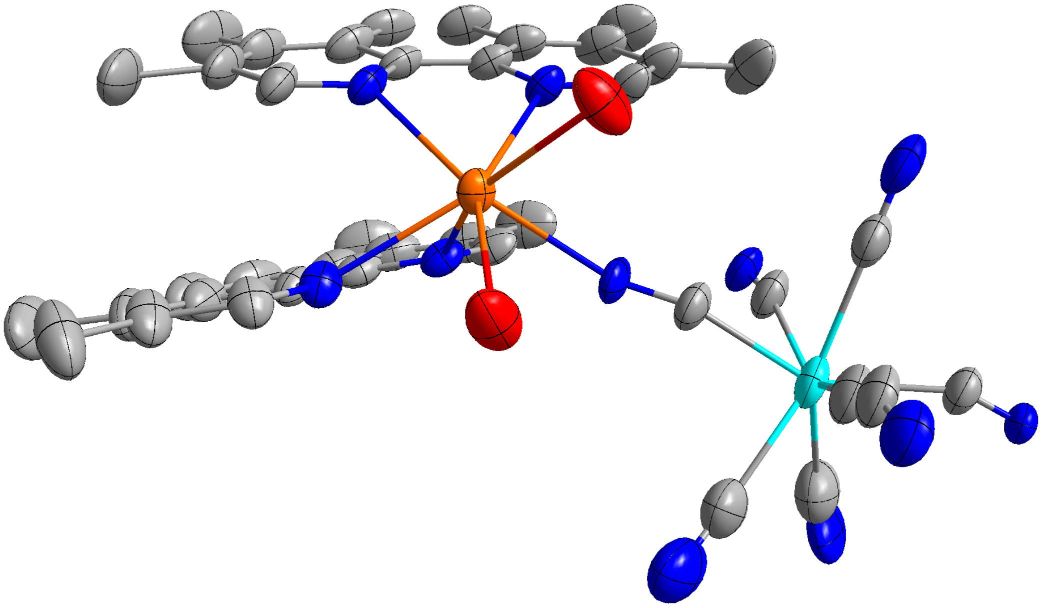

Figure 19. Repeating unit of **1**. Only the major component of the {Mo(CN)$_7$} fragment is shown. Hydrogen atoms are omitted for clarity. Ellipsoids drawn at the 50% probability level.

2 – The {Mo(CN)$_7$} fragment is disordered in a 82:18 ratio. The Mo-C bond lengths for the major component range from 2.237(10) Å to 2.256(10) Å. The Mo-C bond lengths in the minor component range from 2.242(10) Å to 2.267(18) Å. The Tb-N bonds from tmphen are 2.532(5) Å and 2.548(6) Å, while the bond lengths of the Tb-N from cyanide and Tb-O are 2.76(5) Å and 2.366(5) Å, respectively. Selected bond angles around the lanthanide centers are described in Table 6. SADI restraints were used on the cyanide bond lengths as well as the Mo-C bond lengths in the {Mo(CN)$_7$} fragment. SIMU restraints were used on the thermal parameters of the atoms in the {Mo(CN)$_7$} fragment. The ISOR restraint was again used on N8B, which was necessary to prevent a non-positive definite anisotropic thermal parameter. The constraints EXYZ and EADP were used on

N9A and N9B, as they were very close together and having a negative impact on the refinement when allowed to refine without those constraints. A SAME restraint was also used to restrain the geometries of the two {$Mo(CN)_7$} fragments with respect to each other. Additional details can be found in Table 2.

3 – The {$Mo(CN)_7$} fragment is disordered in a 72.4:25.6 ratio. The Mo-C bond lengths for the major component range from 2.200(8) Å to 2.221(9) Å. The Mo-C bond lengths in the minor component range from 2.205(9) Å to 2.223(9) Å. The Dy-N bonds from tmphen are 2.524(4) Å and 2.527(4) Å, while the bond lengths of the Dy-N from cyanide and Dy-O are 2.62(3) Å and 2.317(4) Å, respectively. A similar list of restraints was used on **3** as with **2**. Selected bond angles around the lanthanide centers are described in Table 6. There are SADI and restraints for the cyanide and Mo-C bond lengths, a SIMU and SAME restraint for the {$Mo(CN)_7$} fragment, and one ISOR restraint for N8B. In addition, EXYZ and EADP were used for N9A and N9B. Additional details can be found in Table 3.

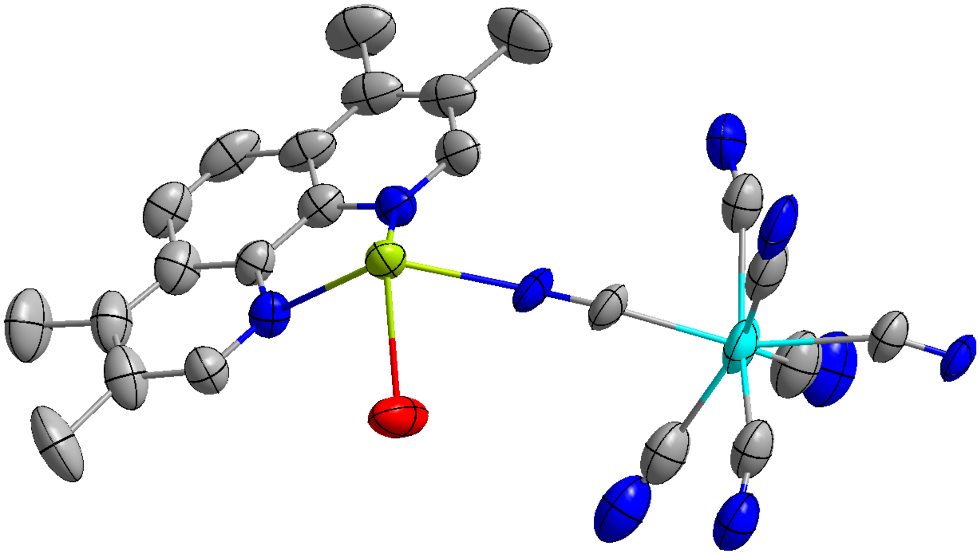

Figure 20. Asymmetric unit of **2**. Only the major component of the {Mo(CN)$_7$} fragment is shown. Hydrogen atoms are omitted for clarity. Ellipsoids drawn at the 50% probability level.

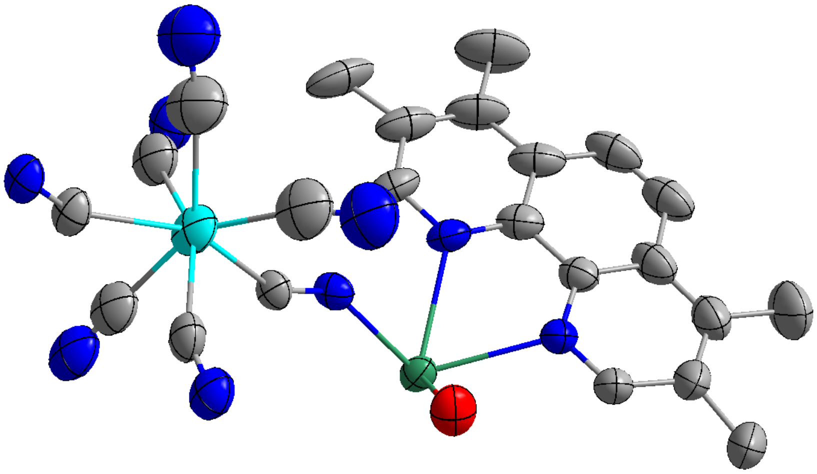

Figure 21. Asymmetric unit of **3**. Only the major component of the {Mo(CN)$_7$} fragment is shown. Hydrogen atoms are omitted for clarity. Ellipsoids drawn at the 50% probability level.

Table 2. Crystal data and structure refinement for **2**.

Identification code	TbMo
Empirical formula	$C_{39}H_{36}MoN_{11}O_2Tb$
Formula weight	945.65
Temperature/K	100.0
Crystal system	monoclinic
Space group	C2/c
a/Å	21.2353(15)
b/Å	20.0775(11)
c/Å	13.7060(9)
α/°	90
β/°	110.594(3)
γ/°	90
Volume/Å^3	5470.1(6)
Z	4
ρ_{calc}g/cm^3	1.148
μ/mm^{-1}	8.434
F(000)	1880.0
Crystal size/mm^3	0.1 × 0.3 × 0.4
Radiation	CuKα (λ = 1.54178)
2Θ range for data collection/°	6.256 to 147.008
Index ranges	$-26 \leq h \leq 26$, $-24 \leq k \leq 24$, $-16 \leq l \leq 16$
Reflections collected	31943
Independent reflections	5441 [R_{int} = 0.0790, R_{sigma} = 0.0570]
Data/restraints/parameters	5441/589/444
Goodness-of-fit[a] on F^2	1.051
Final R indexes [I>=2σ (I)]	R_1[b] = 0.0757, wR_2[c] = 0.2149
Final R indexes [all data]	R_1[b] = 0.0861, wR_2[c] = 0.2265
Largest diff. peak/hole / e Å^{-3}	1.70/-0.59

[a] Goodness-of-fit = $\{\Sigma [w(Fo^2 - Fc^2)^2]/(n-p)\}^{1/2}$, where n is the number of reflections and p is the total number of parameters refined.

[b] $R = \Sigma \| Fo | - | Fc \| / \Sigma | Fo |$

[c] $wR = \{\Sigma [w(Fo^2 - Fc^2)^2] / \Sigma w(Fo^2)^2]\}^{1/2}$

Table 3. Crystal data and structure refinement for **3**.

Identification code	DyMo
Empirical formula	$C_{39}H_{36}DyMoN_{11}O_2$
Formula weight	949.23
Temperature/K	100.0
Crystal system	monoclinic
Space group	C2/c
a/Å	21.1080(11)
b/Å	20.4345(10)
c/Å	13.6909(7)
α/°	90
β/°	111.924(3)
γ/°	90
Volume/Å^3	5478.2(5)
Z	4
ρ_{calc}g/cm^3	1.151
μ/mm^{-1}	9.371
F(000)	1884.0
Crystal size/mm^3	0.2 × 0.4 × 0.5
Radiation	CuKα (λ = 1.54178)
2Θ range for data collection/°	8.654 to 141.952
Index ranges	$-25 \le h \le 25$, $-24 \le k \le 24$, $-14 \le l \le 16$
Reflections collected	35645
Independent reflections	5211 [R_{int} = 0.0600, R_{sigma} = 0.0383]
Data/restraints/parameters	5211/601/444
Goodness-of-fit[a] on F^2	1.079
Final R indexes [I>=2σ (I)]	R_1[b] = 0.0563, wR_2[c] = 0.1687
Final R indexes [all data]	R_1[b] = 0.0618, wR_2[c] = 0.1747
Largest diff. peak/hole / e Å^{-3}	0.99/-0.73

[a]Goodness-of-fit = $\{\Sigma [w(Fo^2 - Fc^2)^2]/(n-p)\}^{1/2}$, where n is the number of reflections and p is the total number of parameters refined.

[b]$R = \Sigma \| Fo | - | Fc \| / \Sigma | Fo |$

[c]$wR = \{\Sigma [w(Fo^2 - Fc^2)^2] / \Sigma w(Fo^2)^2]\}^{1/2}$

4 – The {Mo(CN)$_7$} fragment is disordered in a 84.8:15.2 ratio. The Mo-C bond lengths for the major component range from 2.14(3) Å to 2.26(3) Å. The Mo-C bond lengths in the minor component range from 2.11(4) Å to 2.31(2) Å. The Ho-N bonds from tmphen are 2.507(3) Å and 2.513(3) Å, while the bond lengths of the Ho-N from cyanide and Ho-O are 2.62(6) Å and 2.324(3) Å, respectively. Selected bond angles around the lanthanide centers are described in Table 6. A similar list of restraints was used on **4** as with **1-3**. There are SADI and restraints for the cyanide, a SIMU and SAME restraint for the {Mo(CN)$_7$} fragment, and one ISOR restraint for N8B. In addition, EXYZ and EADP were used for N9A and N9B. Additional details can be found in Table 4.

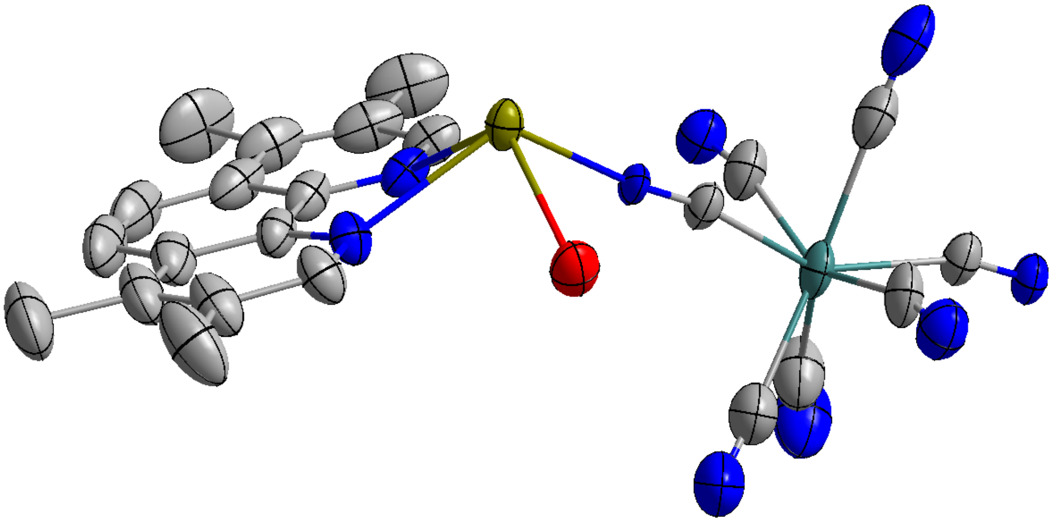

Figure 22. Asymmetric unit of **4**. Only the major component of the {Mo(CN)$_7$} fragment is shown. Hydrogen atoms are omitted for clarity. Ellipsoids drawn at the 50% probability level.

Table 4. Crystal data and structure refinement for **4**.

Identification code	HoMo
Empirical formula	$C_{39}H_{36}HoMoN_{11}O_2$
Formula weight	951.66
Temperature/K	100.0
Crystal system	monoclinic
Space group	C2/c
a/Å	20.9472(11)
b/Å	20.2772(10)
c/Å	13.5431(7)
α/°	90
β/°	111.534(2)
γ/°	90
Volume/Å^3	5350.9(5)
Z	4
ρ_{calc}g/cm^3	1.181
μ/mm^{-1}	4.884
F(000)	1888.0
Crystal size/mm^3	0.2 × 0.2 × 0.5
Radiation	CuKα (λ = 1.54178)
2Θ range for data collection/°	8.722 to 141.366
Index ranges	$-24 \leq h \leq 25$, $-23 \leq k \leq 24$, $-16 \leq l \leq 16$
Reflections collected	30000
Independent reflections	5065 [$R_{int} = 0.0452$, $R_{sigma} = 0.0322$]
Data/restraints/parameters	5065/517/444
Goodness-of-fit[a] on F^2	1.086
Final R indexes [I>=2σ (I)]	R_1[b] = 0.0433, wR_2[c] = 0.1389
Final R indexes [all data]	R_1[b] = 0.0473, wR_2[c] = 0.1416
Largest diff. peak/hole / e Å^{-3}	0.84/-0.53

[a] Goodness-of-fit = $\{\Sigma [w(Fo^2 - Fc^2)^2]/(n-p)\}^{1/2}$, where n is the number of reflections and p is the total number of parameters refined.

[b] $R = \Sigma \| Fo | - | Fc \| / \Sigma | Fo |$

[c] $wR = \{\Sigma [w(Fo^2 - Fc^2)^2] / \Sigma w(Fo^2)^2]\}^{1/2}$

5 – The {Mo(CN)$_7$} fragment is disordered in a 82.2:17.8 ratio. The Mo-C bond lengths range from 2.220(8) Å to 2.246(9) Å and 2.229(9) Å to 2.243(9) Å for the major and minor component, respectively. The Er-N bonds from tmphen are 2.503(4) Å and 2.507(4) Å, while the bond lengths of the Er-N from cyanide and Dy-O are 2.428(10) Å and 2.303(4) Å, respectively. Selected bond angles around the lanthanide centers are described in Table 6. There are SADI restraints for the cyanide and Mo-C bond lengths, a SIMU and SAME restraint for the {Mo(CN)$_7$} fragment, and one ISOR restraint for N8B. In addition, EXYZ and EADP were used for each pair of disordered, terminal nitrogen atoms (N9A, N9B, N3A, and N3B). See Table 5 for details.

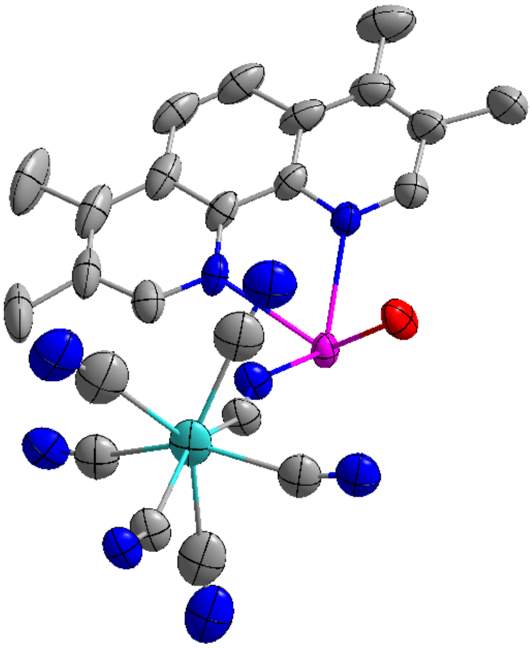

Figure 23. Asymmetric unit of **5**. Only the major component of {Mo(CN)$_7$} is shown. Hydrogen atoms are omitted for clarity. Ellipsoids drawn at the 50% probability level.

Table 5. Crystal data and structure refinement for **5**.

Identification code	ErMo
Empirical formula	$C_{39}H_{36}ErMoN_{11}O_2$
Formula weight	953.99
Temperature/K	100.0
Crystal system	monoclinic
Space group	C2/c
a/Å	21.0503(7)
b/Å	20.3290(6)
c/Å	13.6886(5)
α/°	90
β/°	112.0963(18)
γ/°	90
Volume/Å^3	5427.5(3)
Z	46
ρ_{calc}g/cm^3	8.288
μ/mm^{-1}	99.626
F(000)	11272.0
Crystal size/mm^3	0.2 × 0.2 × 0.6
Radiation	CuKα (λ = 1.54178)
2Θ range for data collection/°	8.7 to 127.718
Index ranges	$-24 \leq h \leq 24$, $-23 \leq k \leq 23$, $-15 \leq l \leq 15$
Reflections collected	30713
Independent reflections	4466 [R_{int} = 0.0598, R_{sigma} = 0.0370]
Data/restraints/parameters	4466/614/435
Goodness-of-fit[a] on F^2	1.075
Final R indexes [I>=2σ (I)]	R_1[b] = 0.0511, wR_2[c] = 0.1618
Final R indexes [all data]	R_1[b] = 0.0570, wR_2[c] = 0.1664
Largest diff. peak/hole / e Å^{-3}	1.30/-0.52

[a] Goodness-of-fit = $\{\Sigma [w(Fo^2 - Fc^2)^2]/(n-p)\}^{1/2}$, where n is the number of reflections and p is the total number of parameters refined.

[b] $R = \Sigma || Fo | - | Fc || / \Sigma | Fo |$

[c] $wR = \{\Sigma [w(Fo^2 - Fc^2)^2] / \Sigma w(Fo^2)^2]\}^{1/2}$

Table 6. Selected bond lengths and angles for the LnMo chains. All distances are given in Å and angles are given in degrees (°).

	1	**2**	**3**	**4**	**5**
Ln - O1	2.369(4)	2.366(5)	2.317(4)	2.324(3)	2.303(4)
Ln - N1	2.548(4)	2.548(6)	2.524(4)	2.513(3)	2.503(4)
Ln - N2	2.543(4)	2.532(5)	2.527(4)	2.507(3)	2.507(4)
Ln - N3A	2.46(3)	2.398(17)	2.448(13)	2.39(3)	2.428(10)
Ln - N3B	2.71(5)	2.76(5)	2.62(3)	2.62(6)	2.428(10)
O1 - Ln - O1'	82.8(2)	82.0(3)	83.2(2)	82.80(14)	82.7(2)
O1 - Ln - N1	112.72(16)	113.2(2)	112.85(15)	112.80(10)	112.84(15)
O1' - Ln - N1	145.40(15)	145.2(2)	144.84(14)	144.94(10)	144.97(15)
O1 - Ln - N2	77.11(14)	77.09(18)	76.48(14)	76.45(10)	76.50(14)
O1' - Ln - N2	150.43(14)	150.6(2)	150.67(14)	150.17(9)	150.03(14)
O1 - Ln - N3A	76.6(10)	76.3(9)	77.2(7)	75.2(8)	76.6(5)
O1' - Ln - N3A	81.4(10)	81.4(7)	82.3(4)	75.4(7)	81.2(4)
N1 - Ln - N2	63.75(13)	63.55(18)	64.02(13)	64.35(10)	64.48(14)
N1 - Ln - N3A	73.2(9)	72.9(6)	71.9(4)	78.7(8)	72.9(3)
N2 - Ln - N3A	114.1(11)	112.9(8)	112.9(5)	118.6(7)	114.0(5)
N3A -Ln - N3A'	150.486	150.252	152.644	140.37	150.384

Magnetic measurements

Measurements were performed on a Quantum Design MPMS-XL SQUID magnetometer equipped with a 7 T magnet. A polypropylene bag was used to secure the sample, and the diamagnetic contribution was subtracted from the raw data. Diamagnetic contributions from the sample were accounted for by using Pascal's constants.[74]

1 – Variable temperature static DC magnetic susceptibility measurements were performed on crushed crystals of **1** from 300 to 2 K under an applied field of 1000 Oe (Figure 24). The room temperature value of 8.5 cm^3 K mol^{-1} is consistent with one Gd center and one S = ½ Mo^{III} center. The decrease, which accelerates as the sample is cooled to about 10 K, can be attributed to weak antiferromagnetic coupling between Gd and Mo, interchain interactions, or spin-orbit coupling. The reduced magnetization plot for **1** (Figure 25) shows that there is a small amount of anisotropy in the system, with near overlap of some isofield lines. This anisotropy likely originates from the spin-orbit coupling of Mo^{III}. Since there is evidence of magnetic coupling between the metal centers and the reduced magnetization indicates spin-orbit coupling, it is possible that there is minor anisotropic exchange in the system. Alternating current (AC) measurements were performed to evaluate the magnetic dynamics of **1** (Figure 26). There was no notable slow relaxation of the magnetization observed, including in measurements that included a static DC field up to 2000 Oe. The lack of signal in these measurements indicates there is no SCM behavior in this chain.

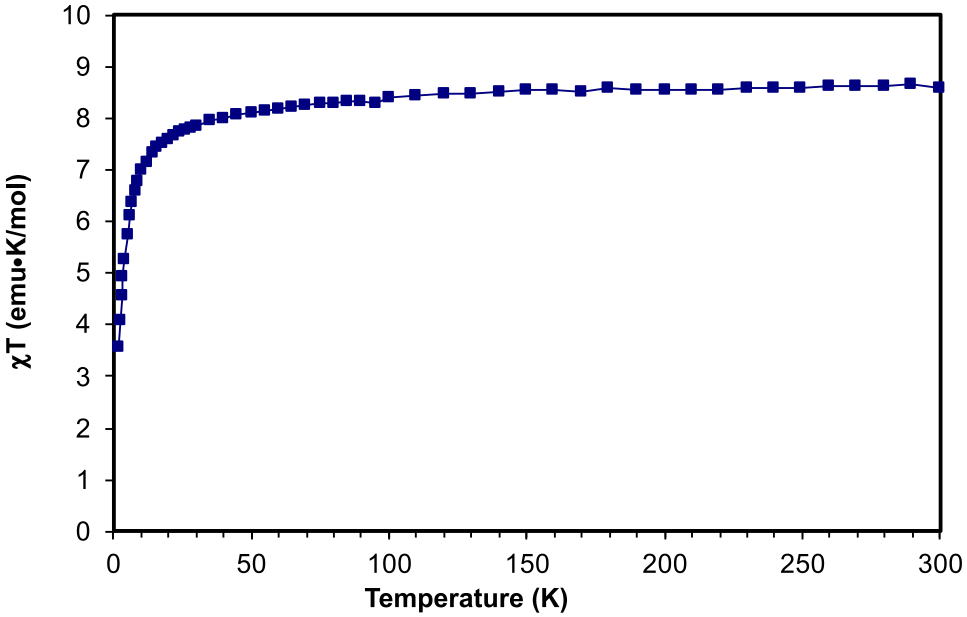

Figure 24. Magnetic susceptibility data of **1.**

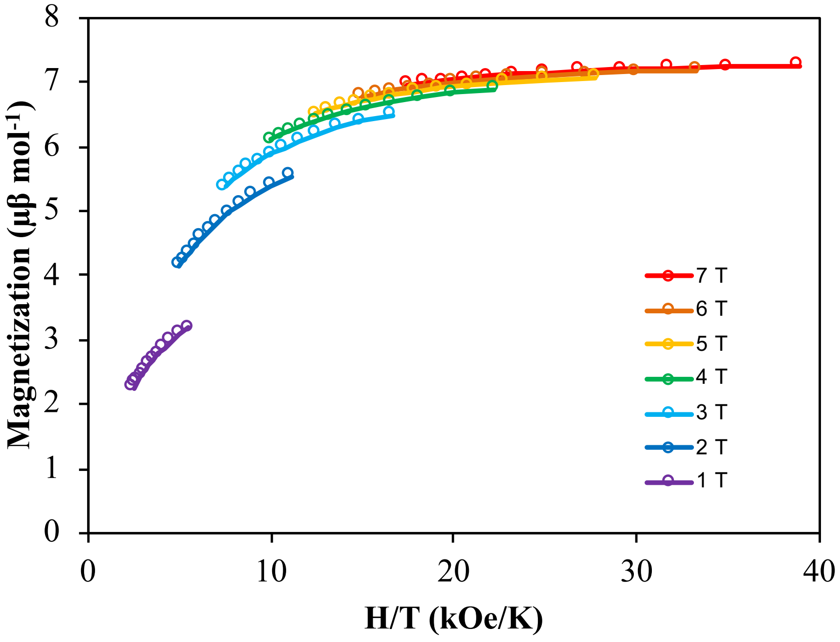

Figure 25. Reduced magnetization plot for **1** with applied fields of 1-7 T in the 2-4 K range.

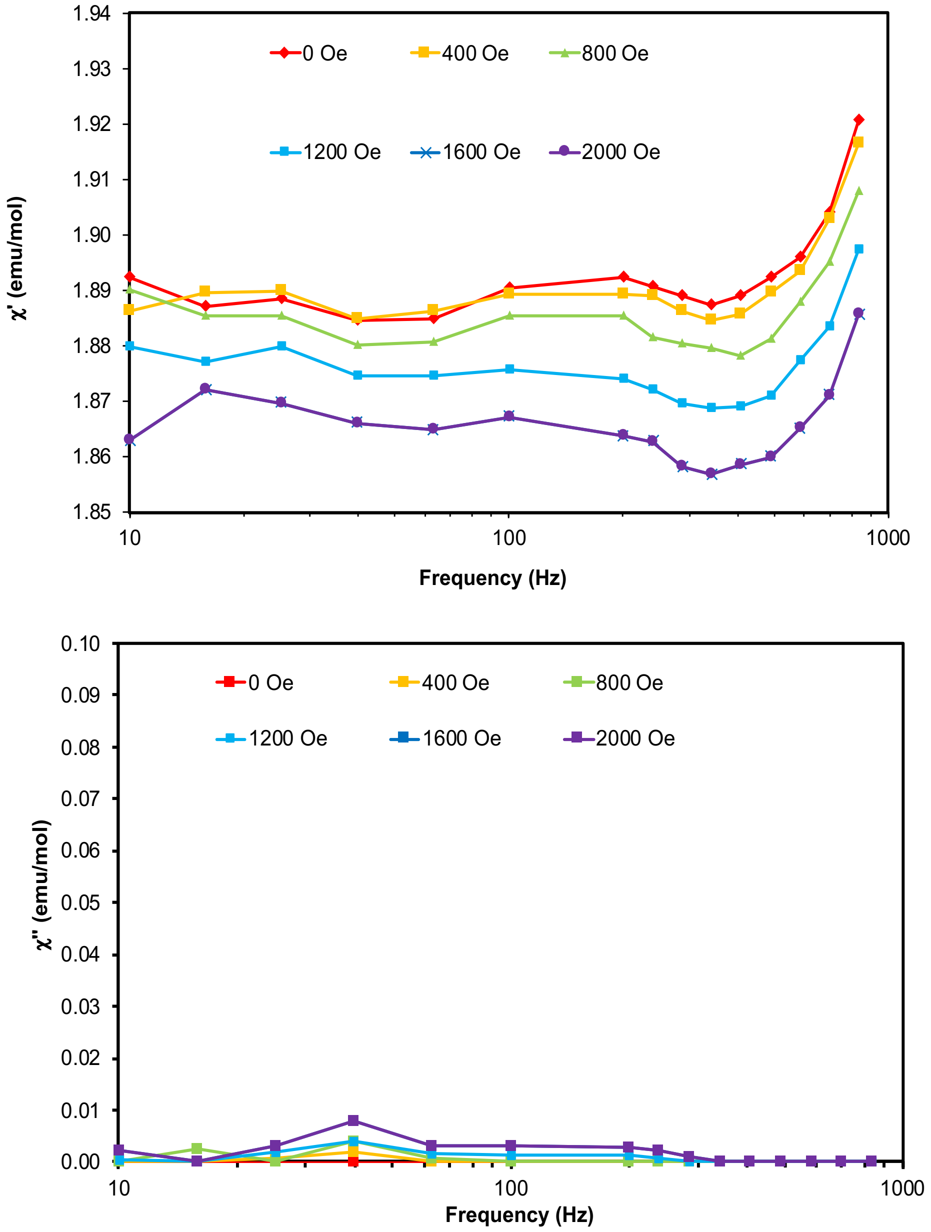

Figure 26. In-phase and out-of-phase susceptibility data for **1**, measured at 2 K with applied static DC fields from 0-2000 Oe.

2 – Variable temperature static DC magnetic susceptibility measurements were performed on crushed crystals of **2** from 300 to 2 K under an applied field of 1000 Oe (Figure 27). The room temperature value of 11.3 cm^3 K mol^{-1} is consistent with one Tb center and one S = ½ Mo^{III} center. The sharp decrease near 2K is likely due to interchain interactions, though it is possible that there is also weak coupling between Mo and Tb. The reduced magnetization plot for **2** (Figure 28) does not have superimposed isofield lines, which indicates that there is magnetic anisotropy in the system. The anisotropy present is likely a combination of exchange anisotropy and single-ion anisotropy from Tb, as well as spin-orbit coupling from Mo^{III}. Alternating current (AC) measurements were performed to evaluate the magnetic dynamics of **2** (Figure 29). A weak signal was observed in χ'', which indicates that there was some slow relaxation of the magnetization, but not at a level expected for SCM behavior.

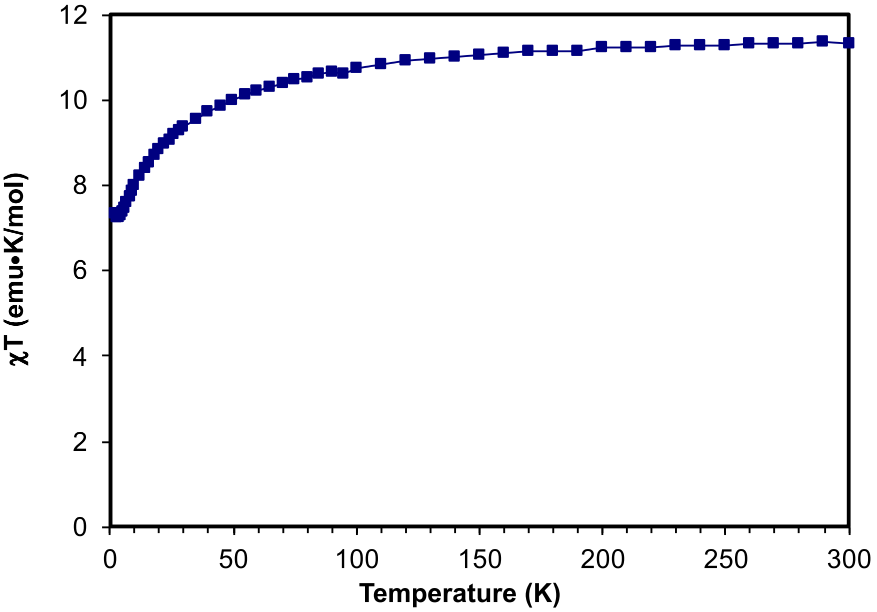

Figure 27. Magnetic susceptibility data of **2.**

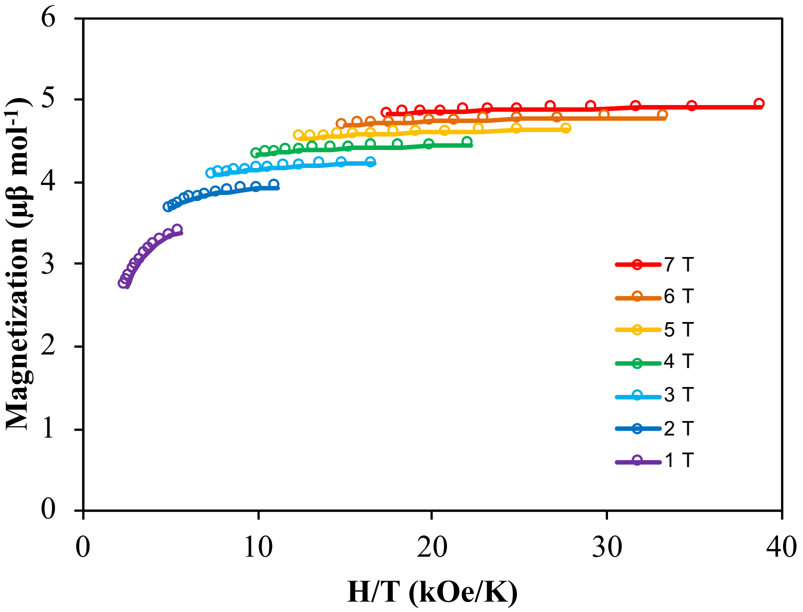

Figure 28. Reduced magnetization plot for **2** with applied fields of 1-7 T in the 2-4 K range.

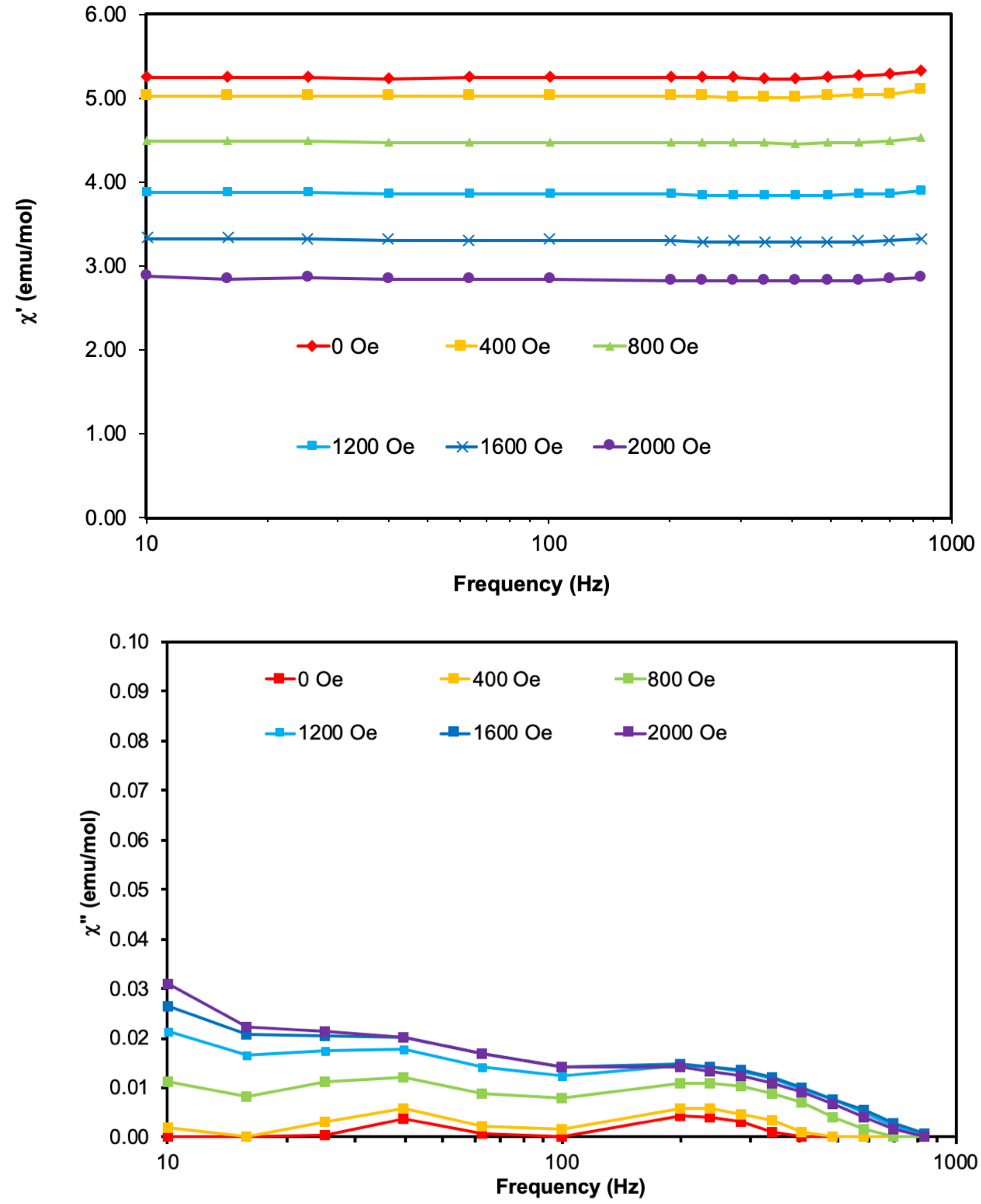

Figure 29. In-phase and out-of-phase susceptibility data for **2**, measured at 2 K with applied static DC fields from 0-2000 Oe.

3 – Variable temperature static DC magnetic susceptibility measurements were performed on crushed crystals of **3** from 300 to 2 K under an applied field of 1000 Oe (Figure 30). The room temperature value of 14.0 cm^3 K mol^{-1} is consistent with one Dy center and one S = ½ Mo^{III} center. The decrease at low temperature can be attributed to antiferromagnetic coupling between Dy and Mo or interchain interactions, including the sharp increase near 4 K. The reduced magnetization plot for **3** (Figure 31) does not have superimposed isofield lines, which shows that there is magnetic anisotropy in the system. The anisotropy present is likely a combination of exchange anisotropy and single-ion anisotropy from Dy, as well as spin-orbit coupling from Mo^{III}. Alternating current (AC) measurements were performed to evaluate the magnetic dynamics of **3** (Figure 32). The beginnings of an out-of-phase signal are be observed, but the frequency limitations of the instrument prevent the peaks from being visible under these conditions. **3** may have some weak magnetic memory behavior under an applied field, but it is not possible to quantify that behavior without the peaks in the data.

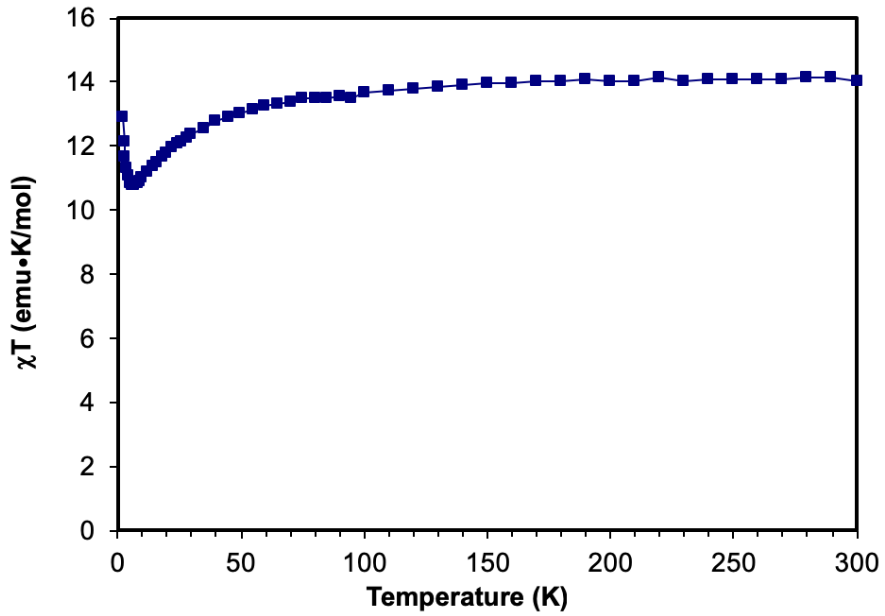

Figure 30. Magnetic susceptibility data of **3**.

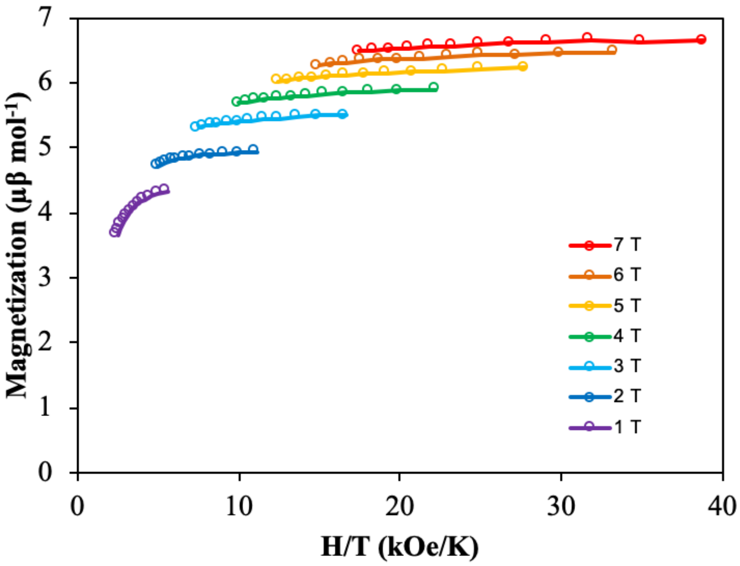

Figure 31. Reduced magnetization plot for **3** with applied fields of 1-7 T in the 2-4 K range.

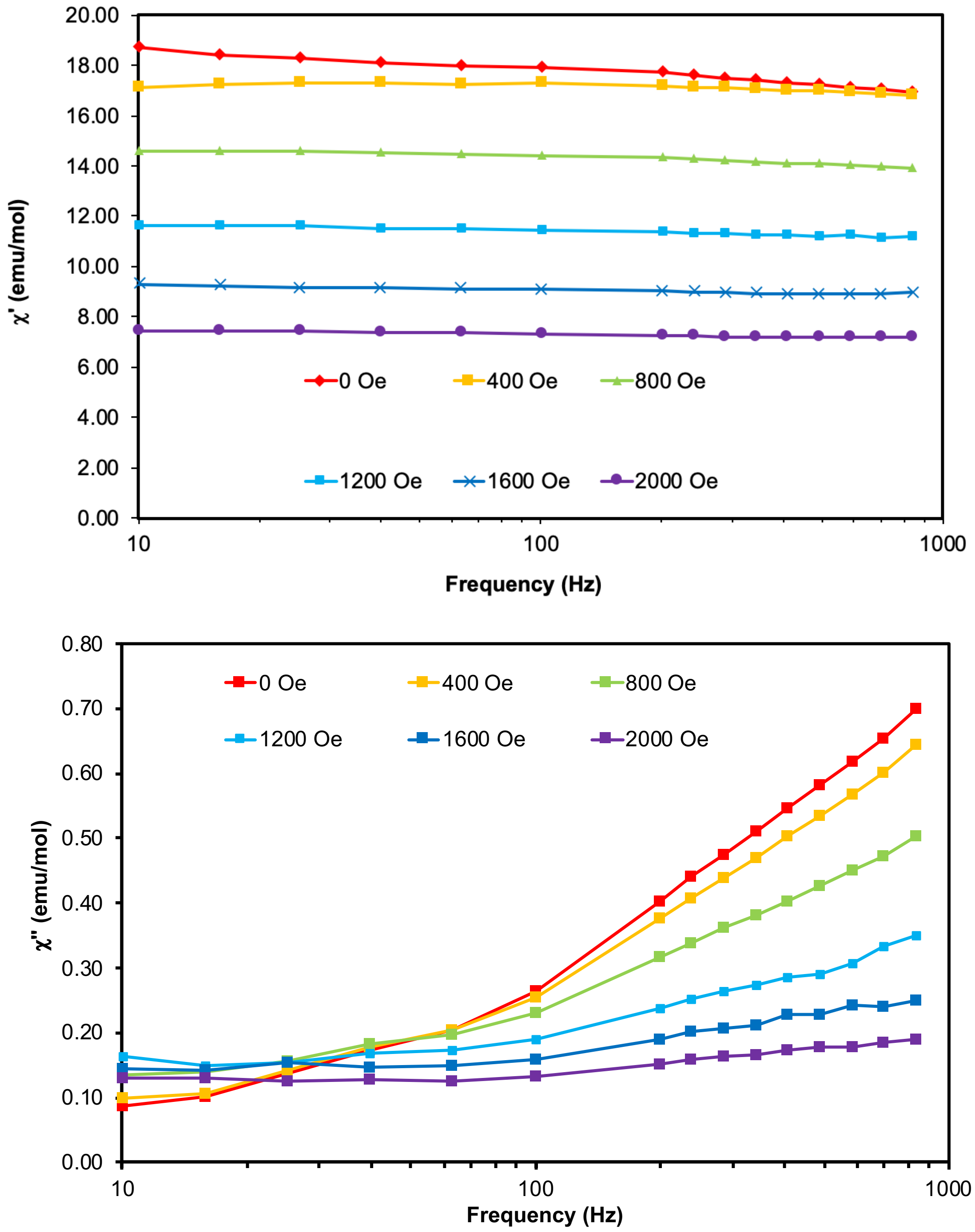

Figure 32. In-phase and out-of-phase susceptibility data for **3**, measured at 2 K with applied static DC fields from 0-2000 Oe.

4 – Variable temperature static DC magnetic susceptibility measurements were performed on crushed crystals of **4** from 300 to 2 K under an applied field of 1000 Oe (Figure 33). The room temperature value of 12.8 cm^3 K mol^{-1} is close to the expectated spin-only value for one Ho center and one S = ½ Mo^{III} center (13.9 cm^3 K mol^{-1}). The decrease at low temperature can be attributed to antiferromagnetic coupling between Ho and Mo or interchain interactions. The reduced magnetization plot for **4** (Figure 34) does not have superimposed isofield lines, which indicates the presence of magnetic anisotropy in the system. The anisotropy present is likely a combination of exchange anisotropy and single-ion anisotropy from Ho, as well as spin-orbit coupling from Mo^{III}. Alternating current (AC) measurements were performed to evaluate the magnetic dynamics of **4** (Figure 35). An out-of-phase signal is not observed for **4**, despite the observation of magnetic anisotropy.

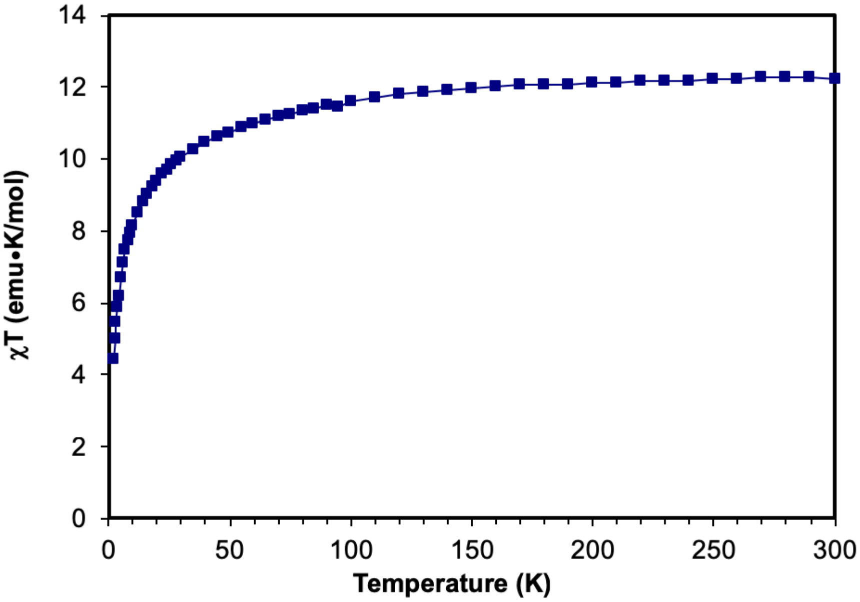

Figure 33. Magnetic susceptibility data of **4**.

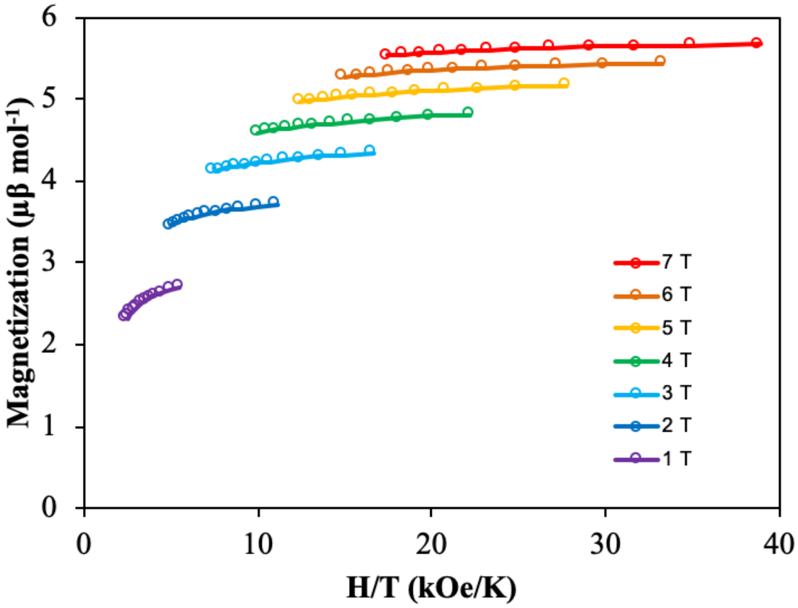

Figure 34. Reduced magnetization plot for **4** with applied fields of 1-7 T in the 2-4 K range.

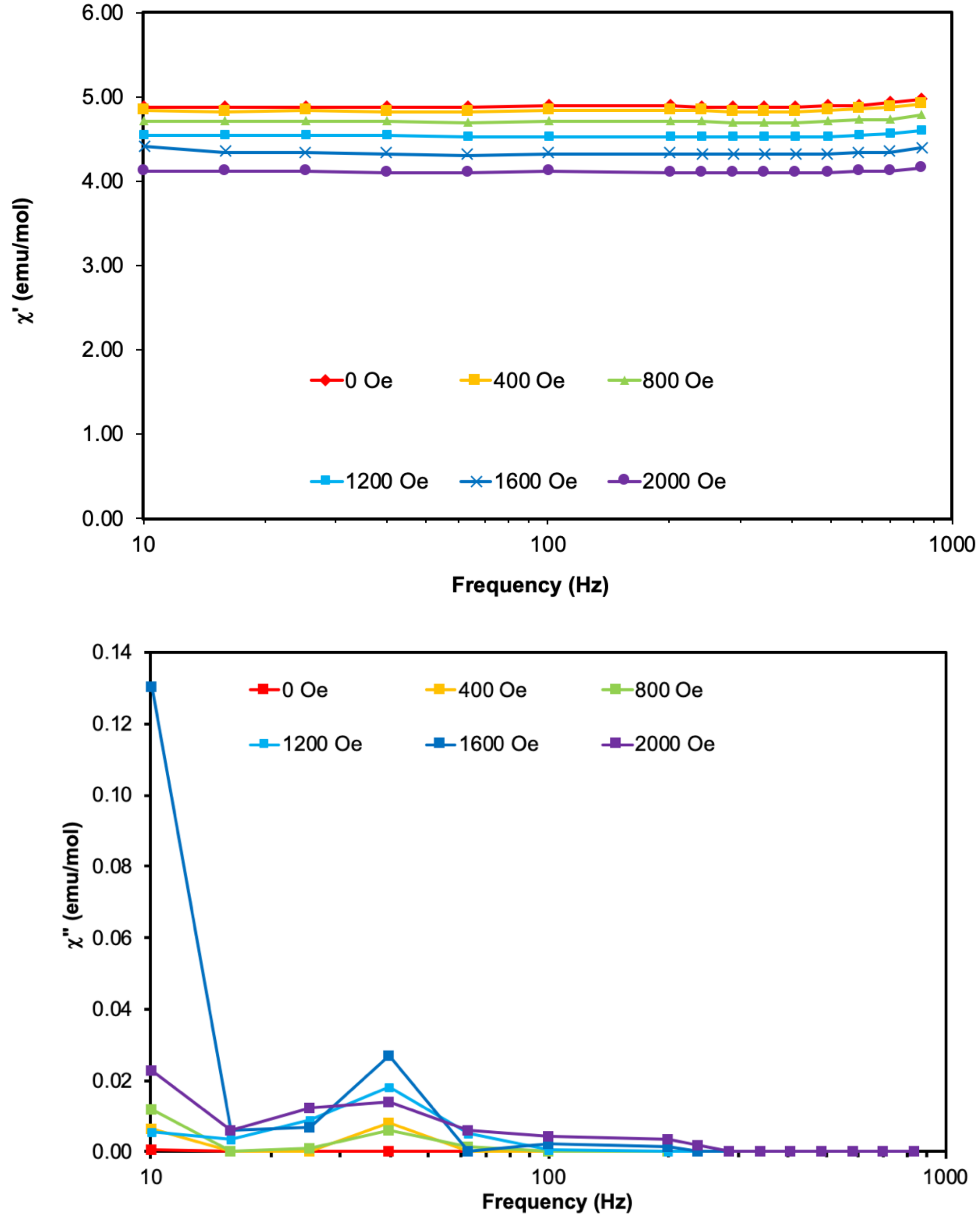

Figure 35. In-phase and out-of-phase susceptibility data for **4**, measured at 2 K with applied static DC fields from 0-2000 Oe.

5 – Variable temperature static DC magnetic susceptibility measurements were performed on crushed crystals of **5** from 300 to 2 K under an applied field of 1000 Oe (Figure 36). The room temperature value of 12.1 cm^3 K mol^{-1} is consistent with expectations for one Er center and one S = ½ Mo^{III} center (11.8 cm^3 K mol^{-1}). The decrease at low temperature can be attributed to coupling between Er and Mo or interchain interactions. The reduced magnetization plot for **5** (Figure 37) does not have superimposed isofield lines, which shows that there is magnetic anisotropy in the system, although less anisotropy than was observed for **3** and **4**. The anisotropy present is likely a combination of exchange anisotropy and single-ion anisotropy from Er, as well as spin-orbit coupling from Mo^{III}. Alternating current (AC) measurements were performed to evaluate the magnetic dynamics of **5** (Figure 38). Like **4**, **5** shows the beginnings of an out-of-phase signal, but it is likewise difficult to quantify the response due to frequency limitations of the SQUID instrument.

The existence of a small amount of anisotropic exchange in these compounds is evident due to the anisotropy present in **1**, but the small amount of anisotropy is insufficient to induce SCM behavior. In the other compounds in the series, if there is anisotropic exchange, it would likely have competing axes with single-ion sources of anisotropy on the lanthanide ions. It is possible that inducing stronger coupling to an orbitally degenerate metal center could lead to anisotropic exchange coupled SMMs or SCMs, but the weak coupling through cyanide is insufficient to induce that change.

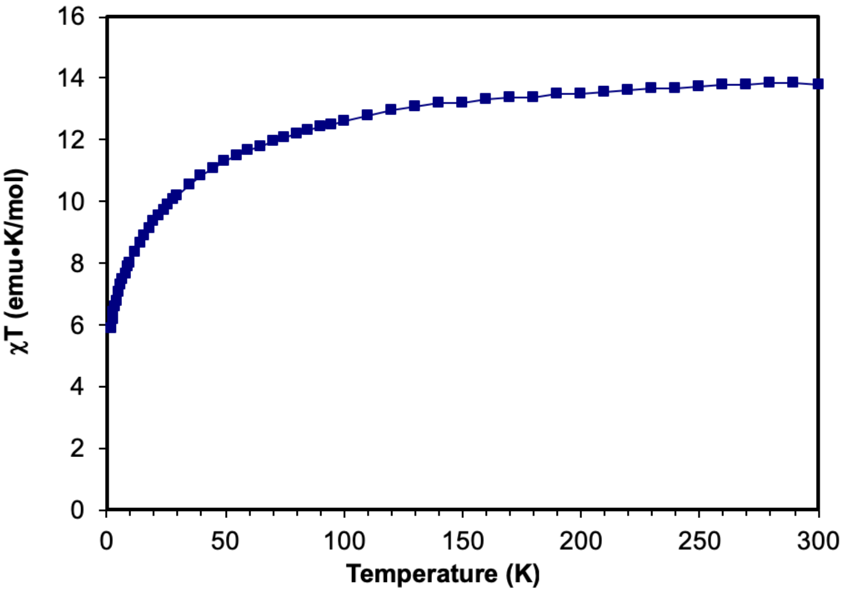

Figure 36. Magnetic susceptibility data of **5**.

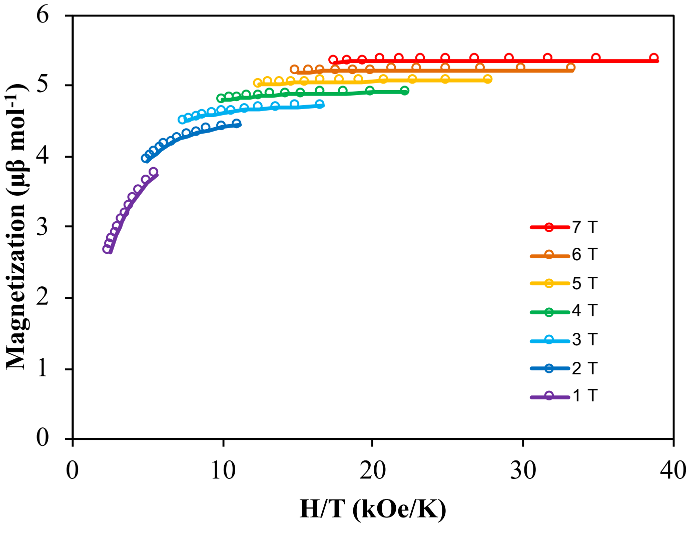

Figure 37. Reduced magnetization plot for **5** with applied fields of 1-7 T in the 2-4 K range.

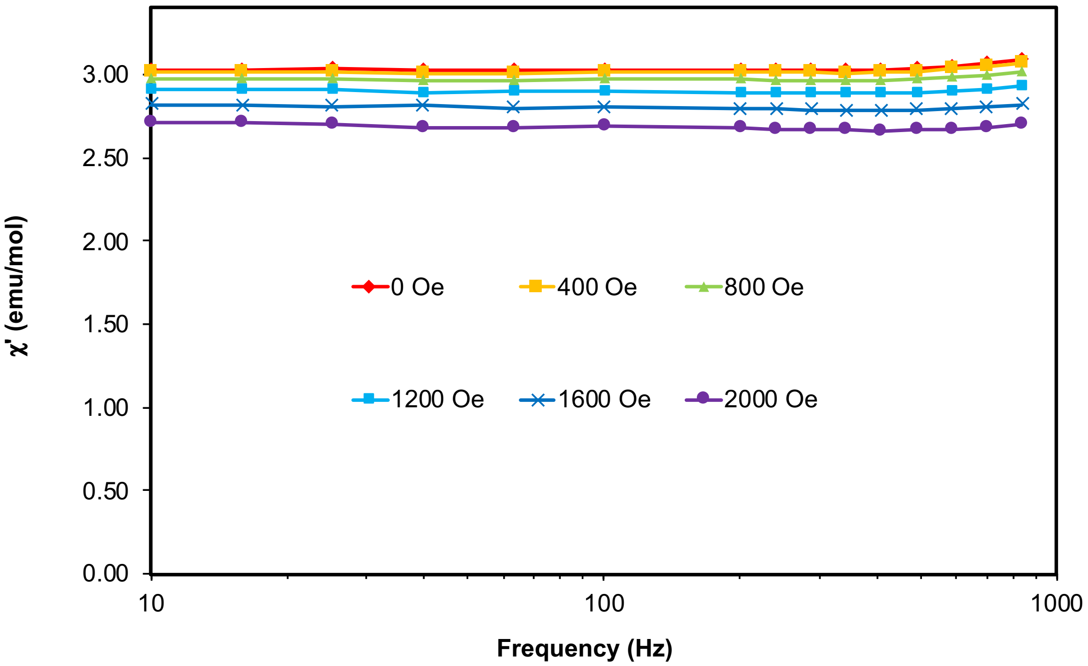

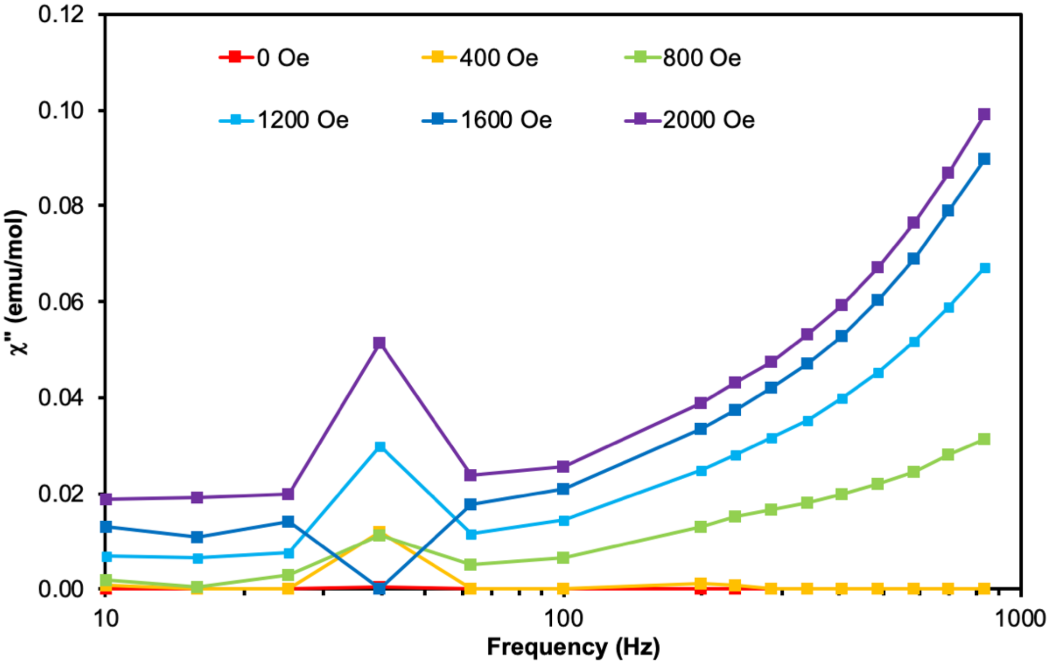

Figure 38. In-phase and out-of-phase susceptibility data for **5**, measured at 2 K with applied static DC fields from 0-2000 Oe.

Conclusions and Future Studies

A family of cyanide bridge $\mathrm{Ln^{III}}$ - $\mathrm{Mo^{III}}$ atoms were synthesized and characterized structurally and magnetic measurements. The inclusion of a 7-coordinate $\mathrm{Mo^{III}}$ center in a chain with a lanthanide ion is novel, but did not lead to SCM behavior in this case. In future studies, other bridging ligands could be used to try to increase the amount of coupling between the lanthanide ion and the molybdenum center. Like in other cases that show anisotropic exchange, the best strategy would likely be strongly coupled $\mathrm{Mo^{III}}$ to $\mathrm{Gd^{III}}$, because there would be no single-ion anisotropy from $\mathrm{Gd^{III}}$ to interfere with the anisotropy from superexchange. In order to increase coupling, a different bridging ligand should be employed. Diamagnetic bridging ligands are known to provide limited coupling between transition metals and lanthanides due to the contracted f-orbitals on lanthanide centers. If a radical bridging ligand was used, it is possible that the coupling would be increased and better magnetic properties could be expected.

CHAPTER III

PREPARATION AND REACTIONS OF SEVEN COORDINATE MOLYBDENUM(III) COMPOUNDS*

Background

The discovery of magnetic bistability for Mn_{12} acetate[1] in 1993 opened the door to wide exploration of magnetic behavior in molecular materials. Cyanide compounds experienced a renaissance in this area owing to the discovery of fascinating magnetic properties in Prussian Blue analogues such as the material $V^{II}[Cr^{III}(CN)_6]_{0.86}\cdot 2.8\ H_2O$, which exhibits magnetic ordering above room temperature.[23] Over the past twenty years, hexacyanometallates, octacyanometallates, as well as heteroleptic cyanide precursors have been studied extensively vis-à-vis their capacity to be incorporated into extended networks as well as discrete molecules.[33,75-76] In the latter category, single molecule magnets (SMMs) prepared from cyanometallate building blocks are especially intriguing due to their potential applicability to quantum computing, data storage, and spintronics.[9,11,22,77] SMMs function as nanomagnets with a thermal energy barrier to reversal of their magnetization. Even in cases with record coupling[78-79] and large ground state spin values,[16] however, SMM behavior is still relatively elusive in cyanide-bridged materials. Investigating

---

*Data, figures, and text in this chapter were adapted with permission from reference 97, copyright 2019 Royal Society of Chemistry.

underexplored geometries and architectures can aid in the understanding of including how to improve their magnetic properties.

Molecular wheels are well-known in the magnetism and coordination chemistry communities, with many different bridging ligands having been used to obtain cyclic architectures. Among these wheels are examples that contain lanthanides and transition metals with a wide variety of bridging ligands including azides, carboxylates, polyolates, polyamines, oxides, polyols, and hydroxides.[80-88] Wheel examples with cyanide, however, are rather limited,[16,89-94] despite the interesting magnetic phenomena observed for some of those compounds. One of these molecules, $[Mn^{III}(salen)]_6[Fe^{III}(bpmb)(CN)_2]_6 \bullet 7H_2O$ exhibits magnetic hysteresis consistent with SMM behavior.[90] Another interesting molecule reported by the Dunbar group, namely $[Mn(dpop)(H_2O)_2]_2[\{Mo(CN)_7\}_8\{Mn(dpop)\}_{10}\{Mn(dpop)(H_2O)\}_4]\cdot xH_2O$ (dpop = 2,13-dimethyl-3,6,9,12,18-pentaazabicyclo-[12.3.1]octadeca-1(18),2,12,14,16-pentaene), has the largest spin ground state for a cyanide bridged molecule.[16] Based on that result and the dearth of cyanide-bridged wheels, pursuit of other wheel architectures utilizing $[Mo^{III}(CN)_7]^{4-}$ as a building block is warranted.

The S = ½ anion $[Mo^{III}(CN)_7]^{4-}$ has attracted interest in the area of cyanide magnetism due to its five-fold symmetry and atypical coordination geometries in magnetic systems. Early studies by Kahn and coworkers focused on the incorporation of $[Mo(CN)_7]^{4-}$ into extended cyanide-bridged networks. The seven-coordinate geometry precludes the formation of the highly symmetric networks typically observed for hexa- and octacyanometallates and leads to increased magnetic anisotropy.[55,57] Examples of molecules containing the $[Mo^{III}(CN)_7]^{4-}$ moiety are scarce, however; results from our laboratories have provided the only examples that satisfy the conditions for SMMs, *viz.* the Mo^{III} center having pseudo-D_{5h} geometry and a 3d metal being coordinated to the apical cyanide ligands which maximizes Ising anisitropy.[28,38-39,95] While one would not expect to preserve the D_{5h} symmetry when incorporating $[Mo^{III}(CN)_7]^{4-}$ into wheel architectures, isolation of new cyclic molecules with this anion allows for more data to be added to the scarce information about the magnetism of this building block. One family of wheels that incorporates homoleptic cyanometallates have the formula $[M^{IV}(CN)_8]_6[Ni(L)]_{12}(H_2O)_6$ (M = Nb, Mo, or W). Weak antiferromagnetic interactions between the Ni centers in $[Mo^{IV}(CN)_8]_6[Ni(L)]_{12}(H_2O)_6$[92] and antiferromagnetic interactions between Nb and Ni in $[Nb^{IV}(CN)_8]_6[Ni(L)]_{12}(H_2O)_6$ were reported in the original publications.[94] The magnetic properties of $[W^{IV}(CN)_8]_6[Ni(L)]_{12}(H_2O)_6$ were not reported.[93]

In this report, the synthesis of the Mo^{III} analogue $[Mo^{III}(CN)_7]_6[Ni(L)]_{12}(H_2O)_6$ (**7**) is shown to be possible by emulating reaction conditions used to prepare $[Mo^{IV}(CN)_8]_6[Ni(L)]_{12}(H_2O)_6$ (**8**). The Mo^{IV} analogue, **8** was also re-synthesized and measured to directly compare data for the two molecules. A new, simpler procedure for the synthesis of $K_4[Mo^{III}(CN)_7]\cdot 2H_2O$ (**6**)[96] was also developed. Characterizing the new wheel compound reignited interest in syntheses that might yield proper geometries for anisotropic exchange with Mo^{III}. As previously stated, the D_{5h} geometry is critical to the observation of Ising-type anisotropic exchange. Rather than using $[Mo^{III}(CN)_7]^{4-}$ as a building block and hoping to preserve its pentagonal bipyramidal geometry, it would significantly aid the efforts to make polynuclear SMMs if a starting material existed that would naturally enforce such a geometry. With that goal in mind, $Mo^{III}Cl_3(THF)_3$ was reacted with the organic Schiff base ligand DAPB ((2*E*,12*E*)-2,13-dimethyl-6,9-dioxa-3,12-diaza-1(2,6)-pyridinacyclotridecaphane-2,12-diene).[97-98] The reaction led to the isolation of the product $[Mo^{III}DAPB(CN)_2]^-$, which is an exciting new building block that optimizes the geometry of the orbitally degenerate Mo^{III} center, satisfying the conditions for anisotropic exchange. DAPB has been used in a similar fashion before, but not with an orbitally degenerate metal center.[99] Using a similar strategy with Mo^{III} should enable new complexes to be prepared that exhibit Ising-type anisotropic exchange.

Experimental Details

Synthesis

Syntheses were carried out under air free conditions using a nitrogen-filled glove box or Schlenk-line outfitted with argon gas. The solvents were deoxygenated by sparging with argon gas and the dry EtOH was dried over Mg and I_2. Diethyl ether was purified using an MBRAUN purification system. $Mo^{III}Cl_3(THF)_3$, $Ni(L)(ClO_4)_2$, and DAPB were prepared by literature methods[97-98,100-101]; all other chemicals were purchased from commercial sources and used without further purification unless otherwise indicated.

$K_4[Mo^{III}(CN)_7]\cdot 2H_2O$ (6)

A 3.2g (7.64 mmol) sample of $Mo^{III}Cl_3(THF)_3$ and 4.4g (66.9 mmol) of KCN were added to a flask containing 40 mL of H_2O and heated to 70°C for 12 h to yield a dark orange solution. MeOH was subsequently added until the solution became slightly cloudy. After left to stand overnight at 25°C, X-ray quality dark olive-green crystals were isolated (2.48g, 69% yield). IR (ν for C≡N): 2115sh, 2101s, 2067vs cm^{-1}.

$[Mo^{III}(CN)_7]_6[Ni(L)]_{12}\cdot 24H_2O$ (7)

A 25mg (0.05 mmol) sample of $K_4[Mo^{III}(CN)_7]\cdot 2H_2O$ was dissolved in 6 mL of H_2O. A separate sample (25mg, 0.05 mmol) of Ni(L) was dissolved in 6 mL of H_2O and added dropwise to the solution of K4$[Mo^{III}(CN)_7]\cdot 2H_2O$. After standing overnight, the dark orange needle crystals were collected by filtration and washed with H_2O and Et_2O, 27mg, 50% yield. Samples were dried under vacuum prior to submission for elemental analysis and SQUID measurements. Found: C, 44.94; N, 21.34; H, 5.17%. Calc. for $[Mo^{III}(CN)_7]_6[Ni(L)]_{12}\cdot 24H_2O$: C, 45.15; N, 21.35; H, 5.33%. IR (ν for C≡N): 2090m, 2077m, 2042sh, 2033m cm^{-1}.

$[Mo^{IV}(CN)_8]_6[Ni(L)]_{12}\cdot 30H_2O$ (8)

A 65 mg sample of $K_4[Mo^{IV}(CN)_8]\cdot 2H_2O$ was dissolved in 8 mL of H_2O. A separate 50 mg sample of Ni(L) was dissolved in 8 mL of H_2O and added dropwise to the solution of $K_4[Mo^{IV}(CN)_8]\cdot 2H_2O$. After standing overnight, dark yellow needle crystals were collected by filtration and washed with H_2O and Et_2O, 34 mg, 32% yield. The sample was dried under vacuum prior to submission for elemental analysis and SQUID measurements. Found: C, 44.40; N, 21.74; H, 5.22%. Calc for

$[Mo^{IV}(CN)_8]_6[Ni(L)]_{12}\cdot 30H_2O$: C, 44.39; N, 21.79; H, 5.29%. IR (ν for C≡N): 2150sh, 2144m, 2131m, 2119w, 2100s, 1626m, 1579m cm^{-1}.

$Mo^{IV}DAPBCl_2$ (9)

A 1.0 g sample (2.12 mmol) of $MoCl_3(THF)_3$ and an 850 mg sample (2.12 mmol) of $DAPBH_2$ were added to a Schlenk fask with 50 mL MeCN. After refluxing for about 2 hours, a black, crystalline powder was observed in the flask. It was left to stir for another hour and the X-ray quality crystals were filtered in air and washed with MeCN, 1.0 g, 83% yield.

$(NEt_4)[Mo^{III}(DAPB)(CN)_2]$ (10)

A 2.72 g (0.48 mmol) sample of $Mo^{IV}(DAPB)Cl_2$ was placed in a Schlenk flask with a 225 mg (1.44 mmol) sample of $(NEt_4)CN$ and 20 mL MeCN. The mixture was subjected to reflux for 12 hours, after which there was a green solution and some dark particulate matter. The solution was filtered to separate the filtrate and the solid. After slow diffusion of Et_2O into the filtrate, a small number of X-ray quality, dark green crystals were observed.

$K[Mo^{III}(DAPB)(CN)_2]$ (11)

A 100 mg (0.177 mmol) sample of $Mo^{IV}DAPBCl_2$ was placed in a Schlenk flask with 23 mg (0.354 mmol) KCN and 30 mL of dry ethanol. The mixture was refluxed for 12 hours, which resulted in a yellow solution with brown solid. After filtration, the filtrate was subjected to slow diffusion with Et_2O and Xray quality, dark brown crystals were isolated, 13 mg, 12.5% yield.

Crystallography

Single crystals of each complex were selected under Paratone® oil with a MiTGen microloop. Reflection data were collected on a Bruker D8-VENTURE diffractometer equipped with a IµS Cu microsource (λ = 1.54178 Å) or a Bruker D8-QUEST diffractometer equipped with a IµS Mo microsource (λ = 0.71073 Å) under a stream of N2 gas a 100 K. The frames were integrated and a semi-empirical absorption correction was applied using SADABS[68] within the software package included in the APEX3 software suite.[69] The structure was solved using SHELXT[70] and refined using SHELXL;[71] OLEX2 was used as an interface for the solution and refinement.[72] Small Q-peaks in the structure that were consistent with the behavior of disordered solvent were removed using the SQUEEZE routine of the PLATON software package.[73] Hydrogen atoms were placed in calculated positions.

$[Mo^{III}(CN)_7]_6[Ni(L)]_{12}\cdot 24H_2O$ (7)

Compound **7** crystallizes in $P\overline{1}$ with a unit cell that is metrically similar to that of **8** which crystallizes in $R\overline{3}$. The molecule of **7** resides on a crystallographic inversion center with one-half of the complex in the asymmetric unit (Figure 39). The structure consists of six $[Mo^{III}(CN)_7]^{4-}$ moieties bridged to six [Ni(L)] moieties in an alternating arrangement to give a wheel motif. The remaining six $[Ni(L)]^{2+}$ act as capping ligands for the wheel with one coordinated water in the Ni axial position opposite the cyanide ligand. The coordination geometry around the Mo^{III} centers was evaluated using the SHAPE program, which calculates a continuous shape measurement (CShM) based on the positions of the atoms relative to their positions in ideal geometries (closer to 0 is a better match).[102-103] The coordination geometries of the Mo centers are best described as capped trigonal prismatic. Mo3 is a particularly good fit for that geometry and the results of those calculations are compiled in Table 7. The angles between the equatorial cyanide ligands range from 71.9(4)° to 76.4(3)°, which are close to the 72° for a perfect pentagon. OLEX2 was used to calculate a mean plane of the equatorial cyanide ligands on each Mo^{III} center in **7**; the rmsd values for each of those planes are 0.549, 0.535, and 0.579 for Mo1-Mo3, further showing that the cyanide ligands are distorted compared to a perfect pentagonal arrangement. The Ni^{II} centers all adopt an approximately octahedral geometry, with the four equatorial positions being occupied by the N atoms of L and the axial positions filled with either two cyanide ligands (for the Ni atoms in the ring), or one cyanide ligand and one water ligand (for the Ni atoms on the outside). Additional information regarding the structure can be found in Table 8.

Table 7. SHAPE results for crystallographically independent Mo^{III} centers in **7**.

Mo Center	CShM for Pentagonal Bipyramidal	CShM value for Capped Trigonal Prism
1	2.530	2.316
2	2.441	2.233
3	3.849	0.924

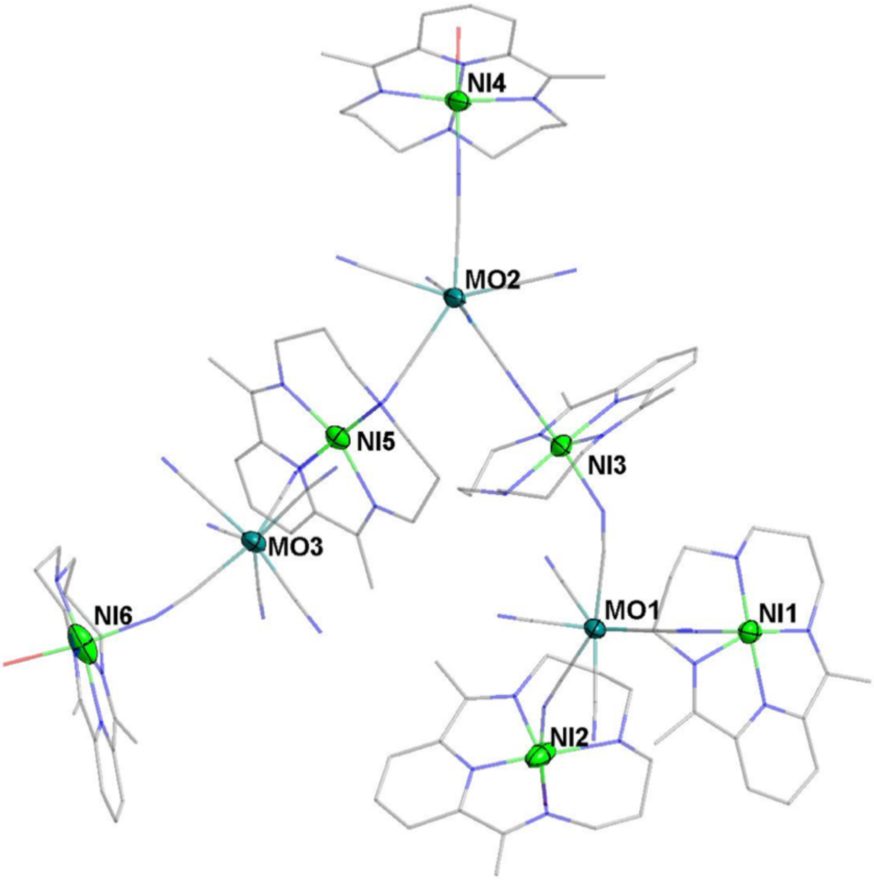

Figure 39. Local geometry of the molybdenum atoms in **7** (Mo1, Mo2, and Mo3 left to right).

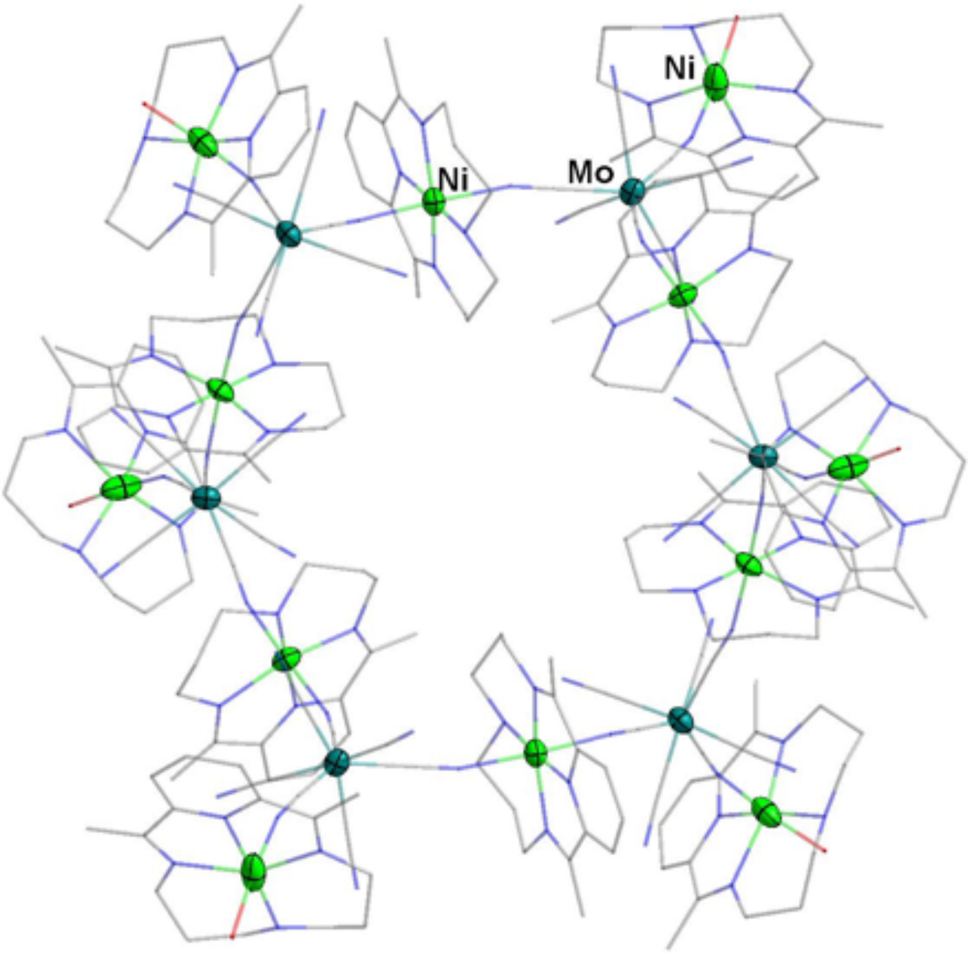

Figure 40. Structure of **7**. The nickel atoms are green, molybdenum atoms are teal, carbon atoms are grey, nitrogen atoms are blue, and oxygen atoms are red. Hydrogen atoms are omitted for the sake of clarity.

Table 8. Crystal data and structure refinement for **7**.

Identification code	$\mathbf{Mo_6^{III}Ni_{12}}$
Empirical formula	$C_{222}H_{276}Mo_6N_{90}Ni_{12}O_6$
Formula weight	5581.47
Temperature/K	110.0
Crystal system	triclinic
Space group	$P\bar{1}$
a/Å	20.8632(17)
b/Å	20.9777(19)
c/Å	21.0033(18)
α/°	105.168(3)
β/°	105.407(2)
γ/°	104.914(2)
Volume (Å^3)	8008.0(12)
Z	1
ρ_{calc}g (cm^3)	1.157
μ (mm^{-1})	0.968
F (000)	2874.0
Crystal size (mm^3)	0.5 × 0.2 × 0.05
Radiation	MoKα (λ = 0.71073)
2Θ range for data collection/°	4.068 to 48.602
Index ranges	$-24 \leq h \leq 24$, $-24 \leq k \leq 24$, $-24 \leq l \leq 24$
Reflections collected	89054
Independent reflections	25768 [R_{int} = 0.0848, R_{sigma} = 0.0814]
Data/restraints/parameters	25768/2764/2122
Goodness-of-fit^a on F^2	1.030
Final R indexes [I>=2σ (I)]	$R_1{}^b$ = 0.0881, $wR_2{}^c$ = 0.1838
Final R indexes [all data]	$R_1{}^b$ = 0.1361, $wR_2{}^c$ = 0.2110
Largest diff. peak/hole / e Å^{-3}	0.96/-1.01

^{a}Goodness-of-fit = $\{\Sigma [w(Fo^2 - Fc^2)^2]/(n-p)\}^{1/2}$, where n is the number of reflections and p is the total number of parameters refined.

^{b}R = $\Sigma \| Fo | - | Fc \| / \Sigma | Fo |$

^{c}wR = $\{\Sigma [w(Fo^2 - Fc^2)^2] / \Sigma w(Fo^2)^2]\}^{1/2}$

$[Mo^{IV}(CN)_8]_6[Ni(L)]_{12}\cdot 30H_2O$ (8)

The structure of **8** was previously reported by the Wang group in 2017.[92] The structure was collected at room temperature, and for the sake of direct comparison to **7**, it was re-collected at 110 K. The structure is superficially similar to **7**, and is reported in the rhombohedral setting to facilitate comparison of its unit cell to **7** (Table 9). The unit cell of this data is slightly smaller than the cell of the previously reported data, as might be expected from the lowered temperature. More details can be found in Table 10.

Table 9. Comparison of the unit cell parameters for **7** and **8**.

Unit cell parameter	**8**	**7**
Space Group	$R\bar{3}$	$P\bar{1}$
a (Å)	21.1191(3)	20.8632(17)
b (Å)	21.1191(3)	20.9777(19)
c (Å)	21.1191(3)	21.0033(18)
α (°)	105.6515(6)	105.168(3)
β (°)	105.6515(6)	105.407(2)
γ (°)	105.6515(6)	104.914(2)
V (Å^3)	8116.0(2)	8008.1(12)

Table 10. Crystal data and structure refinement for **8**.

Identification code	$\mathbf{Mo_6^{IV}Ni_{12}}$
Empirical formula	$C_{38}H_{46}MoN_{16}Ni_2O$
Formula weight	956.27
Temperature/K	100.0
Crystal system	trigonal
Space group	$R\overline{3}$
a/Å	33.6548(8)
b/Å	33.6548(8)
c/Å	24.8190(6)
α/°	90
β/°	90
γ/°	120
Volume/Å^3	24344.9(13)
Z	18
ρ_{calc}g (cm^3)	1.174
μ (mm^{-1})	3.005
F(000)	8856.0
Crystal size (mm^3)	0.8 × 0.2 × 0.2
Radiation	CuKα (λ = 1.54178)
2Θ range for data collection (°)	7.034 to 140.406
Index ranges	$-41 \leq h \leq 41$, $-41 \leq k \leq 35$, $-30 \leq l \leq 30$
Reflections collected	84785
Independent reflections	10294 [R_{int} = 0.0522, R_{sigma} = 0.0260]
Data/restraints/parameters	10294/1/543
Goodness-of-fit^a on F^2	1.051
Final R indexes [I>=2σ (I)]	R_1^b = 0.0346, wR_2^c = 0.0863
Final R indexes [all data]	R_1^b = 0.0418, wR_2^c = 0.0894
Largest diff. peak/hole / e Å^{-3}	0.67/-0.43

[a] Goodness-of-fit = $\{\Sigma [w(Fo^2 - Fc^2)^2]/(n-p)\}^{1/2}$, where n is the number of reflections and p is the total number of parameters refined.

[b] $R = \Sigma \| Fo | - | Fc \| / \Sigma | Fo |$

[c] $wR = \{\Sigma [w(Fo^2 - Fc^2)^2] / \Sigma w(Fo^2)^2]\}^{1/2}$

$Mo^{IV}DAPBCl_2$ (9)

Compound **9** crystallizes in the space group $P2_1/C$. The structure was previously reported by the Yagubskii group,[104] and they noted that the structure is remarkably close to pentagonal bipyramidal. There are no anions in the structure; the ligand, $DAPBH_2$, becomes deprotonated during the reaction, leading to the formation of a neutral compound. The bond lengths to the two Cl^- ligands are 2.3868(14) Å and 2.3912(14) Å. More details can be found in Table 11.

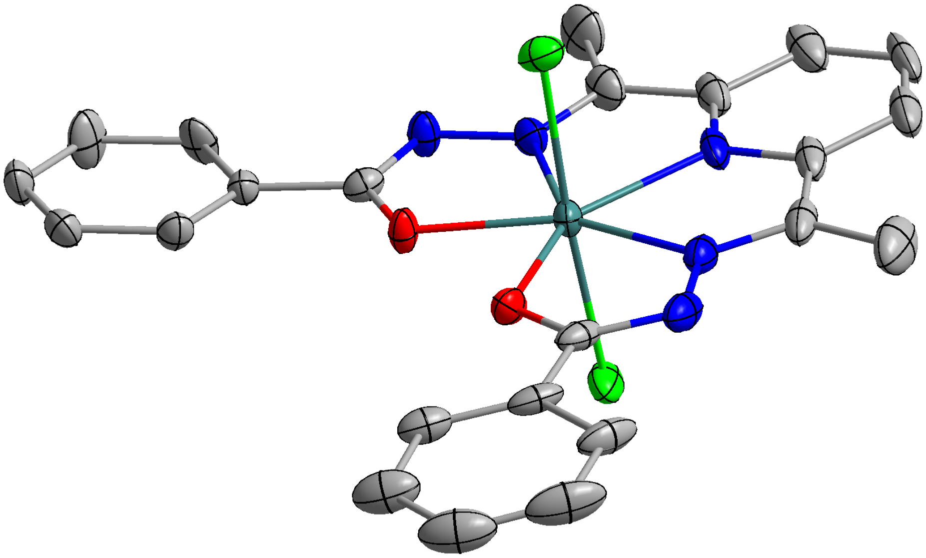

Figure 41. Crystal structure of **9**. Ellipsoids are drawn at the 50% probability level.

Table 11. Crystal data and structure refinement for **9**.

Identification code	$Mo^{IV}DAPBCl_2$
Empirical formula	$C_{23}H_{19}Cl_2MoN_5O_2$
Formula weight	564.27
Temperature/K	138.0
Crystal system	monoclinic
Space group	$P2_1/c$
a/Å	8.5335(3)
b/Å	13.9276(7)
c/Å	20.0337(9)
α/°	90
β/°	99.509(2)
γ/°	90
Volume/Å^3	2348.31(18)
Z	4
ρ_{calc}g/cm^3	1.596
μ/mm^{-1}	0.817
F(000)	1136.0
Crystal size/mm^3	.3 × .3 × .6
Radiation	MoKα (λ = 0.71073)
2Θ range for data collection/°	4.84 to 51.408
Index ranges	$-10 \leq h \leq 10$, $-17 \leq k \leq 15$, $-24 \leq l \leq 24$
Reflections collected	26070
Independent reflections	4466 [R_{int} = 0.1037, R_{sigma} = 0.0549]
Data/restraints/parameters	4466/0/300
Goodness-of-fit[a] on F^2	1.187
Final R indexes [I>=2σ (I)]	$R_1{}^b$ = 0.0568, $wR_2{}^c$ = 0.0976
Final R indexes [all data]	$R_1{}^b$ = 0.0841, $wR_2{}^c$ = 0.1059
Largest diff. peak/hole / e Å^{-3}	0.72/-0.81

[a] Goodness-of-fit = $\{\Sigma [w(Fo^2 - Fc^2)^2]/(n-p)\}^{1/2}$, where n is the number of reflections and p is the total number of parameters refined.

[b] $R = \Sigma \| Fo | - | Fc \| / \Sigma | Fo |$

[c] $wR = \{\Sigma [w(Fo^2 - Fc^2)^2] / \Sigma w(Fo^2)^2]\}^{1/2}$

$(NEt_4)[Mo^{III}(DAPB)(CN)_2]$ (10)

10 crystallizes in the space group $Pna2_1$. The geometry of the Mo^{III} center is still close to pentagonal bipyramidal, but the DABP ligand lies less flat than it does in **9**. The $[NEt_4]^+$ moiety is disordered and was able to be modeled in two positions. The Mo-C bonds to the cyanide ligands are 2.177(7) Å and 2.172(6) Å, respectively. More information can be found in Table 12, and the structure is shown in Figure 42.

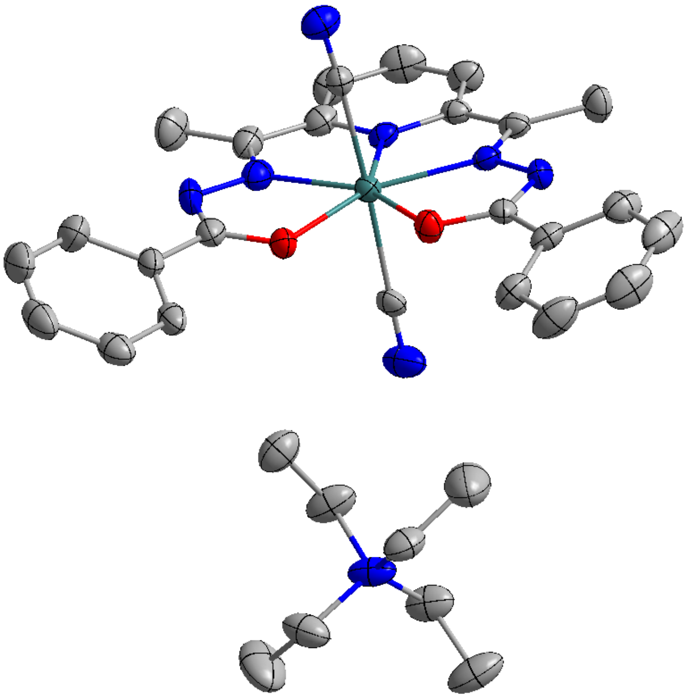

Figure 42. Crystal structure of **10**. Only one configuration of the disordered $[NEt_4]^+$ is shown. Ellipsoids are drawn at the 50% probability level.

Table 12. Crystal data and structure refinement for **10**.

Identification code	$(NEt_4)[Mo^{III}(DAPB)(CN)_2]$
Empirical formula	$C_{33}H_{41}MoN_8O_2$
Formula weight	677.68
Temperature/K	120
Crystal system	orthorhombic
Space group	$Pna2_1$
a/Å	22.609(3)
b/Å	10.8318(16)
c/Å	13.0487(15)
α/°	90
β/°	90
γ/°	90
Volume/Å^3	3195.5(8)
Z	4
ρ_{calc}g/cm^3	1.409
μ/mm^{-1}	0.454
F(000)	1412.0
Crystal size/mm^3	0.576 × 0.106 × 0.076
Radiation	MoKα (λ = 0.71073)
2Θ range for data collection/°	4.768 to 52.202
Index ranges	$-26 \leq h \leq 27, -13 \leq k \leq 13, -16 \leq l \leq 16$
Reflections collected	67594
Independent reflections	6310 [R_{int} = 0.1095, R_{sigma} = 0.0480]
Data/restraints/parameters	6310/190/480
Goodness-of-fit[a] on F^2	1.140
Final R indexes [I>=2σ (I)]	R_1[b] = 0.0462, wR_2[c] = 0.0862
Final R indexes [all data]	R_1[b] = 0.0641, wR_2[c] = 0.0920
Largest diff. peak/hole / e Å^{-3}	0.34/-0.56
Flack parameter	-0.005(15)

[a] Goodness-of-fit = $\{\Sigma [w(Fo^2 - Fc^2)^2]/(n-p)\}^{1/2}$, where n is the number of reflections and p is the total number of parameters refined.

[b] $R = \Sigma \| Fo | - | Fc \| / \Sigma | Fo |$

[c] $wR = \{\Sigma [w(Fo^2 - Fc^2)^2] / \Sigma w(Fo^2)^2]\}^{1/2}$

K[Mo^{III}(DAPB)(CN)$_2$] (11)

Compound **11** crystallizes in the space group P2$_1$/n. There are two [Mo^{III}(DAPB)]$^-$ fragments in the unit cell. The geometry of the Mo^{III} centers is slightly distorted due to the presence of the K$^+$ ions, which bend the cyanide ligands away from the ideal geometry – the angle between these ligands is 167.584° and 167.060° for the two complexes in the unit cell, respectively, which is a significant deviation from the ideal of 180°. The Mo-C bond lengths for these axial cyanide ligands are 2.16(2) Å, 2.20(2) Å, 2.20(2) Å, and 2.134(18) Å. There are large Q-peaks that appear to correspond to solvent molecules that act as ligands on K$^+$ – all efforts to model those peaks resulted in chemically unreasonable refinements. The difficulty in modelling those peaks is due to disorder of the ligands, whose likely identity is EtOH. Additional details can be found in Table 13. The structure is shown from two angles in Figure 43.

Table 14 contains some comparisons of the bond angles in **9, 10** and **11**. Consistently, the O-Mo-O bond angle is the widest for the DAPB compounds, but their closeness to the perfect pentagonal angle of 72° is noteworthy because of the dependence of the orbital degeneracy on the geometry of the metal center.

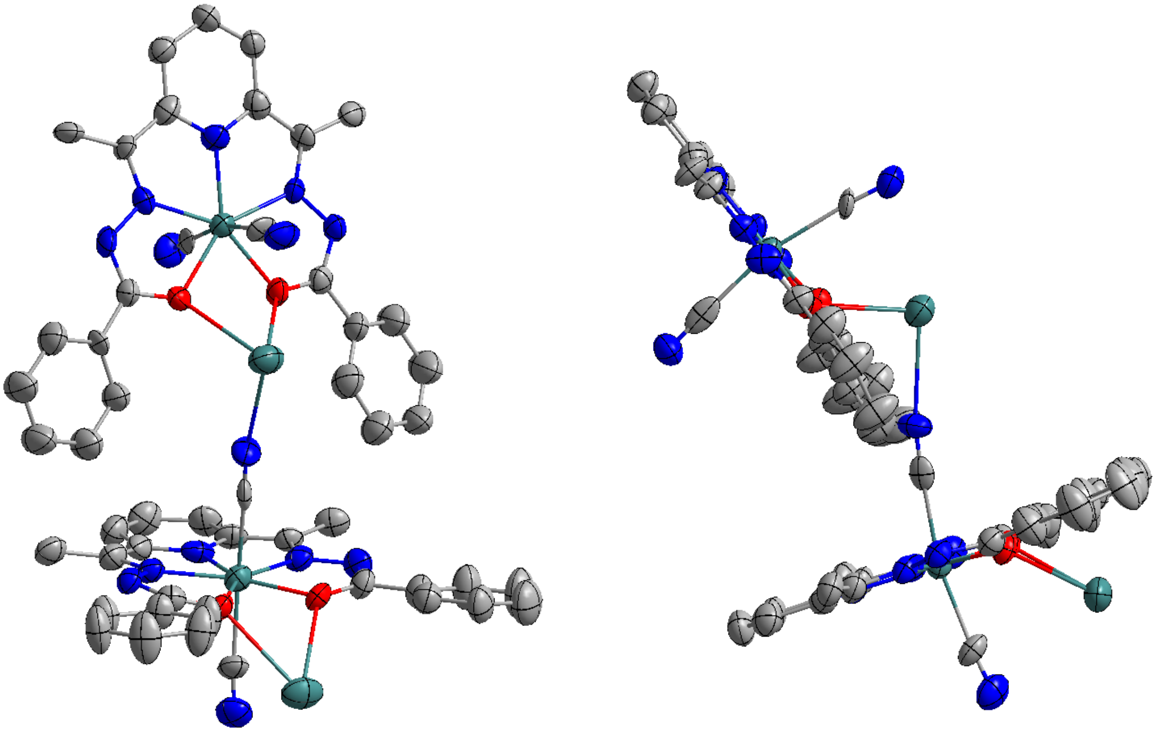

Figure 43. Two views of the two $[Mo^{III}(DAPB)(CN)_2]^-$ fragments in the unit cell of **11**. The ellipsoids are drawn the 50% probability level.

Table 13. Crystal data and structure refinement for **11**.

Identification code	K[Mo^{III}(DAPB)(CN)$_2$]
Empirical formula	$C_{50}H_{42}K_2Mo_2N_{14}O_4$
Formula weight	645.32
Temperature/K	100.01
Crystal system	monoclinic
Space group	$P2_1/n$
a/Å	12.0195(7)
b/Å	23.6383(15)
c/Å	25.3338(16)
α/°	90
β/°	101.438(2)
γ/°	90
Volume/Å^3	7054.9(8)
Z	8
ρ_{calc}g/cm^3	1.215
μ/mm^{-1}	3.495
F(000)	2579.0
Crystal size/mm^3	0.1 × 0.3 × 0.3
Radiation	CuKα (λ = 1.54178)
2Θ range for data collection/°	5.162 to 86.308
Index ranges	$-10 \leq h \leq 10$, $-20 \leq k \leq 19$, $-22 \leq l \leq 21$
Reflections collected	21400
Independent reflections	5101 [R_{int} = 0.0936, R_{sigma} = 0.0586]
Data/restraints/parameters	5101/402/653
Goodness-of-fit[a] on F^2	1.059
Final R indexes [I>=2σ (I)]	$R_1^b = 0.0849$, $wR_2^c = 0.2439$
Final R indexes [all data]	$R_1^b = 0.1024$, $wR_2^c = 0.2596$
Largest diff. peak/hole / e Å^{-3}	2.72/-0.59

[a] Goodness-of-fit = $\{\Sigma [w(Fo^2 - Fc^2)^2]/(n-p)\}^{1/2}$, where n is the number of reflections and p is the total number of parameters refined.

[b] $R = \Sigma || Fo | - | Fc || / \Sigma | Fo |$

[c] $wR = \{\Sigma [w(Fo^2 - Fc^2)^2] / \Sigma w(Fo^2)^2]\}^{1/2}$

Table 14. Comparison of bond angles of Mo with the chelating ligand DAPB. The O-Mo-O angles are wider in each case, but the angles are generally close to the ideal for a pentagonal bipyramid (72°).

Angle	**9**	**10**	**11 (#1)**	**11 (#2)**
N-Mo-N	71.028°	72.069°	70.271°	70.191°
N-Mo-O	71.549°	70.807°	71.478°	72.275°
O-Mo-O	75.289°	75.311°	75.572°	75.2°
O-Mo-N	71.269°	71.37°	72.09°	71.481°
N-Mo-N	70.867°	70.717°	70.927°	70.953°

Cyclic Voltammetry

Cyclic voltammetry was performed on **9** to evaluate its redox potential. Electrochemical measurements were carried out under an inert N_2 atmosphere using dichloromethane that had been dried over molecular sieves, using 0.1 M $[n\text{-}Bu_4N][PF_6]$ as the supporting electrolyte. The setup used an HCH Electrochemical Analyzer model CH 1620A with a glassy carbon working electrode, Pt wire auxiliary electrode, and a Ag/AgCl (3 M KCl(aq)) reference electrode at a 100 mV/s scan rate. The concentration of **9** was ~100 mM. Ferrocene was used as an internal standard and exhibited an $E_{1/2} = 0.44$ V vs Ag/AgCl for the Fc+ /Fc couple under the same experimental conditions. Data shown in Figure 44.

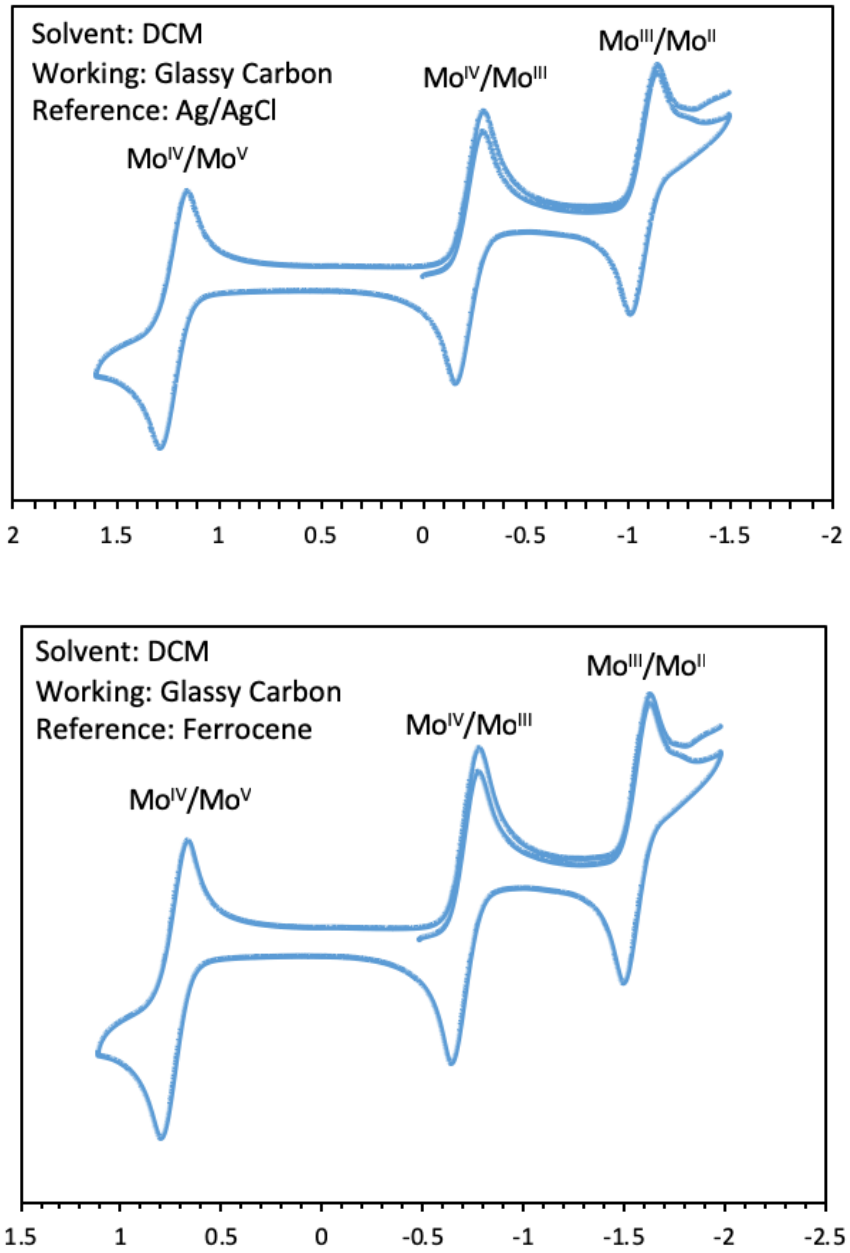

Figure 44. Cyclic voltammograms of **9** in CH_2Cl_2 (DCM).

The cyclic voltammogram exhibits a reversible oxidation at 1.21 V and reversible reduction couples located at $E_{1/2}$ = -0.239 V and $E_{1/2}$ = -1.08 V for **9**. These results indicate that the Mo^{III} analogue is accessible as well as the Mo^{V} and Mo^{II} species.

Magnetic Measurements

Magnetic measurements were performed on a Quantum Design MPMS-XL SQUID magnetometer equipped with a 7 T magnet. A polypropylene bag was used to secure the sample, and the diamagnetic contribution was subtracted from the raw data. Diamagnetic contributions from the sample were accounted for by using Pascal's constants.[74]

Variable temperature static DC magnetic susceptibility measurements were performed on crushed crystals of **7** from 300 to 2 K under an applied field of 1000 Oe (Figure 45). The room temperature χ_mT value of 19.07 $cm^3mol^{-1}K$ is higher than the spin-only value of 14.25 $cm^3mol^{-1}K$ (g_{Mo} = 2.0, S_{Mo} = ½, g_{Ni} = 2.0, S_{Ni} = 1) for the 18-metal center wheel. Calculations on seven-coordinate Mo^{III} centers have revealed that, even in distorted geometries, the g-values are highly anisotropic, with g_z ranging from 3.0 to 3.5 and $g_x = g_y$ ranging from 0.4 – 1.3.**[28]** Calculations (*vide infra*) predict an average g_{iso} value between 2.23-2.24 for the Ni^{II} centers, which also has a substantial effect on χ_mT. The observed room temperature χ_mT value is easily explained when accounting for these highly anisotropic g values (19.10 $cm^3mol^{-1}K$, g_{Mo} = 1.80, S_{Mo} = ½, g_{Ni} = 2.40, S_{Ni} = 1). The χ_mT value increases from 19.07 $cm^3mol^{-1}K$ at 300 K to a maximum of 22.92 $cm^3mol^{-1}K$ at 5 K before dropping precipitously as the temperature is lowered to 2 K. The decrease in χ_mT at very low temperatures is the result of zero-field splitting of the Ni^{II} centers. The increase from 300 to 5 K is likely due to coupling between the Ni^{II} and Mo^{III} centers. In the case where one set of Ni-Mo couplings is ferromagnetic and another set is antiferromagnetic (this is possible when inner-ring six Ni^{II} and all Mo^{III} spins are parallel and the external six Ni^{II} centers are antiparallel), then $S = 3$ would be expected; the room temperature value of χ_mT rules out such a possibility, since χ_mT would be expected to be 6 cm^{3}mol^{-1}K in that case. Both fully antiferromagnetic (S = 9, χ_mT = 45 cm^{3}mol^{-1}K, when all the Ni^{II} centers have a spin-up configuration and all the Mo^{III} have a spin-down configuration) and fully ferromagnetic (S = 15, χ_mT = 120 cm^{3}mol^{-1}K, when all Ni^{II} and Mo^{III} centers have a spin-up configuration) coupling would lead to an increase in χ_mT at low temperatures.

The magnetic susceptibility data for **8** reveal a value of 12.6 cm^{3}mol^{-1}K at 300 K, which is close to the previously reported value of 12.19 cm^{3}mol^{-1}K at 300 K.[92] The data for the magnetic susceptibility of **8** are included in Figure 45 to facilitate direct comparison of the magnetic properties, which clearly exhibit differences in magnetic behavior. The number of metal centers present in **7** precludes the use of complete models to fit the data – attempts based on previously reported methods[105] have not yielded satisfactory fits.

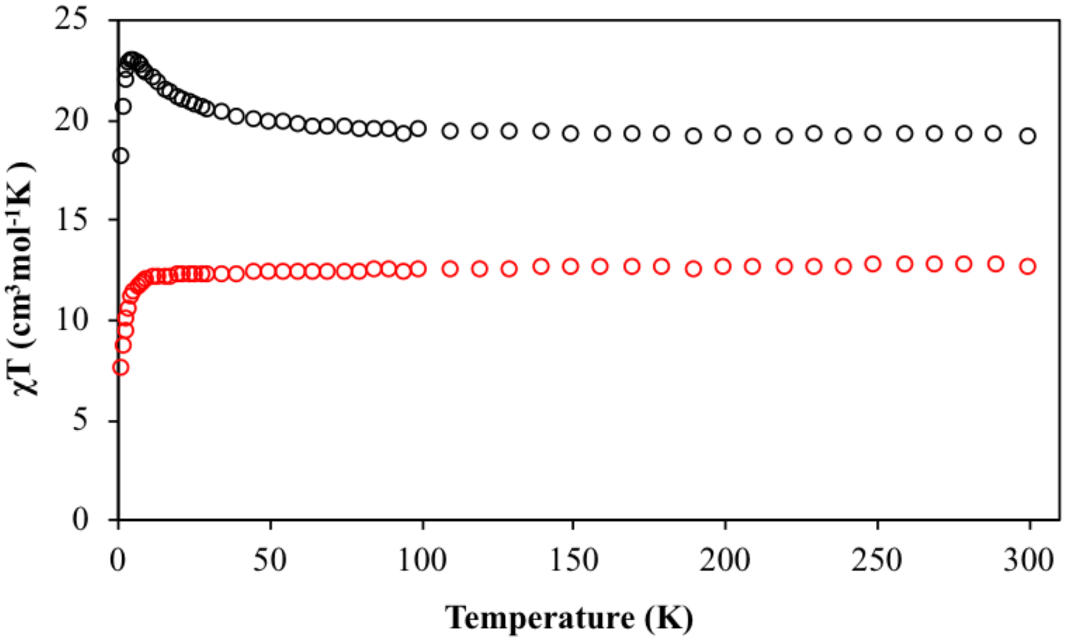

Figure 45. Magnetic susceptibility plots of **7** (black dots) and **8** (red dots).

The magnetization data and reduced magnetization data are instructive in further exploring the magnetic properties of **7**. The 1.8 K magnetization data for **7** (Figure 46) do not saturate up to a field of 7 T, at which field the magnetization is 21.8 μ_B. The spin-only value predicted for an S = 9 ground state (antiferromagnetic coupling between Ni^{II} and Mo^{III}) is 18 μ_B, whereas the value predicted for S = 15 (ferromagnetic coupling) is 30 μ_B. While there is a lack of saturation, the expected value for antiferromagnetic coupling is already exceeded at 7 T, suggesting that the coupling is ferromagnetic. The reduced magnetization data (Figure 47) show that there is anisotropy in the system, even if it is not Ising-type anisotropy that would lead to SMM behavior. The lack of SMM behavior, even with applied DC fields, can be clearly seen in Figure 48.

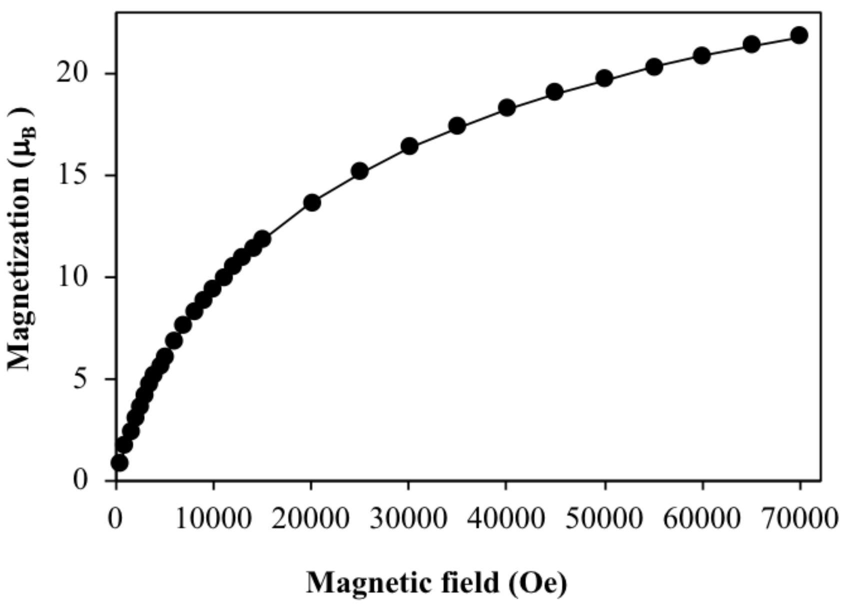

Figure 46. 1.8K magnetization data for **7**. The solid black line is a guide for the eyes.

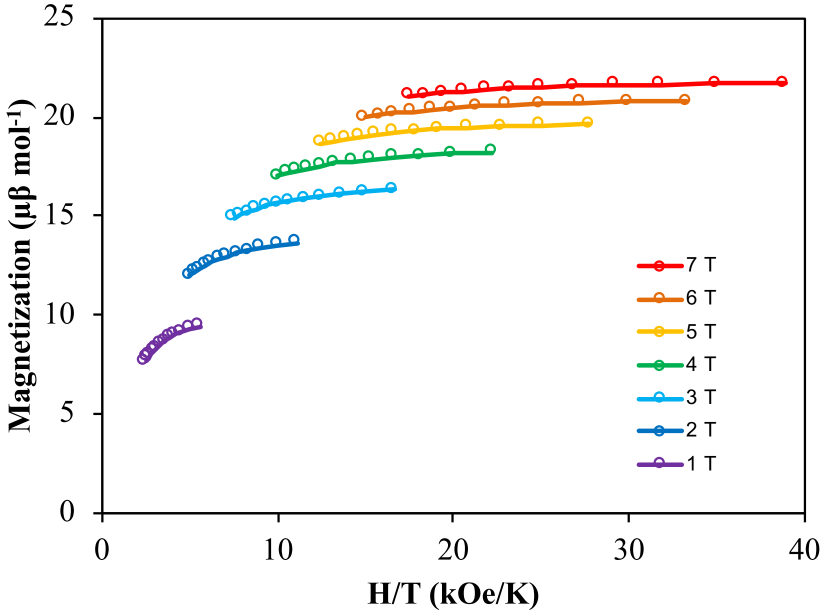

Figure 47. Reduced magnetization data for **7**. Solid lines are a guide for the eye.

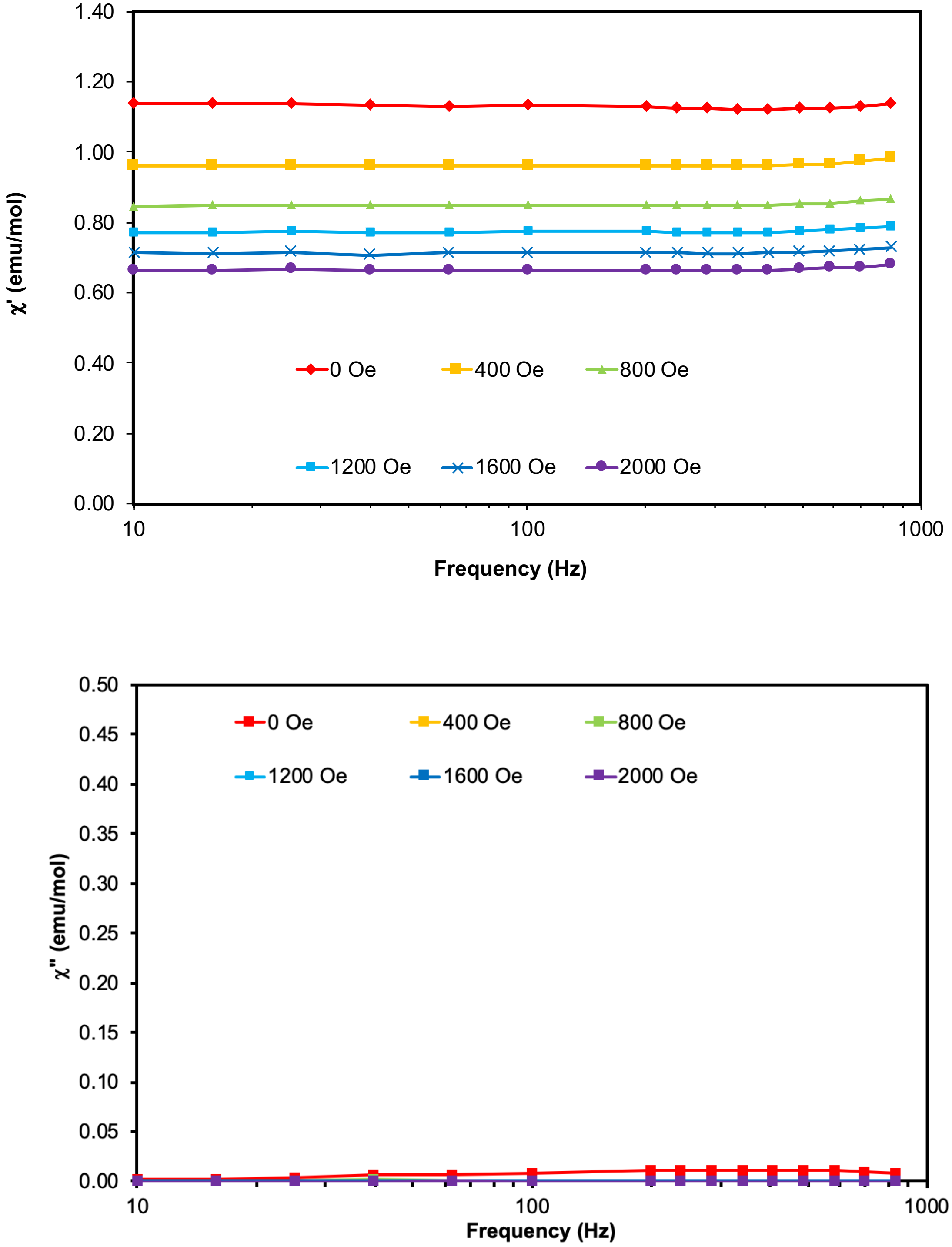

Figure 48. In-phase and out-of-phase susceptibility data for **7**, measured at 2 K with applied static DC fields from 0-2000 Oe.

Infrared Spectroscopy

Infrared spectra were collected on a Nicolet 740 Fourier transform IR spectrometer. Samples were prepared and measured as a Nujol® mulls between KBr plates. The data clearly show a difference between **7** and **8**.

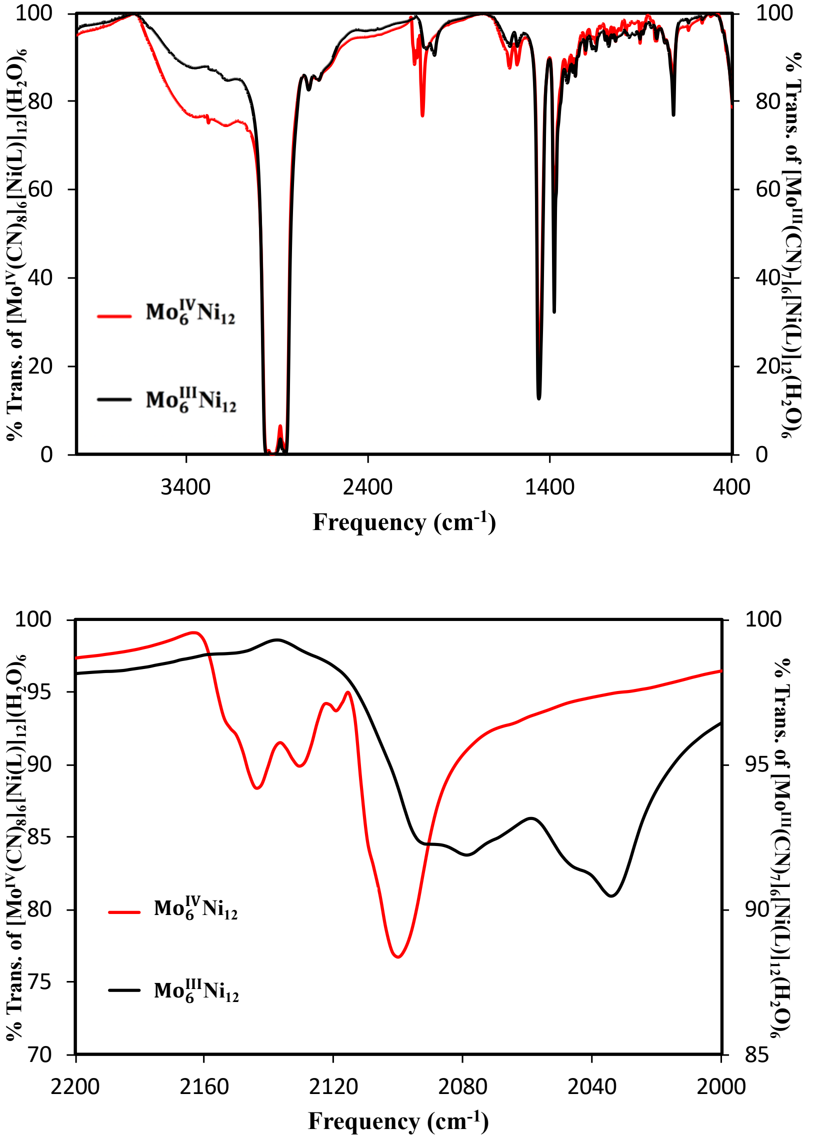

Figure 49. IR spectra for **7** and **8**. Large peaks at 2900, 1460, and 1377 are from the Nujol® used in the mull. The lower spectrum is zoomed in on the cyanide stretching region.

Calculations

DFT calculations, combined with the Broken-Symmetry (BS) approach were carried out to compute the exchange interactions. The calculations described herein were performed by Kuduva R. Vignesh. The B3LYP[106] functionals were employed with Ahlrichs[107-108] triple-ζ basis set for Ni atoms, a relativistic effective-core potential (ECP) LANL08(f) basis set [109] for Mo atoms and 6-31g* basis set for rest of the atoms as implemented in the Gaussian 09[110] suite of programs to calculate the energies of the spin states as given in Table S5. The J values were computed from the energy differences between the high spin (E_{HS}) state calculated using single determinant wave functions, and the low spin (E_{BS}) state determined using the Broken Symmetry (BS) approach developed by Noodleman.[111] The BS approach has a proven record of yielding good numerical estimates of J constants for a variety of complexes,[112-113] such as dinuclear[114-116], and especially, 4d/5d metal complexes[117] and polynuclear complexes.[112,118-119] The following Hamiltonian is used to estimate the isotropic exchange interaction (J).

$$(3) \quad \hat{H} = -2J(S_{Mo}S_{Ni})$$

In the case of a two spin system and using the spin Hamiltonian $\mathbf{\hat{H} = -2\boldsymbol{J_{ij}}S_iS_j}$, the energy difference between the high spin and low spin state is:

$$(4) \quad E_{HS} - E_{BS}/2S_iS_j = -2J_{ij}$$

Considerations related to the self-interaction error in commonly used exchange functional, non-dynamic pair correlation effects, and the application of spin projection techniques to

DFT calculations led to the following equation to describe the energy difference: [112-113,114-116]

$$(5)\quad E_{HS} - E_{BS}/(2S_iS_j + S_j) = -2J_{ij}, \text{ where } S_i > S_j.$$

Application of this formalism to half of the $Mo^{III}_6Ni^{II}_{12}$ complex that consists of six Ni^{II} ions and three Mo^{III} with three J_1 interactions (between the inner ring Ni^{II} ions and Mo^{III} ions) and three J_2 interactions (between the outer Ni^{II} ions and Mo^{III} ions), leads to the following expressions for the differences between the energies for the nine spin states calculated by DFT methods:

$$(6)\quad E_{BS1} - E_{HS} = 2J\,(2 * 1 * ½ + ½) = 3J_1$$

For three possible J_1 interactions the expression becomes,

$$(7)\quad E_{BS1} - E_{HS} = 9J_1$$

Similarly, for three possible J_2 interactions the expression becomes,

$$(8)\quad E_{BS2} - E_{HS} = 9J_2$$

$$(9)\quad J_1 = 1/9\ (184.47\ \text{cm}^{-1}) = +20\ \text{cm}^{-1}$$

$$(10)\quad J_2 = 1/9\ (74.36\ \text{cm}^{-1}) = +8.26\ \text{cm}^{-1}$$

Ab initio calculations were performed to compute the *g* value and the zero-field splitting (D) of the Ni^{II} ions and g value for the Mo^{III} ions in **1** using ORCA 3.0 suite of programs.[120] The BP86 functional was employed along with a scalar relativistic ZORA Hamiltonian and relativistic ZORA type of def2-TZVP basis set on the metal ions and on first coordination sphere, and def2-SVP for the rest of the atoms. The RI approximation with secondary TZV/*J* Columbic fitting basis sets were used along with increased integration grids (Grid 5 in ORCA convention). The tight SCF convergence was used throughout the calculations ($1x10^{-8}$ Eh). The SOC contributions in the *ab initio* frame work were obtained using second-order perturbation theory as well as employing the effective Hamiltonian approach which enables calculations of all matrix elements to be made of the anisotropic spin Hamiltonian from the *ab initio* energies and wave functions numerically. Here the state average-CASSCF (Complete Active Space Self-Consistent Field) method has been employed to compute the zero-field splitting. The active space comprises eight active electrons in five active d-orbitals (d^8 system; CAS (8,5)) for Ni^{II} ion. With this active space, 1 10 triplet and 15 singlet states for the Ni^{II} ion have been computed in the configuration interaction procedure.

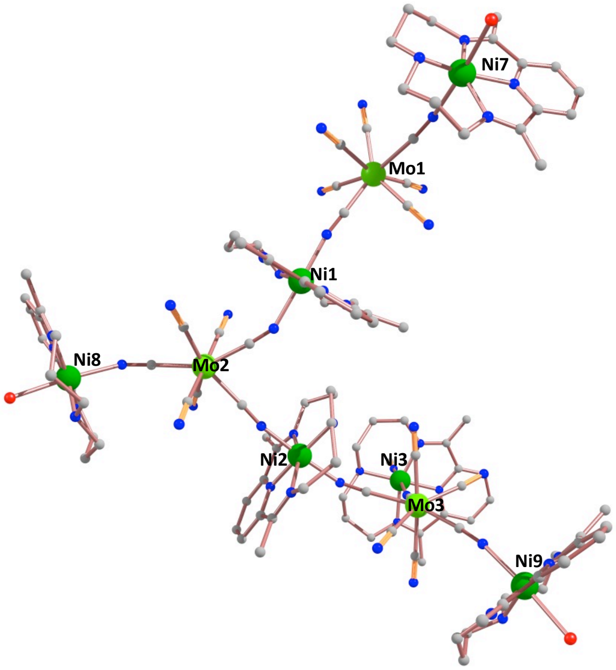

Figure 50. One-half of the **7** complex, depicted above, was used for DFT calculations to compute the exchange interactions.

Table 15. Different spin configurations employed for extracting *J* values and its corresponding energies from DFT calcualtions in **7**. Black arrows denote "spin-up" and red arrows denote "spin-down."

	Mo1	**Mo2**	**Mo3**	**Ni1**	**Ni2**	**Ni3**	**Ni7**	**Ni8**	**Ni9**	**Es (in Hartree)**	$\Delta E = E_{BS} - E_{HS}$ (cm^{-1})
HS	↑	↑	↑	↑	↑	↑	↑	↑	↑	-16346.72018710	0
BS1	↑	↑	↑	↓	↓	↓	↑	↑	↑	-16346.71934660	184.47
BS2	↑	↑	↑	↑	↑	↑	↓	↓	↓	-16346.71984830	74.36

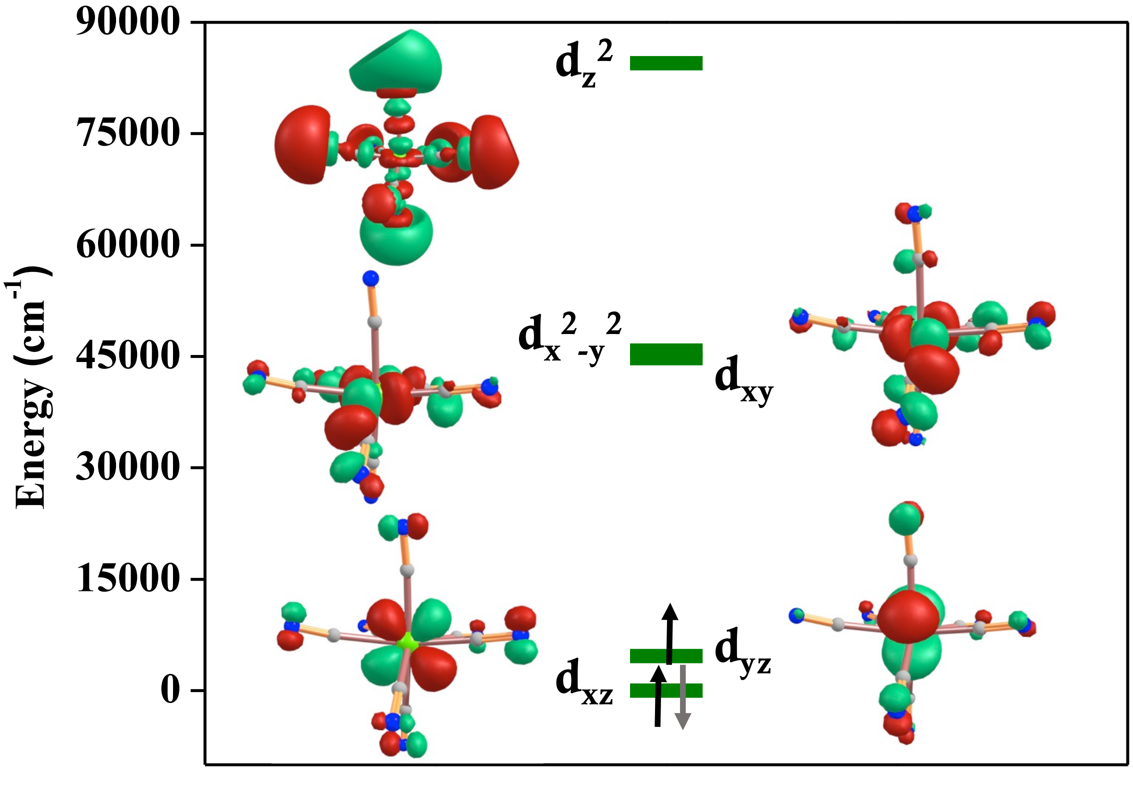

Figure 51. CASSCF computed d-orbital ordering for Mo^{III} ions in **7**.

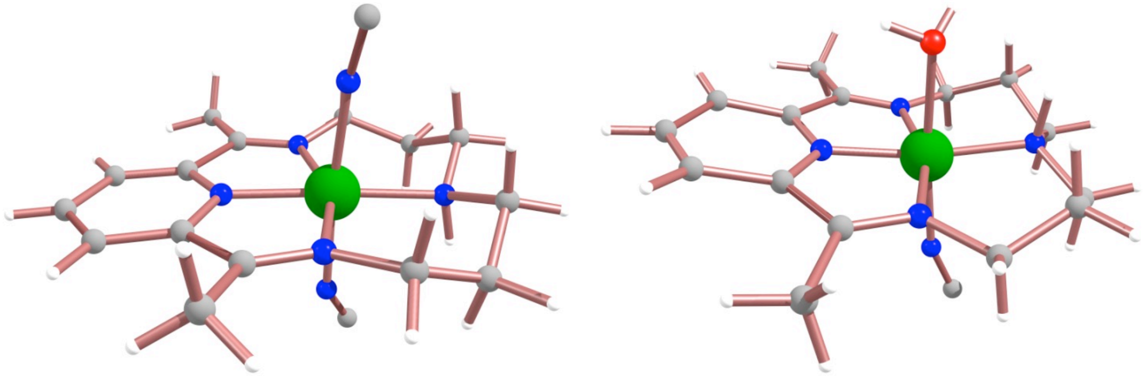

Figure 52. The two Ni centers {Ni(CN)$_2$} (left) and {Ni(CN)(H$_2$O)} (right) used for CASSCF calculations.

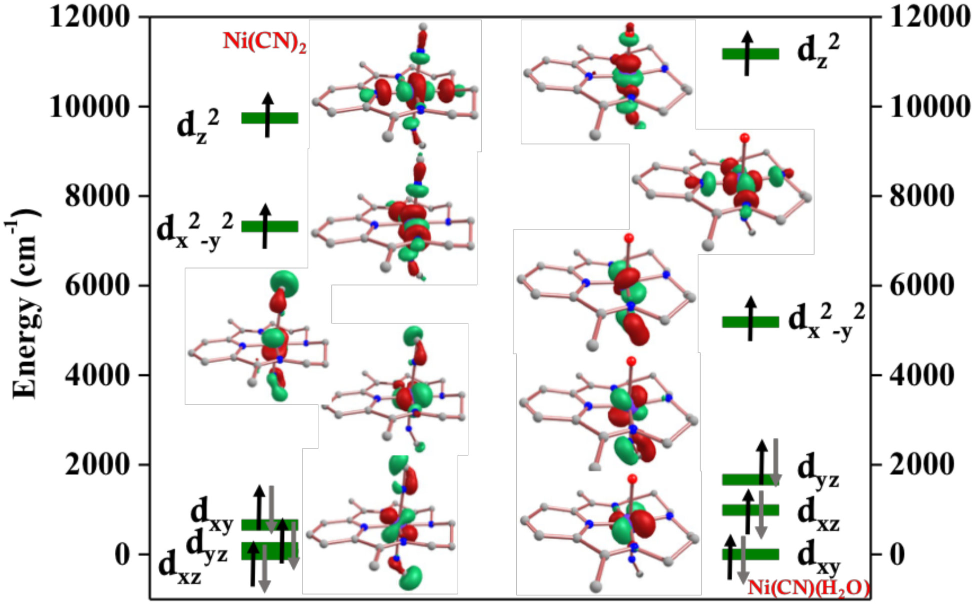

Figure 53. CASSCF-computed d-orbital ordering for Ni^{II} ions in **7**.

Table 16. Values of g, *D* (in cm^{-1}) and *E/D* values for both Ni and Mo centers in **7** computed from *ab initio* CASSCF calculations.

Complex	*calculated*		
	D	*E/D*	g_{iso} (g_x, g_y and g_z)
{Ni(CN)$_2$}	-6.2	0.13	2.23 (2.21, 2.22, 2.26)
{Ni(CN)(H$_2$O)}	+11.2	0.23	2.24 (2.18, 2.25, 2.29)
{Mo(CN)$_7$}	--	--	1.76 (1.03, 1.05, 3.19)

Table 17. CASSCF computed energies (cm^{-1}) and contributions to the *D* value from the first four excited states for Ni^{II} ions in complex **7**.

Ni centers	Excited state	Energy	*D* Contribution
{Ni(CN)$_2$}	First	8751.7	-48.3
	Second	10199.1	20.7
	Third	10556.6	19.6
	Fourth	16398.0	0.06
{Ni(CN)(H$_2$O)}	First	7830.4	26.7
	Second	8748.8	23.3
	Third	11663.6	-35.6
	Fourth	15349.5	-0.5

These calculations provide key evidence that corroborates the magnetic data; the results predict that both the J_1 and J_2 interactions are ferromagnetic in nature with the values of +20.5 and +8.3 cm^{-1}, respectively (Table 15). The ferromagnetic interaction values indicate that all Mo^{III} and Ni^{II} ions have spin-up configurations, leading to a ground state of S = 15. These calculated ferromagnetic interactions are consistent with reported exchange constants values between 4d/5d and Ni^{II} ions.[117,121]

Ab initio CASSCF calculations were performed to compute the zero-field splitting (D) of Ni ions and g parameters for both Ni and Mo ions in **7**. Calculations suggest a g value of 1.76 (g_x =1.03, g_y= 1.05 and g_z = 3.19) for $\{Mo^{III}CN_7\}$ center which is in close agreement with the reported values[28] and rationalizes the expected room temperature $\chi_m T$ value when considering anisotropic Ni centers (Figure 51 and Table 17). Calculations predict a negative D value (-6.2 cm^{-1}) and g = 2.23 for the inner ring Ni^{II} ions with two –CN groups in axial positions ($\{Ni(CN)_2\}$), and a positive D value (+11.2 cm^{-1}) and g = 2.24 for the external Ni^{II} ions with a H_2O molecule and a –CN group in their axial positions ($\{Ni(CN)(H_2O)\}$) (Figure 52 and Table 16). The computed crystal field splitting of the d orbitals for Ni^{II} ions are depicted in Figure 53. Based on the orbital splitting in the $\{Ni(CN)_2\}$ centers, the first excitation involves orbitals with the same $|\pm m_l|$ values (d_{xy} to $d_{x^2-y^2}$) resulting in a negative D value as expected. In contrast, for the $\{Ni(CN)(H_2O)\}$ centers, the first excitation occurs between the d_{xz} and d_{yz} orbitals (different $|\pm m_l|$ values) leading to a positive D value. In both cases, the major contribution to the D value arises from the triplet excited states (Table 17). The energy gaps between the ground and the first excited triplet states are relatively large, leading to either a small negative or positive D value.

Conclusions and Future Studies

This work demonstrates that syntheses of octacyanocyanometallate containing compounds can be extended to the heptacyano derivatives. By using $[Mo^{III}(CN)_7]^{4-}$ in this synthesis instead of $[Mo^{IV}(CN)_8]^{4-}$, an analogue was isolated that exhibits coupling between the Mo and Ni centers. The magnetic data and the calculations, taken together, provide strong evidence that the coupling is ferromagnetic in nature. This strategy can be useful in future work as a method to reliably obtain new molecules that contain $[Mo^{III}(CN)_7]^{4-}$. Specifically, molcules of Cu and Mo, which are previously known with $[Mo^{IV}(CN)_8]^{4-}$, may provide interesting photomagnetic properties.[122-126]

Additionally, the newly reported compounds of Mo and the ligand DAPB provide a new route to pentagonal bipyramidal structures that contain Mo^{III}. While previous examples of SMMs that exhibit anisotropic exchange were limited to Mn^{II}, this new starting material may accelerate progress towards the realization of trinuclear compounds with other metal centers; the restricted geometry of the Mo^{III} center highly encourages the formation of Ising-type anisotropic exchange. The rich electrochemistry for this molecule is another excellent reason to pursue work with MoDAPB fragments – changing the oxidation state could lead to changes in other physical properties, including magnetism. A series which was able to probe many similar MoDAPB molecules may lead to interesting insights into exchange interactions and other phenomena. By systematically varying the identity of the capping metal groups and their geometry, new insights will be gained into the requisite parameters to improve polynuclear transition metal magnets.

CHAPTER IV

COMPOUNDS CONTAINING ORBITALLY DEGENERATE RHENIUM(II)

Background

Heavy metal atoms, such as 5d transition metals, are important in the field of molecular magnetism due to the influence of more diffuse orbitals and increased spin-orbit coupling parameters. The increased spin-orbit coupling effects directly influence the anisotropy in the compounds whereas more diffuse orbitals lead to increased coupling. Both of these characteristics are desirable qualities for molecular magnets and could help to increase the operating temperature of SMMs. As the first example of a 5d-metal containing SMM, the molecule $[\{MnCl\}_4\{Re(triphos)(CN)_3\}_4]$, published by the Dunbar group in 2004,[36] underscores the benefits of the incorporation of 5d metal ions in magnetic compounds. Theoretical analysis of this molecule led to the conclusion that anisotropic exchange was responsible for the SMM behavior of the molecule.[29] In spite of the observed SMM properties, the analysis revealed that the shape of the compound causes partial cancellation of the Ising-type anisotropy in the molecule. The anisotropy in the compound originates from the 3-fold axis in the $[(triphos)Re^{II}(CN)_3]^-$ moiety and the orientation of these moieties in $[\{MnCl\}_4\{Re(triphos)(CN)_3\}_4]$ results in less anisotropy than if the 3-fold axes were arranged coaxially (see Figure 11).

As a result of that partial cancellation, a major goal of this work was to isolate a compound of $[(triphos)Re^{II}(CN)_3]^-$ with a geometry that is more conducive to the development of Ising-type anisotropy. In the case of $[\{MnCl\}_4\{Re(triphos)(CN)_3\}_4]$, there is no organic ligand on the Mn^{II} center to restrict the formation of an octanuclear complex. The introduction of a ligand that blocks some sites on the 3d metal center is expected to lead to the formation of compounds with different shapes than a distorted cube. In this vein, tmphen (3,4,7,8-tetramethyl-1,10-phenanthroline) is an attractive choice due to its steric bulk and propensity to facilitate crystallization. Pentanuclear trigonal bipyramidal compounds that take advantage of this ligand were previously reported by the Dunbar group,[78,127-128] which is a very promising geometry for compounds of $[(triphos)Re^{II}(CN)_3]^-$ because of the manner in which the threefold axes on both of the $[(triphos)Re^{II}(CN)_3]^-$ moieties would align. It has been shown that the bulk of the triphos ligand would not hinder the formation of a pentanuclear structure of this type, as the previously synthesized compound $(Et_4N)_2[((triphos)Re^{II}(CN)_3)_2(Ln(NO_3)_3)_3]\cdot 4MeCN$ adopts this arrangement.[129] Despite the geometry of these structures, the very weak coupling to the lanthanide centers prohibits any Ising-type anisotropy from having a significant impact on the magnetism. It was hypothesized that replacing the lanthanide ions with 3d transition metal ions in a similar architecture could generate Ising-type anisotropy through the mechanism of anisotropic exchange.

A second key design criterion involves the electronic structure of the 3d metal. Despite forming cubes with the formula $[\{MCl\}_4\{Re(triphos)(CN)_3\}_4]$ where M = Mn, Fe, Co, Ni, or Zn, only the Mn analog exhibits SMM behavior. This may be partially due to the introduction of a second source of anisotropy; other groups have reported that having multiple sources of anisotropy in polynuclear compounds sometimes results in diminished SMM behavior, as is the case for the series of compounds

$[L_{NNN}CoLnCoL_{NNN}]NO_3$ (L = N,N′,N″-tris(2-hydroxy-3-methoxy- benzili- dene)-2-(aminomethyl)-2-methyl-1,3-propanediamine; Ln = Gd, Tb, Dy) (Figure 6).[26-27] Notably, all SMMs that exhibit Ising-type anisotropic exchange couple an orbitally degenerate metal center with the isotropic 3d metal Mn^{II}.[36-39] Another interesting choice that has yet to be explored is V^{II}. The more diffuse orbitals are expected to lead to stronger coupling, which may also enhance the barrier since the barrier height is proportional to the strength of the coupling in anisotropically exchange-coupled systems. Therefore, V^{II} was used for the reactions with $[(triphos)Re^{II}(CN)_3]^-$ in this chapter.

Three new compounds of $[(triphos)Re^{II}(CN)_3]^-$ are reported herein, one of which successfully meets the criteria of lining up the threefold axes of the $[(triphos)Re^{II}(CN)_3]^-$ moieties. Two of these compounds, $[\{V^{II}(tmphen)_2\}_2\{Re(CN)_3(triphos)\}_2](CF_3SO_3)_2$ (**12**) and the decomposition product $[\{V^{II}(tren)\}(\mu\text{-}CN)Re(triphos)]_2(\mu\text{-}O)$ (**13**) (tren = triethylamine) demonstrate that the presence of coupling and an orbitally degenerate Re^{II} center are not sufficient to guarantee Ising-type magnetic exchange. The third molecule $[V^{II}(tmphen)Cl_2]_3[Re(CN)_3(triphos)]_2\cdot 2MeCN$ (**14**) is an excellent example to follow for future studies on molecules with the proper geometry to introduce Ising-type anisotropic exchange interactions.

Experimental Details

Synthesis

Syntheses were carried out under air free conditions using a nitrogen-filled glove box or Schlenk line outfitted with argon gas. The solvents were deoxygenated by sparging with argon gas. Diethyl ether was purified using an MBRAUN purification system. $[V^{II}(H_2O)_6](CF_3SO_3)_2$ and $(NEt_4)[(triphos)Re^{II}(CN)_3]$ were prepared by literature methods;[34,130] all other chemicals were purchased from commercial sources and used without further purification unless otherwise indicated.

$[\{V^{II}(tmphen)_2\}_2\{Re(CN)_3(triphos)\}_2](CF_3SO_3)_2$ (12)

$[V^{II}(H_2O)_6](CF_3SO_3)_2$ (34 mg, 0.075 mmol) of and tmphen (35 mg , 0.15 mmol) were dissolved in 2 mL of H_2O, 2 mL of MeOH, and 1 mL of MeCN. $(NEt_4)[(triphos)Re^{II}(CN)_3]$ (50 mg, 0.05 mmol) was also dissolved in 2 mL of H_2O, 2 mL of MeOH, and 1 mL of MeCN. The solution of $(NEt_4)[(triphos)Re^{II}(CN)_3]$ was added dropwise to the solution of $[V^{II}(H_2O)_6](CF_3SO_3)_2$ and tmphen which led to a cloudy green solution. After standing overnight at room temperature, dark green, X-ray quality crystals were isolated, 12 mg, 7.7% yield. Attempts to recover more product via Et_2O diffusion were unsuccessful.

$[\{V^{II}(tren)\}(\mu\text{-}CN)Re(triphos)]_2(\mu\text{-}O)$ (13)

$[V^{II}(H_2O)_6](CF_3SO_3)_2$ (23 mg, 0.05 mmol) and tren (8 g, 0.05 mmol) were dissolved in 2 mL of MeCN and 1 mL of MeOH and a separate sample of $(NEt_4)[(triphos)Re^{II}(CN)_3]$ (34 mg, 0.034 mmol) was dissolved in 2 mL of MeCN and 1 mL of MeOH. The $(NEt_4)[(triphos)Re^{II}(CN)_3]$ solution was added dropwise to the solution of $[V^{II}(H_2O)_6](CF_3SO_3)_2$ and tren, which resulted in a slightly cloudy orange solution. After standing overnight at room temperature, X-ray quality dark orange crystals were isolated; 8 mg, 10% yield. Attempts to recover more product via Et_2O diffusion were unsuccessful.

$[V^{II}(tmphen)Cl_2]_3[Re(CN)_3(triphos)]_2\cdot 2MeCN$ (14)

$[V^{II}(H_2O)_6](CF_3SO_3)_2$ (23 mg, 0.05 mmol) and tmphen (24 mg, 0.1 mmol) were dissolved in 4 mL acetonitrile and added dropwise to a solution of $(NEt_4)[(triphos)Re^{II}(CN)_3]$ (50 mg, 0.05 mmol) in 4 mL of acetonitrile. The solution turned a dark blue color, and, after standing overnight, a small amount of Et_2O was added. After 2 hours, a small crop of X-ray quality crystals was harvested from the solution. More Et_2O was diffused into the solution in an attempt to recover more product, but no more crystals were isolated.

Crystallography

Single crystals were selected under Paratone® oil with a MiTGen microloop or a glass fiber. Reflection data for **12** were collected under a stream of N_2 at 100K using beamline 15-AD-B at the Advanced Photon Source at Argonne National Laboratory. Reflection data for **13** and **14** were collected on a Bruker D8-QUEST diffractometer equipped with a IμS Mo microsource ($\lambda = 0.71073$ Å) under a stream of N_2 gas at 100 K. The frames were integrated and a semi-empirical absorption correction was applied using SADABS[68] within the software package included in the APEX3 software suite.[69] The structure was solved using SHELXT[70] and refined using SHELXL;[71] OLEX2 was used as an interface for the solution and refinement.[72] Small Q-peaks in the structure that were consistent with the behavior of disordered solvent were removed using the SQUEEZE routine of the PLATON software package.[73] Hydrogen atoms were placed in calculated positions.

$[\{V^{II}(tmphen)_2\}_2\{Re(CN)_3(triphos)\}_2](CF_3SO_3)_2$ (12)

Compound **12** crystallizes in the space group $P\bar{1}$. The refinement required modeling of a disorder of the triflate anion, the phenyl rings that are part of the triphos ligand, and one tmphen ligand. No additional restraints or constraints were used. The two vanadium and two rhenium units form the corners of a square-like core, where the edges are the CN^- ligands connected to one rhenium and one vanadium atom each. The metal centers adopt a distorted octahedral geometry with the Re and V metal ions being capped by a triphos moiety and two tmphen ligands respectively. Each rhenium unit is bound to the $V(tmphen)_2$ moieties through two of the three cyanide ligands with one terminal cyanide ligand. One square occupies into the unit cell and is accompanied by two triflate anions, so the square must have a +2 charge. In this case, the metal centers can be assigned as Re^{II} and V^{II}. The square sits on an inversion center so the asymmetric unit only contains half of the molecule. The Re-C bond lengths in the structure are 2.001(19) Å, 2.02(3) Å, and 1.996(17) Å. The V-N bond lengths to the cyanide ligands are 1.981(14) Å and 1.986(17) Å. The square has angles at the corners of 86.374° for C-Re-C and 99.800° for N-V-N.

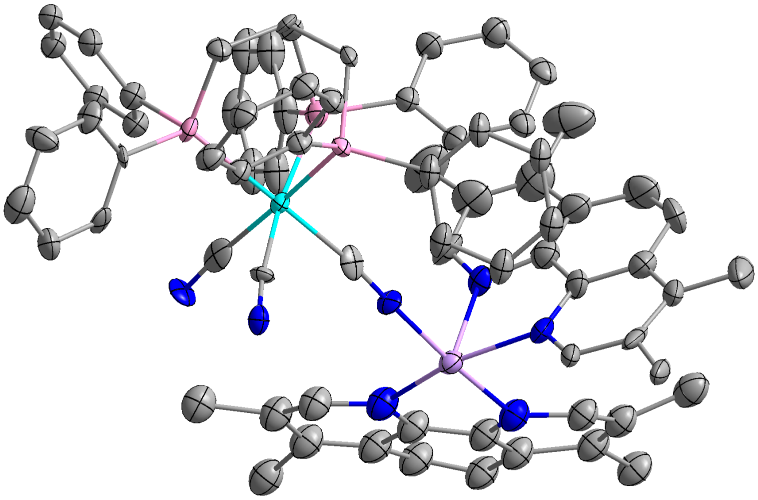

Figure 54. Plot of the asymmetric unit in **12**. Ellipses are drawn at the 50% probability level.

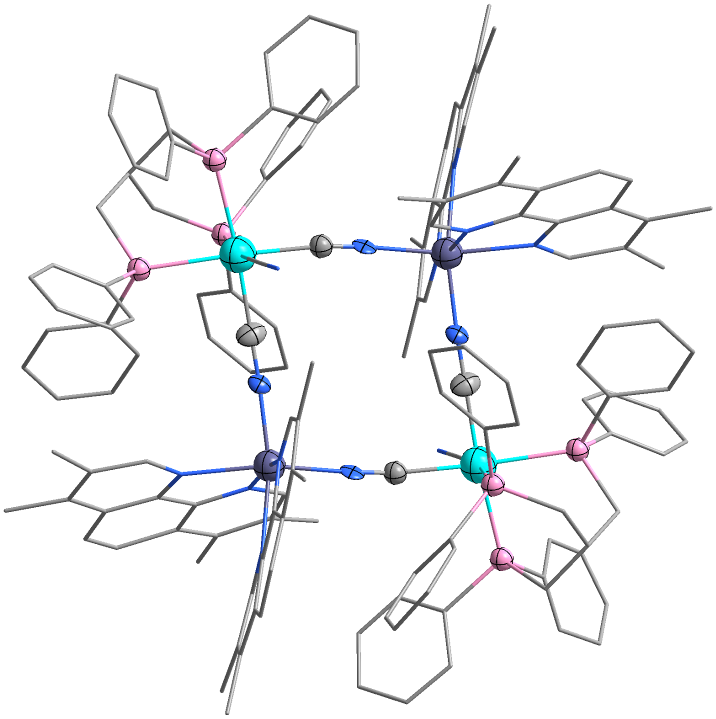

Figure 55. Full molecule of **12**. Ligands are drawn in a wireframe mode to emphasize the structure of the cyanide-bridged core.

Table 18. Crystal data and structure refinement for **12**.

Identification code	Re2V2
Empirical formula	$C_{77}H_{71}F_3N_7O_3P_3ReSV$
Formula weight	1561.51
Temperature/K	100
Crystal system	triclinic
Space group	P-1
a/Å	15.474(5)
b/Å	15.617(5)
c/Å	15.993(5)
α/°	73.460(4)
β/°	85.974(4)
γ/°	78.444(4)
Volume/Å^3	3629(2)
Z	2
ρ_{calc}g/cm^3	1.429
μ/mm^{-1}	1.950
F(000)	1584.0
Crystal size/mm^3	.05 × .05 × .03
Radiation	Synchrotron (λ = 0.41328)
2Θ range for data collection/°	3.264 to 51.622
Index ranges	$-18 \leq h \leq 18$, $-18 \leq k \leq 18$, $0 \leq l \leq 19$
Reflections collected	12498
Independent reflections	12498 [R_{int} = 0.0140, R_{sigma} = 0.0827]
Data/restraints/parameters	12498/1929/1301
Goodness-of-fit^a on F^2	1.144
Final R indexes [I>=2σ (I)]	R_1^b = 0.1131, wR_2^c = 0.3070
Final R indexes [all data]	R_1^b = 0.1359, wR_2^c = 0.3215
Largest diff. peak/hole / e Å^{-3}	4.44/-2.71

[a] Goodness-of-fit = $\{\Sigma [w(Fo^2 - Fc^2)^2]/(n-p)\}^{1/2}$, where n is the number of reflections and p is the total number of parameters refined.

[b] $R = \Sigma || Fo | - | Fc || / \Sigma | Fo |$

[c] $wR = \{\Sigma [w(Fo^2 - Fc^2)^2] / \Sigma w(Fo^2)^2]\}^{1/2}$

[{V^{II}(tren)}(μ-CN)Re(triphos)]$_2$(μ-O) (13)

Crystals of **13** adopt the space group $P2_1/n$. The asymmetric unit contains one-half of the molecule of one [(triphos)$Re^{II}(CN)_3]^-$ moiety and one $[V^{II}(tren)]^{2+}$ moiety. There is an O^{2-} bridge between the two V^{II} centers in the molecule which was assigned based on the charges of the other atoms in the structure. No outer-sphere ions were identified in the structure, so the molecule is assumed to be neutrally charged. The phenyl rings in the triphos ligands are somewhat disordered and were successfully modeled over two positions. The V-O bond length is 1.760(2) Å, which is consistent with other examples of linear V-O-V bonds with oxide.[131-132] V-OH-V examples are typically bent and have distances close to 2.0 Å, while bridging H_2O is also bent and typically has an even larger distance of 2.4 or 2.5 Å.[133-136] The Re centers are six-coordinate with Re-C bond distances of 2.034(17) Å, 2.067(15) Å, and 2.034(15) Å. The V^{II} ions are also six-coordinate with a V-N_{CN} bond distance of 2.068(12) Å. The V-N_{tren} bond distances are 2.151(11) Å, 2.208(11) Å, 2.162(11) Å, and 2.160(11) Å, with the longest bond being to the central N atom of tren. The angles around V are near 90°, with the N-V-O angles being the largest (93.225° - 102.671°) and the N-V-N angles being the smallest (79.887° - 91.033°).

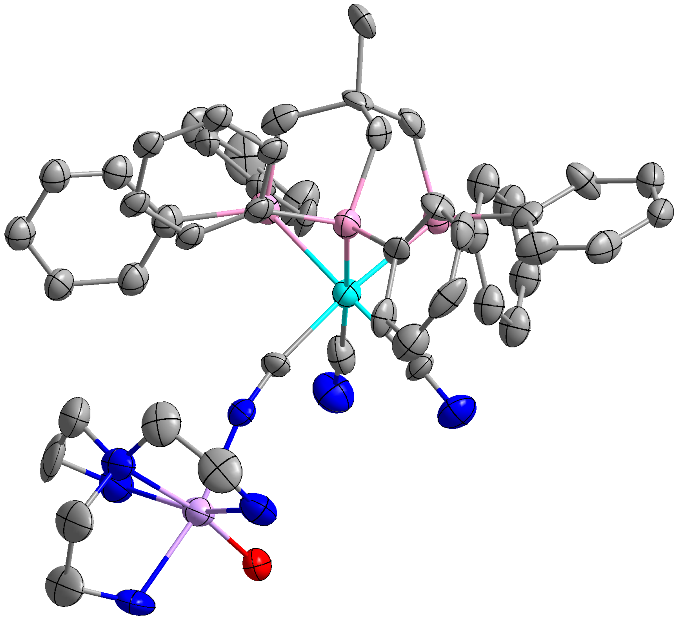

Figure 56. Plot of the asymmetric unit in **13**. Ellipses are drawn at the 50% probability level.

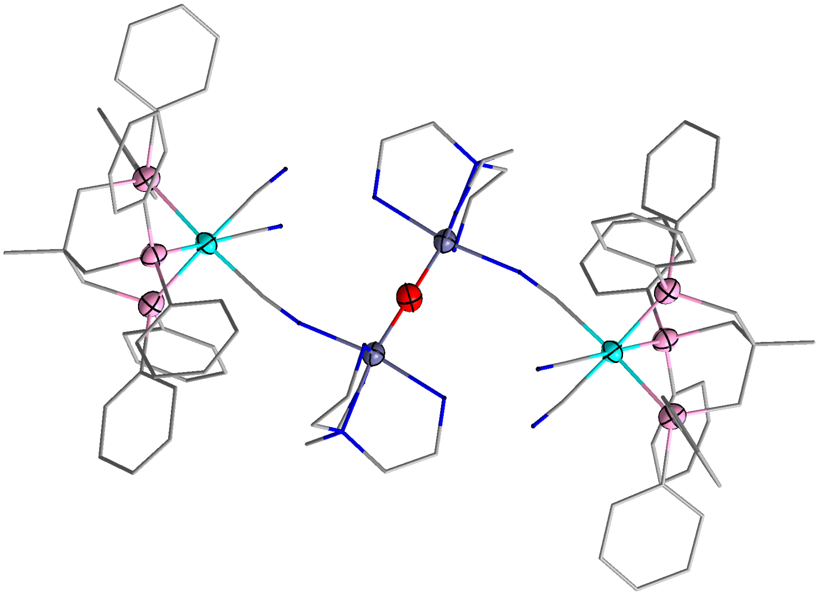

Figure 57. Full molecule of **13**. Ligands are drawn in a wireframe mode to emphasize the structure of the cyanide and oxide-bridged core.

Table 19. Crystal data and structure refinement for **13**.

Identification code	Re2V2O
Empirical formula	$C_{50}H_{59}N_{7}O_{0.5}P_{3}ReV$
Formula weight	346.68
Temperature/K	110
Crystal system	monoclinic
Space group	$P2_{1}/n$
a/Å	12.291(4)
b/Å	31.795(10)
c/Å	14.107(4)
α/°	90
β/°	94.934(8)
γ/°	90
Volume/Å^{3}	5493(3)
Z	33
ρ_{calc}g/cm^{3}	3.459
μ/mm^{-1}	20.022
F(000)	5024.0
Crystal size/mm^{3}	.2 × .1 × .2
Radiation	MoKα (λ = 0.71073)
2Θ range for data collection/°	2.562 to 38.764
Index ranges	$-11 \leq h \leq 11$, $-29 \leq k \leq 29$, $-13 \leq l \leq 13$
Reflections collected	30230
Independent reflections	4654 [R_{int} = 0.1119, R_{sigma} = 0.0789]
Data/restraints/parameters	4654/522/657
Goodness-of-fit[a] on F^{2}	1.040
Final R indexes [I>=2σ (I)]	R_{1}^{b} = 0.0471, wR_{2}^{c} = 0.1199
Final R indexes [all data]	R_{1}^{b} = 0.0722, wR_{2}^{c} = 0.1363
Largest diff. peak/hole / e Å^{-3}	0.52/-0.66

[a] Goodness-of-fit = $\{\Sigma [w(Fo^{2} - Fc^{2})^{2}]/(n-p)\}^{1/2}$, where n is the number of reflections and p is the total number of parameters refined.

[b] $R = \Sigma \| Fo | - | Fc \| / \Sigma | Fo |$

[c] $wR = \{\Sigma [w(Fo^{2} - Fc^{2})^{2}] / \Sigma w(Fo^{2})^{2}]\}^{1/2}$

Na[V^{II}(tmphen)Cl$_2$]$_3$[Re(CN)$_3$(triphos)]$_2$·2MeCN (14)

Compound **14** crystallizes in the space group $P\bar{1}$. The general shape is similar to previous examples of trigonal bipyramidal molecules – the three V units sit reside at the vertices of a triangular plane, which is capped by the two Re atoms. Interestingly, no sources of Na$^+$ or Cl$^-$ were added to the reaction; however, NaCl is a possible contaminant from the metathesis of NaCN and (Et$_4$N)Cl, which is used to make the (Et$_4$N)CN. (Et$_4$N)CN is the cyanide source used to synthesize (Et$_4$N)[(triphos)Re^{II}(CN)$_3$]. The Cl$^-$ ions are the only negatively charged species that is close to the right size for the ligands on V^{II} in **14**. The Na$^+$ was assigned by observing electron density in the center of the structure which fits with Na$^+$. Mg^{2+} is also a valid assignment, but is less likely to be a contaminant. This positively charged ion has close contacts with the CN$^-$ ligands in the structure, so it is not logical to assign it as a negatively charged ion. Further work is necessary to confirm these assignments, preferably by synthesizing this molecule intentionally in a higher yield and measuring the magnetic properties.

The bridging cyanide ligands occupy the edges of the resulting trigonal bipyramid. While the phenyl rings are not sufficiently disordered to warrant extensive disorder modelling, SIMU restraints were required to obtain reasonable ellipsoids for several of the carbon atoms in those ligands. Some of the thermal ellipsoids of the cyanide ligands are distorted, and ISOR restraints were used to obtain reasonable ellipsoids for those atoms. The Re atoms are not significantly distorted from their typical, trigonally distorted octahedral geometry. Re 1 has Re-C bond lengths of 2.064(11) Å, 2.050(11) Å, and 2.045(10) Å while Re2 has Re-C bond lengths of 2.055(10) Å, 2.052(10) Å, and 2.038(9)

Å. The average length of the bonds is slightly longer for Re1, which can be attributed to the steric bulk of the tmphen ligands on the V centers, all three of which point towards Re1. The P-Re-P angles are less than 90°, ranging from 84.010° – 87.327°. The P-Re-C angles for cis positions vary from 98.118° to 93.611°, while the trans P-Re-C angles vary from 175.177° to 178.900°. The V atoms are also octahedral, with two ligands each of N_{CN}, N_{tmphen}, and Cl. The bond lengths of the ligands around V are summarized in Table 20. The smallest cis N-V-N angle is 76.554°, which is smallest bite angle of the three tmphen moieties. The largest angle for each V center is the Cl-V-Cl angle, of which the largest is 97.806° for V1.

The V-N_{CN} bond lengths do not indicate that there are distinct oxidation states of the V atoms; but the charge assignment for the Re and V centers is not straightforward due to the lack of counterions in the structure. The total negative charge is -12 (from 6 CN^- and 6 Cl^-), but the total positive charge is only +11 if all V centers are divalent (3 V^{II}, 2 Re^{II}, and Na^+). Either the ion in the center of the structure is Mg^{2+} or there is one trivalent V center – there are no other obvious solutions to balance the charge in the structure. The V-N_{CN} bond lengths, however, are very similar to the bond lengths in $[V^{II}(tmphen)_2]_3[Mo^{III}(CN)_6]_2\cdot(MeOH)_{12}\cdot(MeCN)_2$,[78] a previously reported trigonal bipyramidal molecule in the Dunbar group, which is reported with three V^{II} centers. The average V_{CN} bond length in $[V^{II}(tmphen)_2]_3[Mo^{III}(CN)_6]_2\cdot(MeOH)_{12}\cdot(MeCN)_2$ is 2.028 Å, compared to 2.040 Å in **14**. More data are needed, especially magnetic measurements, to confidently assign the oxidation states of the V centers in **14**.

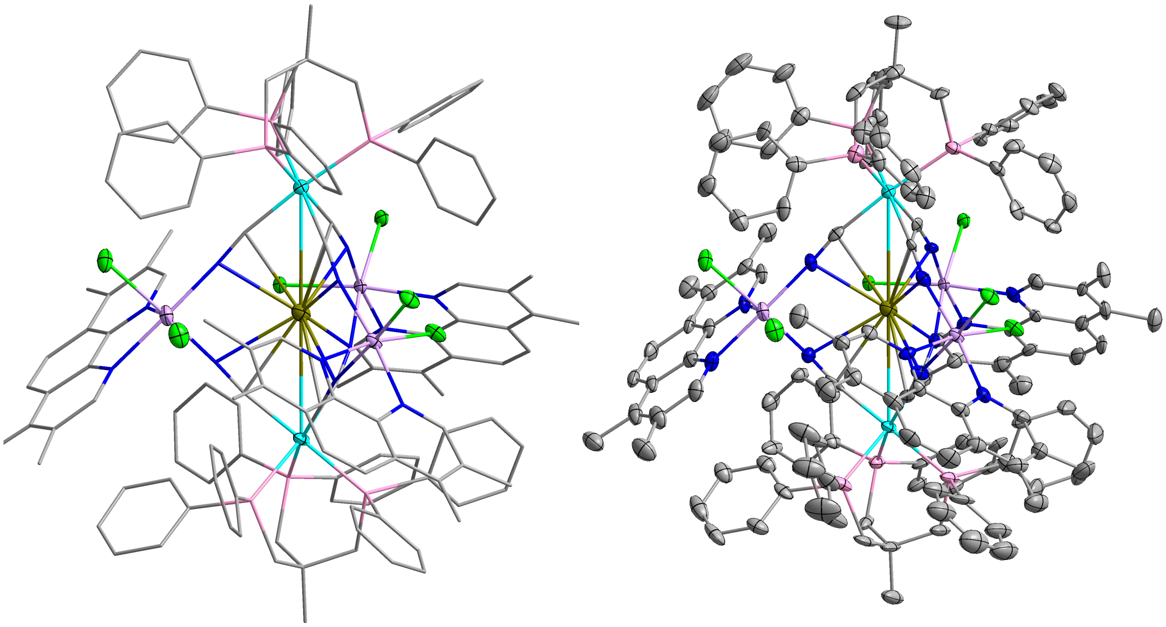

Figure 58. Thermal ellipsoids drawn at the 50% probability level and wireframe model of **14**.

Table 20. V-L bond distances for compound **14**.

	V1	V2	V3
V-Cl	2.319(3) Å	2.328(3) Å	2.335(3) Å
V-Cl	2.340(3) Å	2.330(3) Å	2.335(3) Å
V-N(CN)	2.017(8) Å	2.005(8) Å	2.017(8) Å
V-N(CN)	2.085(8) Å	2.059(8) Å	2.059(8) Å
V-N(tmphen)	2.117(8) Å	2.115(7) Å	2.121(8) Å
V-N(tmphen)	2.128(8) Å	2.150(8) Å	2.132(8) Å

Table 21. Crystal data and structure refinement for **14**.

Identification code	ReTBP
Empirical formula	$C_{140}H_{132}Cl_6N_{14}NaP_6Re_2V_3$
Formula weight	2957.32
Temperature/K	112.46
Crystal system	triclinic
Space group	P-1
a/Å	17.564(3)
b/Å	17.871(3)
c/Å	24.958(4)
α/°	82.009(5)
β/°	79.018(5)
γ/°	62.518(4)
Volume/Å^3	6810.8(18)
Z	2
ρ_{calc}g/cm^3	1.442
μ/mm^{-1}	2.214
F(000)	2984.0
Crystal size/mm^3	.1 × .1 × .08
Radiation	MoKα (λ = 0.71073)
2Θ range for data collection/°	4.326 to 47.894
Index ranges	$-20 \leq h \leq 18$, $-20 \leq k \leq 20$, $-28 \leq l \leq 28$
Reflections collected	225917
Independent reflections	21153 [$R_{int} = 0.1405$, $R_{sigma} = 0.0572$]
Data/restraints/parameters	21153/174/1560
Goodness-of-fit[a] on F^2	1.120
Final R indexes [I>=2σ (I)]	R_1[b] = 0.0645, wR_2 = 0.1273
Final R indexes [all data]	R_1[b] = 0.0884, wR_2 = 0.1365
Largest diff. peak/hole / e Å^{-3}	2.81/-2.53

[a] Goodness-of-fit = $\{\Sigma [w(Fo^2 - Fc^2)^2]/(n-p)\}^{1/2}$, where n is the number of reflections and p is the total number of parameters refined.

[b] $R = \Sigma || Fo | - | Fc || / \Sigma | Fo |$

[c] $wR = \{\Sigma [w(Fo^2 - Fc^2)^2] / \Sigma w(Fo^2)^2]\}^{1/2}$

Magnetic Measurements

Magnetic measurements were performed on a Quantum Design MPMS-XL SQUID magnetometer equipped with a 7 T magnet. A polypropylene bag was used to secure the sample, and the diamagnetic contribution was subtracted from the raw data. Diamagnetic contributions from the sample were accounted for by using Pascal's constants.[74]

There is substantial theoretical work to reference when interpreting the magnetic data for compounds containing $[(\text{triphos})\text{Re}^{\text{II}}(\text{CN})_3]^-$. Theoretical treatments of both the starting material[34] and the known SMM $[\{\text{MnCl}\}_4\{\text{Re}(\text{triphos})(\text{CN})_3\}_4]$[29] are relevant. In variable temperature static DC measurements of $[\text{Et}_4\text{N}][\text{Re}(\text{triphos})(\text{CN})_3]$, the χT value is a straight line, due to the influence of TIP. One cause of TIP, or Van Vleck paramagnetism, is the presence of low lying excited states in magnetic molecules and manifests as a consistent increase in χT as the temperature increases. In both $[\text{Et}_4\text{N}][\text{Re}(\text{triphos})(\text{CN})_3]$ and $[\{\text{MnCl}\}_4\{\text{Re}(\text{triphos})(\text{CN})_3\}_4]$, Re^{II} can be treated as a pseudo $S = ½$ center as the strong trigonal ligand field on Re splits the ground cubic state $^2T_2$ into $^2A_1$ and ^2E, and the ^2E term is the ground state.[29] The low temperature magnetization data can reveal information about the coupling, as shown in the theoretical treatment of $[\{\text{MnCl}\}_4\{\text{Re}(\text{triphos})(\text{CN})_3\}_4]$, despite the high anisotropy of the g-tensor of Re^{II}. Even in this case, where anisotropic exchange is involved, the saturation value of the low temperature magnetization was fit successfully with negative J values, suggesting antiferromagnetic exchange between the Mn^{II} and Re^{II} centers.

Variable temperature static DC magnetic susceptibility measurements were performed on crushed crystals of **12** from 300 to 2 K under an applied field of 1000 Oe (Figure 59). The χT decreases from 4.5 emu·Kmol^{-1} at 300K to 2.2 emu·Kmol^{-1} at 30K, then drops precipitously to .8 emu·Kmol^{-1} at 2K. The steady decrease in χT as the temperature is dropped is due to temperature independent paramagnetism (TIP), which, as mentioned above, is well documented in compounds of [(triphos)Re^{II}(CN)$_3$]$^-$.[29,34,41,129] The increased slope of χT at low temperature suggests antiferromagnetic coupling. Zero-field splitting contributions will be absent from both V^{II} and Re^{II} in these geometries, because V^{II} is isotropic (t_{2g}^3) and the Re^{II} center in [(triphos)Re^{II}(CN)$_3$]$^-$ which is a pseudo $S = ½$ that does not have zero-field splitting.[29] The 1.8 K magnetization data reach 1.9 μ_B in an applied field of 7T, but do not saturate. A value of 4 μ_B is the expected value for two S = 3/2 (g = 2) centers coupled antiferromagnetically to two S = 1/2 centers (g = 2) (Figure 60), which would lead to a ground state of S = 2, but the highly anisotropic Re^{II} center is not expected to match that value due to large anisotropy of the g tensor.

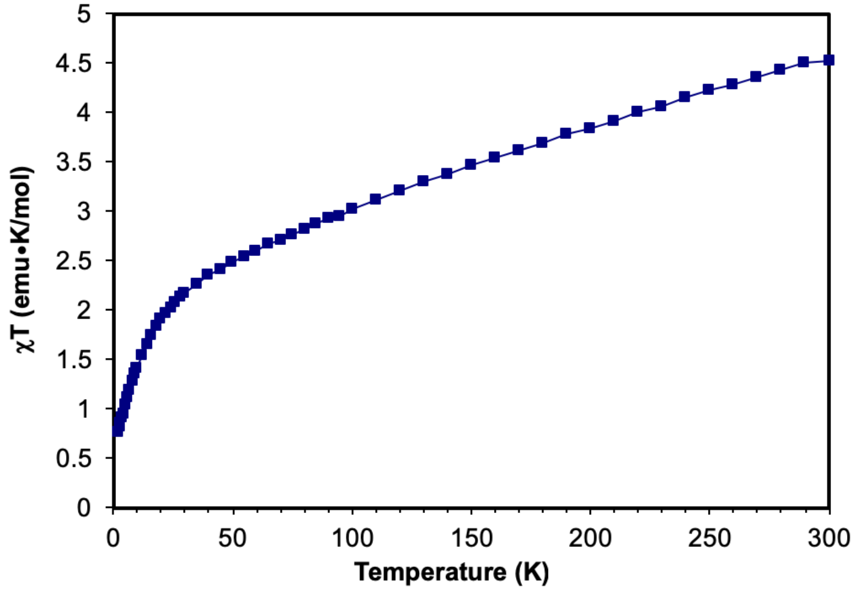

Figure 59. Magnetic susceptibility plot of **12** from 300 K – 2 K in an applied field of 1000 Oe.

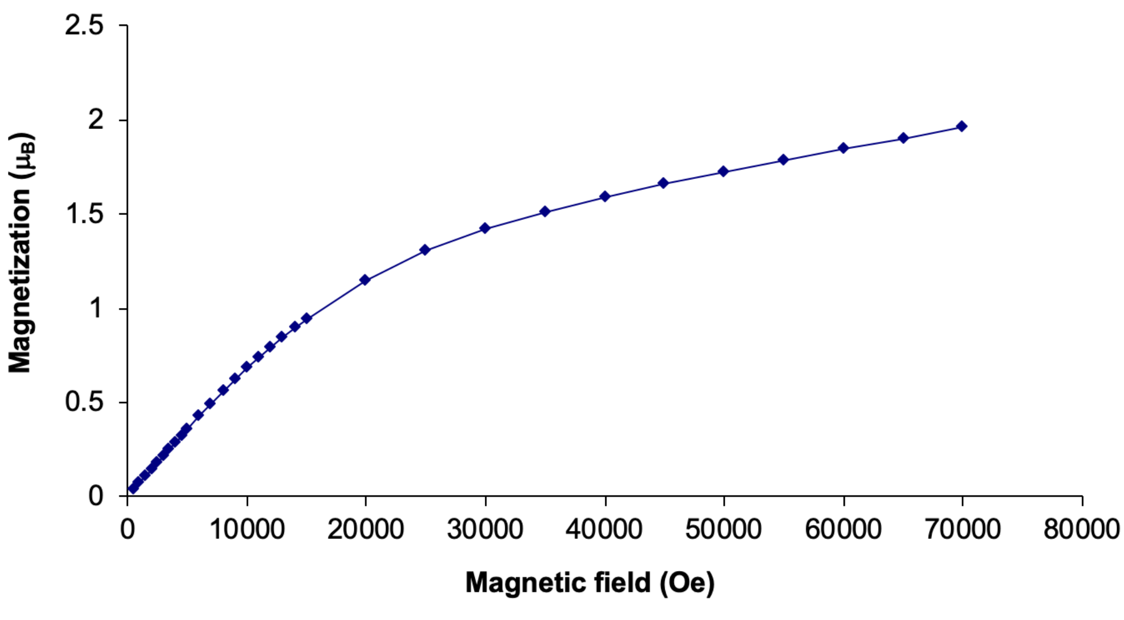

Figure 60. Magnetization data at 1.8 K of **12** at fields up to 7 T (70,000 Oe).

Non-superposition of the isofield lines in the reduced magnetization data (Figure 61) indicates that there is anisotropy in the system, which could originate from the spin-orbit coupling from Re. Despite the presence of anisotropy, Figure 62 shows a clear lack of SMM behavior. This result is attributed to the overall geometry of the molecule which does not exhibit an alignment of the 3-fold axes of the Re centers. Previous work with $[\{MnCl\}_4\{Re(triphos)(CN)_3\}_4]$ shows that the $[(triphos)Re^{II}(CN)_3]^-$ moiety has a proclivity to develop an easy axis along the C_3 axis, but this may not translate to easy axis anisotropy for molecules that are not symmetric about this axis.[29] Despite evidence of coupling to V^{II}, the molecule is not 3-fold symmetric, which confirms that this easy axis will not develop without such symmetry. Even if there were Ising-type anisotropy locally for each Re center, the failure to align the 3-fold axes of those metal centers precludes the development of Ising-type anisotropy for the molecule.

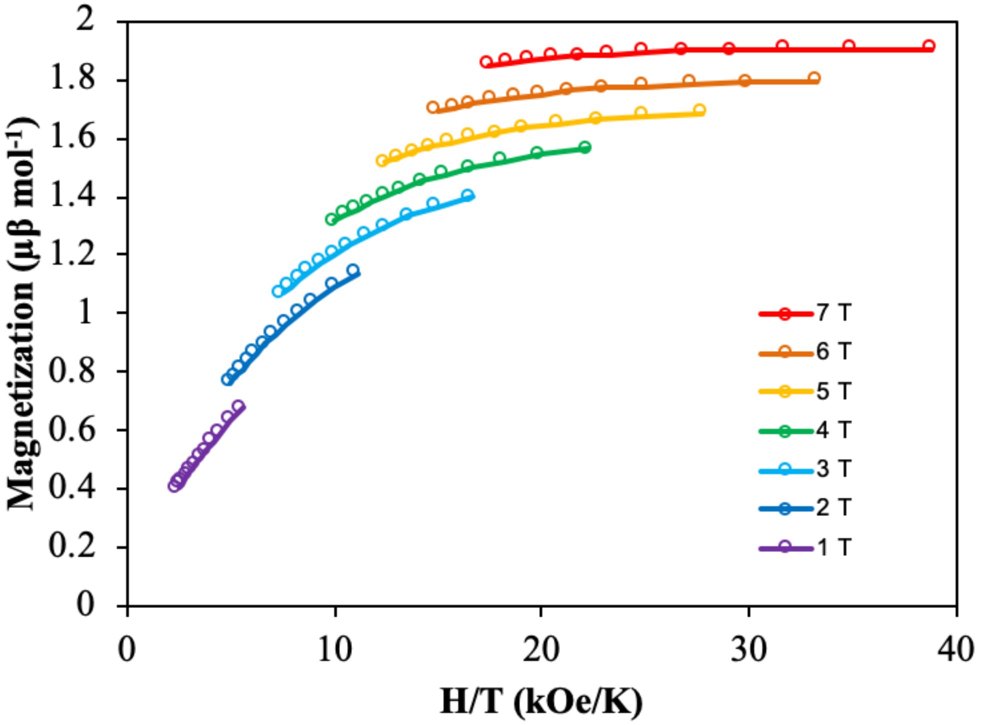

Figure 61. Reduced magnetization data for **12**. Solid lines are a guide for the eye.

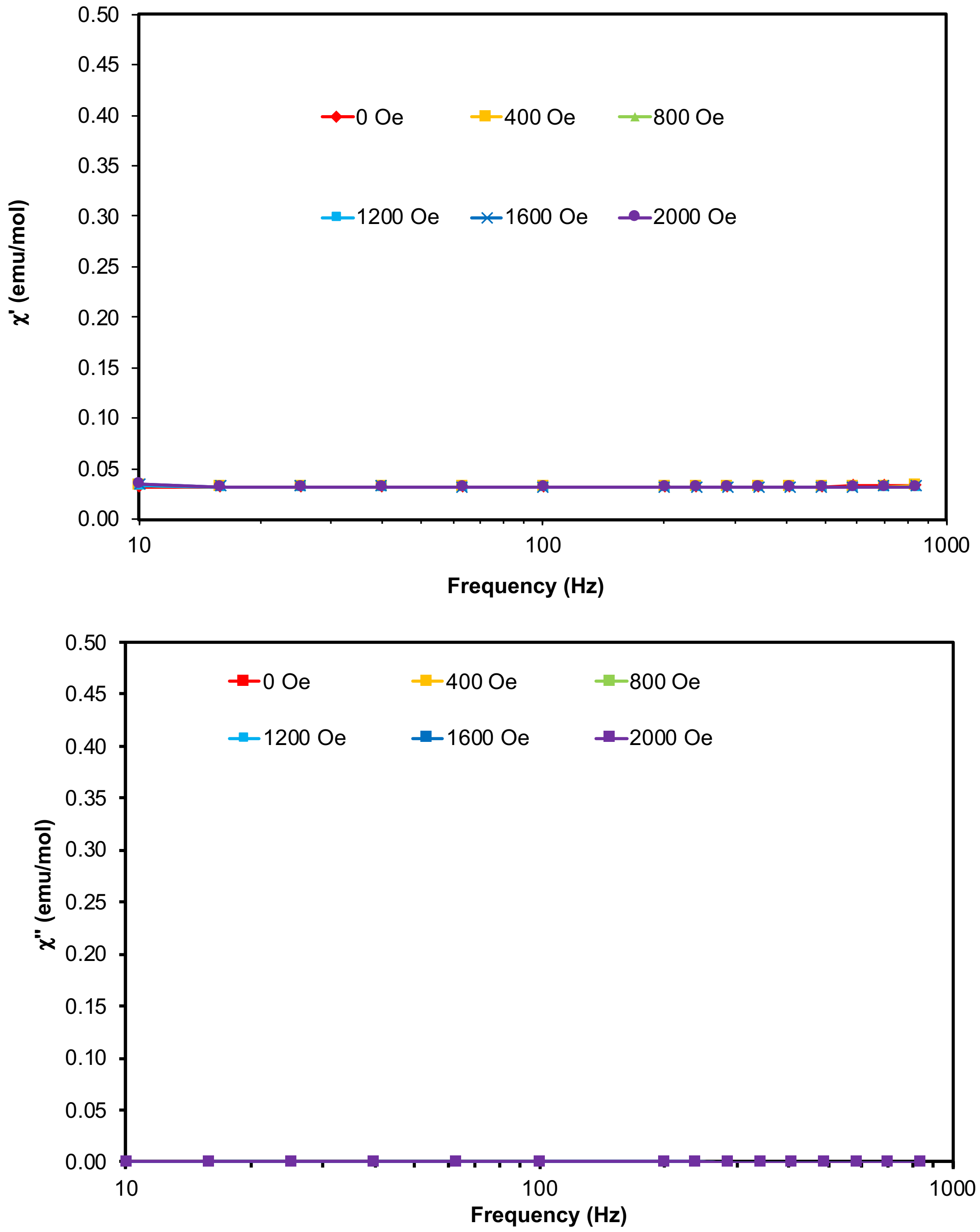

Figure 62. In-phase and out-of-phase susceptibility data for **12**, measured at 2 K with applied static DC fields from 0-2000 Oe.

Variable temperature static DC magnetic susceptibility measurements were also performed on crushed crystals of **13** from 300 to 2 K under an applied field of 1000 Oe (Figure 63). The value of χT decreases linearly from 11.1 emu·Kmol^{-1} to 2.8 emu·Kmol^{-1} as the temperature is lowered from 300 K to 2 K. This behavior can be attributed entirely to TIP. The magnetization data at 1.8 K saturate near $4\mu_B$ (Figure 64), which is consistent with a ground state of $S = 2$ for isotropic centers. As mentioned for **12**, though, Re^{II} is expected to be very anisotropic in this geometry, so it may be coincidence that the magnetization data saturate at $4\mu_B$.

The reduced magnetization of **13** (Figure 66) reveal complete overlap of the isofield lines which indicates a lack of anisotropy in the molecule, but probing for SMM behavior (Figure 65) shows minor beginnings of an out-of-phase signal. It is difficult to interpret the presence of an out-of-phase signal when there is no evidence of magnetic anisotropy, but the signal is very weak, as might be expected for a geometry that is not 3-fold symmetric around the [(triphos)Re^{II}(CN)$_3$]$^-$ anion.

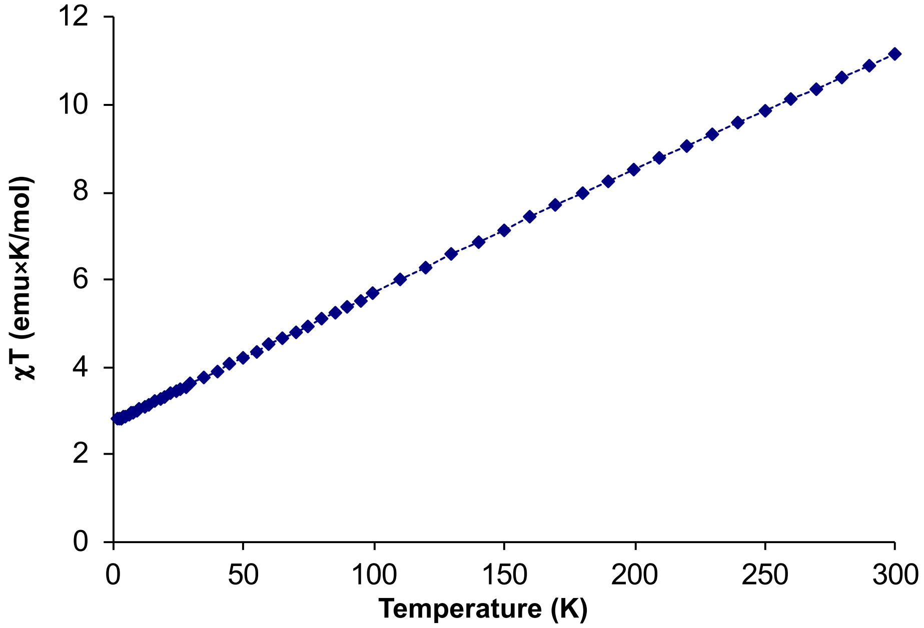

Figure 63. Magnetic susceptibility data for **13** from 300 K – 2K with an applied field of 1000 Oe.

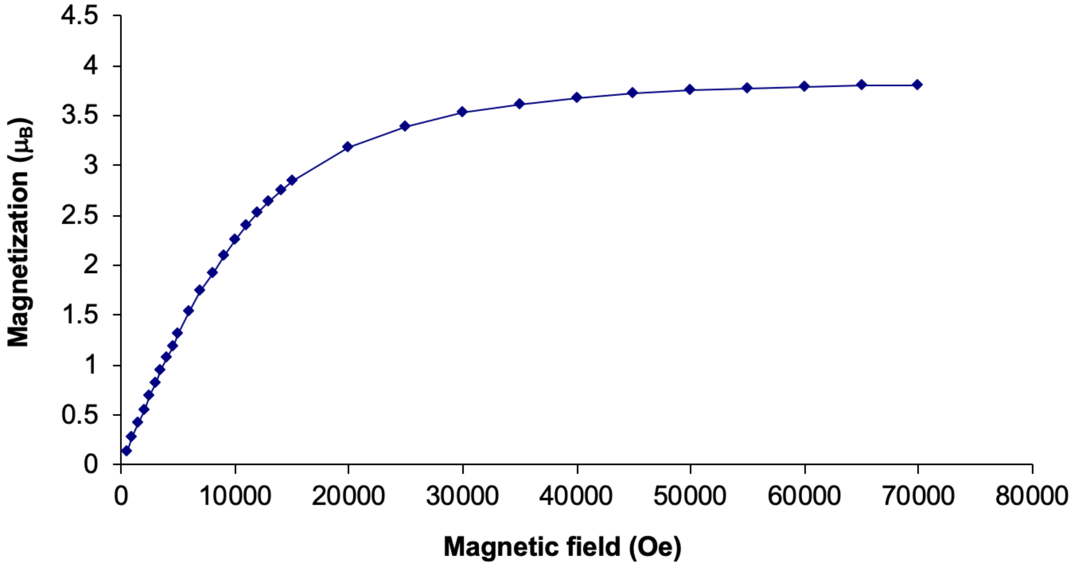

Figure 64. Magnetization data at 1.8 K for **13** at fields up to 7 T.

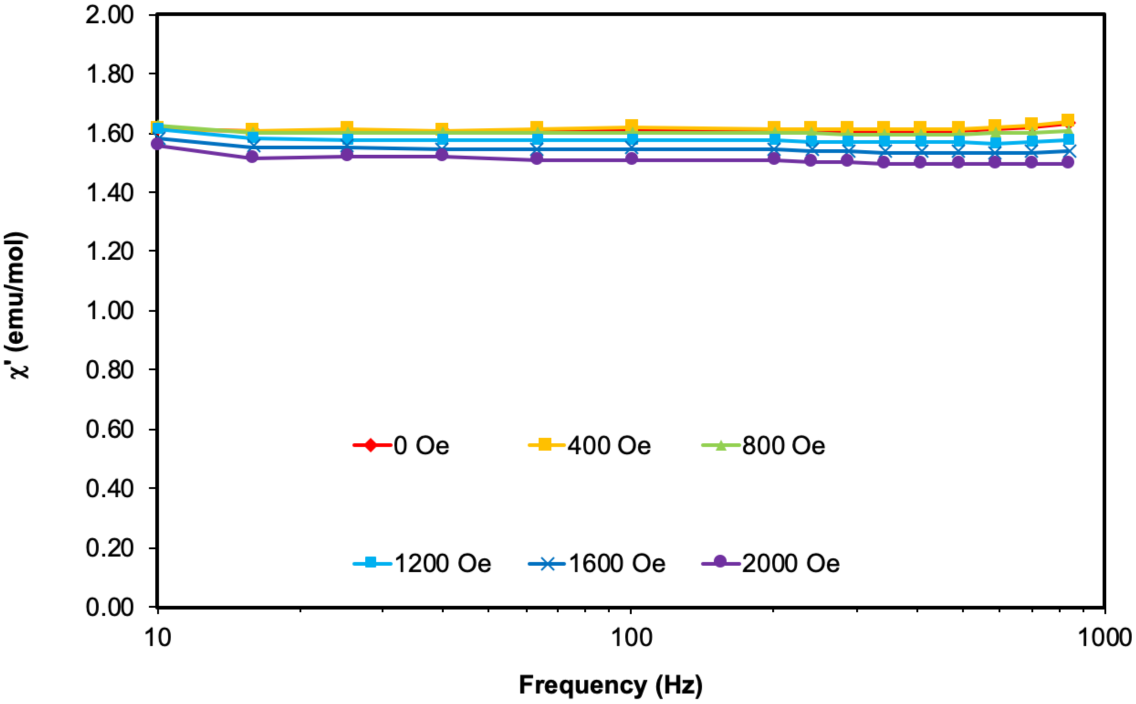

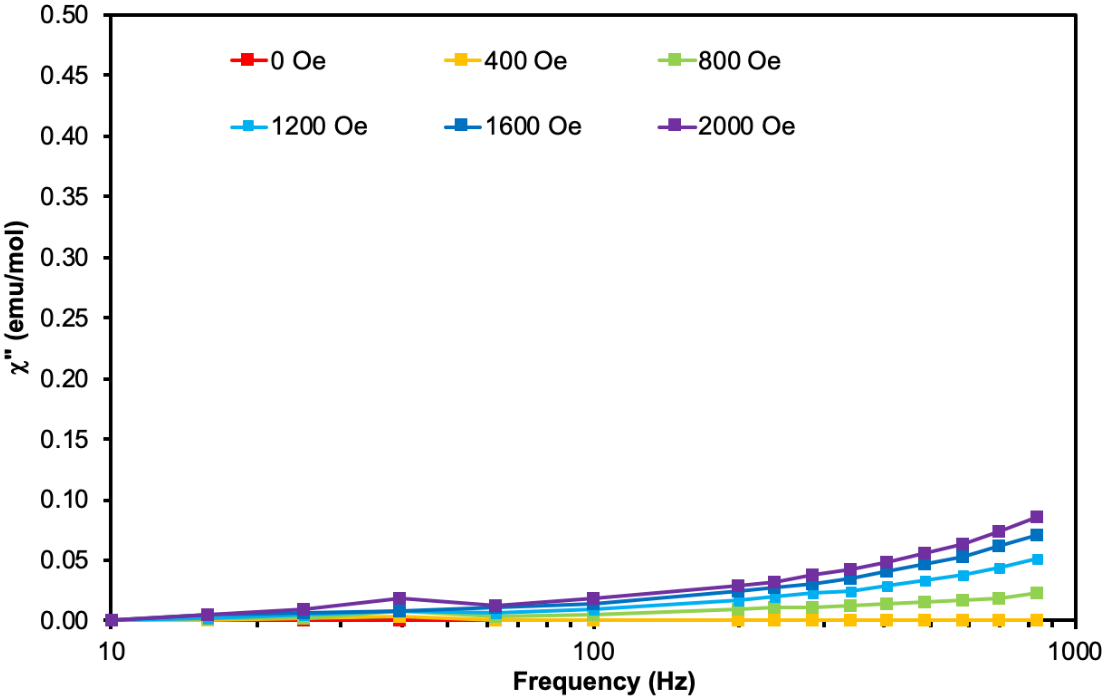

Figure 65. In-phase and out-of-phase susceptibility data for **13**, measured at 2 K with applied static DC fields from 0-2000 Oe.

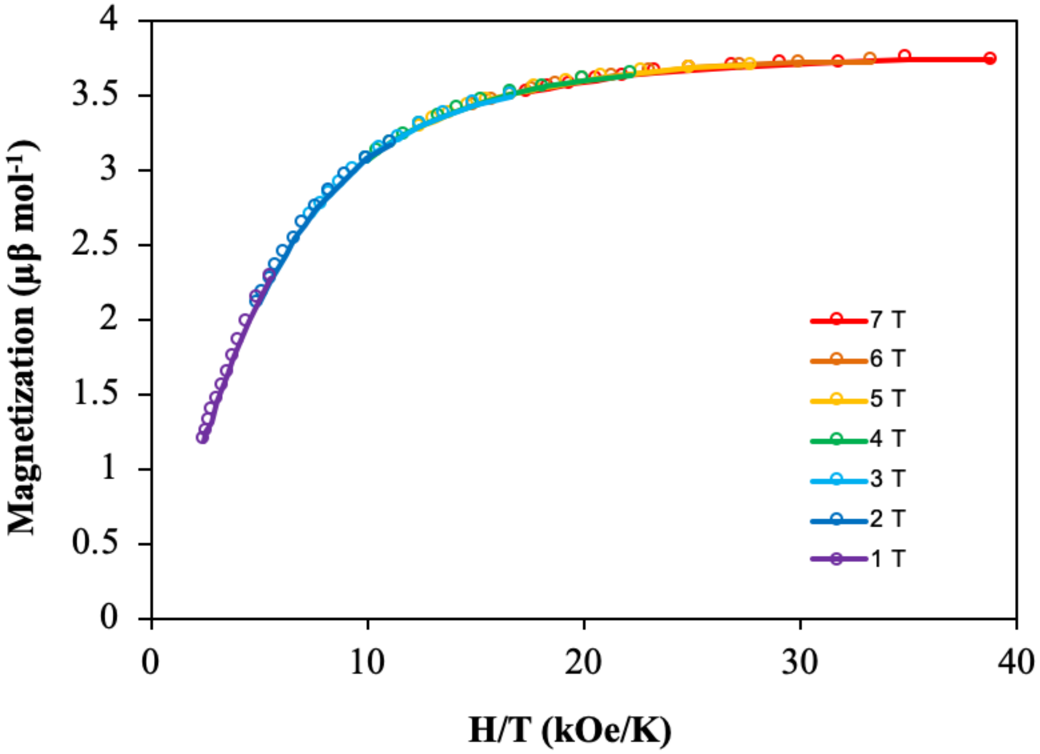

Figure 66. Reduced magnetization data for **13**. Solid lines are a guide for the eye.

Conclusions and Future Studies

The compounds **12** and **13** offer important insight regarding the need for specific geometries in compounds of $[(\text{triphos})\text{Re}^{\text{II}}(\text{CN})_3]^-$ to induce anisotropy. Compound **14** demonstrates the possibility of obtaining the proper geometries to generate Ising-type anisotropic exchange. Future work should focus on optimizing reactions of this type so that the magnetic properties of such compounds can be fully explored.

TIP remains an issue in the characterization of compounds that contain $[(\text{triphos})\text{Re}^{\text{II}}(\text{CN})_3]^-$. Deeper theoretical treatment of the data would allow for more information to be gleaned by fitting the magnetization and magnetic susceptibility data.

Finally, it is noteworthy that reactions with V^{II} resulted in no changes to the oxidation state of Re^{II}, which is critical to maintain orbital degeneracy in this system. Compound **14** is especially interesting due to the ambiguity of the oxidation states of the V^{II} centers in the compound. Full magnetic characterization of this molecule is needed to confidently assign oxidation states for the V centers, which will have significant impact on the magnetic properties of the molecule. Three V^{II} centers may be the best for SMM behavior in this molecule, but it may also be interesting to observe the effects of a $V^{II}/V^{II}/V^{III}$ configuration, which cannot be ruled out based on the crystallographic data. In order to fully characterize this molecule, it should be pursued intentionally as a synthetic target, with stoichiometric amounts of Cl^- and either Na^+ or Mg^{2+} in the reaction, so that the yield is not limited to a few small crystals. If **14** is found to exhibit SMM behavior, it would be another step towards fully understanding anisotropic exchange and using it to full effect in new heavy transition metal complexes.

CHAPTER V

CONCLUSIONS AND FUTURE WORK

The work described in this thesis was directed at exploring new directions for orbitally degenerate cyanometallate building blocks that are promising for the design of SMMs that exhibit anisotropic exchange coupling. While no SMMs were discovered, several new strategies were developed that may lead to new SMMs in the future.

In Chapter II, the potential for anisotropic exchange coupling with Mo^{III} and lanthanide centers was investigated. The resulting chains of formula $\{K[Ln(tmphen)_2(H_2O)_2Mo^{III}(CN)_7]\}$ (Ln = Gd, Tb, Dy, Ho, Er) did not exhibit SCM properties, but there is evidence of antiferromagnetic coupling in several of the chains. The best approach for future work with these molecule is the incorporation of a radical bridging ligand, rather than a diamagnetic one, that will engender stronger direct coupling between the orbitally degenerate Mo^{III} center and the lanthanide ion. In the case of superexchange, theoretical work on the $[Mo^{III}(CN)_7]^{4-}$ anion suggests that the best results are expected to occur with coupling an isotropic 3d metal to a pentagonal bipyramidal Mo^{III} center, so Gd is the best option for future work of this type.

In Chapter III, a new octadecanuclear wheel that incorporates $[Mo^{III}(CN)_7]^{4-}$ was described. This molecule is very similar to the octadecanuclear wheel that contains $[Mo^{IV}(CN)_8]^{4-}$, demonstrating that reactions of $[Mo^{IV}(CN)_8]^{4-}$ can be mimicked with $[Mo^{III}(CN)_7]^{4-}$ to introduce magnetic exchange interactions. New precursors were prepared that are expected to facilitate the synthesis of Mo^{III} containing SMMs. By imposing a pentagonal bipyramidal geometry on Mo^{III} in $[Mo^{III}DAPB(CN)_2]^-$, it is expected that the orbital degeneracy is maintained. That assertion can be tested using magnetic data and if true, it should be possible to prepare novel, polynuclear metal complexes that can be studied for Ising-type anisotropic exchange and SMM behavior.

In Chapter IV, new reactions of $[(\mathrm{triphos})\mathrm{Re}^{\mathrm{II}}(\mathrm{CN})_3]^-$ were presented that led to new compounds with interesting geometries. While none of the synthesized molecules were confirmed to be SMMs, one of them presents a geometry that is promising for future study, and may lead to significant advances in future work. In order to observe Ising-type anisotropic exchange, it is necessary to impose C_3 symmetry on compounds of $[(\mathrm{triphos})\mathrm{Re}^{\mathrm{II}}(\mathrm{CN})_3]^-$, and $\mathrm{Na}[\mathrm{V}^{\mathrm{II}}(\mathrm{tmphen})\mathrm{Cl}_2]_3[\mathrm{Re}(\mathrm{CN})_3(\mathrm{triphos})]_2\cdot 2\mathrm{MeCN}$ (**14**) meets this requirement. Future work should expand on this strategy with other 3d metals, including $\mathrm{Mn}^{\mathrm{II}}$, for comparison and a systematic study of anisotropic exchange.

The most promising compounds presented herein for generating Ising-type anisotropic exchange are $\mathrm{Na}[\mathrm{V}^{\mathrm{II}}(\mathrm{tmphen})\mathrm{Cl}_2]_3[\mathrm{Re}(\mathrm{CN})_3(\mathrm{triphos})]_2\cdot 2\mathrm{MeCN}$ (**14**), $(\mathrm{NEt}_4)[\mathrm{Mo}^{\mathrm{III}}(\mathrm{DAPB})(\mathrm{CN})_2]$ (**10**), and $\mathrm{K}[\mathrm{Mo}^{\mathrm{III}}(\mathrm{DAPB})(\mathrm{CN})_2]$ (**11**). Magnetic measurements are needed for compound **14** to test the hypothesis that this molecule should exhibit Ising-type anisotropic exchange and therefore behave as an SMM. Compounds **10** and **11** are excellent new starting materials for future work that seeks to probe the conditions and requirements for Ising-type anisotropic exchange. By attaching different transition metal centers to the apical positions of a pentagonal, bipyramidal $\mathrm{Mo}^{\mathrm{III}}$ center, it will be possible to tune the properties of the resulting molecules and draw important conclusions that can be leveraged to make progress in future experiments.

The incorporation of new organic ligands and new metal combinations can only serve to increase the knowledge in the field. As new methods and new molecules are developed, incorporating these ideas into novel electronic devices becomes increasingly promising. Anisotropic exchange is still poorly understood due to a dearth of results on the topic, but the work presented here offers good starting points for future work and may lead to promising directions for the field of molecular magnetism.

REFERENCES

1 Sessoli, R.; Gatteschi, D.; Canechi, A.; Novak, M. A. *Nature* **1993**, *365*, 141-143.

2 Lis, T. *Acta Crystallographica Section B* **1980**, *36*, 2042-2046.

3 Caneschi, A.; Gatteschi, D.; Sessoli, R.; Barra, A. L.; Brunel, L. C.; Guillot, M. *J. Am. Chem. Soc.* **1991**, *113*, 5873-5874.

4 Sessoli, R.; Gatteschi, D.; Caneschi, A.; Novak, M. A. *Nature* **1993**, *365*, 141.

5 Sessoli, R.; Tsai, H. L.; Schake, A. R.; Wang, S.; Vincent, J. B.; Folting, K.; Gatteschi, D.; Christou, G.; Hendrickson, D. N. *J. Am. Chem. Soc.* **1993**, *115*, 1804-1816.

6 *Molecular Magnetism: From Molecular Assemblies to the Devices*. Coronado, E.; Delhaès, P.; Gatteschi, D.; Miller, J. S., Eds.; NATO Advanced Science Institute Series E: Applied Sciences 321; Kluwer Academic: Dordrecht, 1996.

7 *Molecular Nanomagnets*. Gatteschi, D.; Sessoli, R.; Villain, J., Eds.; Mesoscopic Physics and Nanotechnology 5; Oxford University Press: Oxford, 2006.

8 Troiani, F.; Affronte, M. *Chem. Soc. Rev.* **2011**, *40*, 3119-3129.

9 Timco, G. A.; Carretta, S.; Troiani, F.; Tuna, F.; Pritchard, R. J.; Muryn, C. A.; McInnes, E. J. L.; Ghirri, A.; Candini, A.; Santini, P.; Amoretti, G.; Affronte, M.; Winpenny, R. E. P. *Nat. Nanotech.* **2009**, *4*, 173-178.

10 Heersche, H. B.; de Groot, Z.; Folk, J. A.; van der Zant, H. S. J.; Romeike, C.; Wegewijs, M. R.; Zobbi, L.; Barreca, D.; Tondello, E.; Cornia, A. *Physical Review Letters* **2006**, *96*, 206801.

11 Leuenberger, M. N.; Loss, D. *Nature* **2001**, *410*, 789-793.

12 Gaita-Ariño, A.; Luis, F.; Hill, S.; Coronado, E. *Nat. Chem.* **2019**, *11*, 301-309.

13 Guo, F.-S.; Day, B. M.; Chen, Y.-C.; Tong, M.-L.; Mansikkamäki, A.; Layfield, R. A. *Science* **2018**, *362*, 1400-1403.

14 Wernsdorfer, W. *Adv. Chem. Phys.* **2001**, *118*, 99-190.

15 Ako, A. M.; Hewitt, I. J.; Mereacre, V.; Clérac, R.; Wernsdorfer, W.; Anson, C. E.; Powell, A. K. *Angew. Chem. Int. Ed.* **2006**, *45*, 4926-4929.

16 Wang, X.-Y.; Prosvirin, A. V.; Dunbar, K. R. *Angew. Chem. Int. Ed.* **2010**, *49*, 5081-5084.

17 Waldmann, O. *Inorg. Chem.* **2007**, *46*, 10035-10037.

18 Gomez-Coca, S.; Cremades, E.; Aliaga-Alcalde, N.; Ruiz, E. *J. Am. Chem. Soc.* **2013**, *135*, 7010-7018.

19 Yao, X.-N.; Du, J.-Z.; Zhang, Y.-Q.; Leng, X.-B.; Yang, M.-W.; Jiang, S.-D.; Wang, Z.-X.; Ouyang, Z.-W.; Deng, L.; Wang, B.-W.; Gao, S. *J. Am. Chem. Soc.* **2017**, *139*, 373-380.

20 Zadrozny, J. M.; Xiao, D. J.; Atanasov, M.; Long, G. J.; Grandjean, F.; Neese, F.; Long, J. R. *Nat Chem* **2013**, *5*, 577-581.

21 Mironov, V. S. *Dokl. Phys. Chem.* **2004**, *397*, 154-157.

22 Feng, M.; Tong, M. L. *Chem. Eur. J.* **2018**, *24*, 7574-7594.

23 Ferlay, S.; Mallah, T.; Ouahes, R.; Veillet, P.; Verdaguer, M. *Nature* **1995**, *378*, 701-703.

24 Kramers, H. A. *Physica* **1934**, *1*, 182-192.

25 Anderson, P. W. *Physical Review* **1950**, *79*, 350-356.

26 Yamaguchi, T.; Costes, J.-P.; Kishima, Y.; Kojima, M.; Sunatsuki, Y.; Bréfuel, N.; Tuchagues, J.-P.; Vendier, L.; Wernsdorfer, W. *Inorg. Chem.* **2010**, *49*, 9125-9135.

27 Ungur, L.; Thewissen, M.; Costes, J.-P.; Wernsdorfer, W.; Chibotaru, L. F. *Inorg. Chem.* **2013**, *52*, 6328-6337.

28 Mironov, V. S.; Chibotaru, L. F.; Ceulemans, A. *J. Am. Chem. Soc.* **2003**, *125*, 9750-9760.

29 Palii, A. V.; Ostrovsky, S. M.; Klokishner, S. I.; Tsukerblat, B. S.; Schelter, E. J.; Prosvirin, A. V.; Dunbar, K. R. *Inorg. Chim. Acta.* **2007**, *360*, 3915-3924.

30 Piligkos, S.; Bill, E.; Collison, D.; McInnes, E. J. L.; Timco, G. A.; Weihe, H.; Winpenny, R. E. P.; Neese, F. *J. Am. Chem. Soc.* **2007**, *129*, 760-761.

31 Westrup, K. C. M.; Boulon, M. E.; Totaro, P.; Nunes, G. G.; Back, D. F.; Barison, A.; Jackson, M.; Paulsen, C.; Gatteschi, D.; Sorace, L.; Cornia, A.; Soares, J. F.; Sessoli, R. *Chem. Eur. J.* **2014**, *20*, 13681-13691.

32 Shatruk, M.; Avendano, C.; Dunbar, K. R., Cyanide-Bridged Complexes of Transition Metals: A Molecular Magnetism Perspective. In Progress in Inorganic Chemistry, John Wiley & Sons, Inc.: 2009; pp 155-334.

33 Pedersen, K. S.; Bendix, J.; Clerac, R. *Chem. Commun.* **2014**, *50*, 4396-4415.

34 Dunbar, K. R.; Schelter, E. J.; Palii, A. V.; Ostrovsky, S. M.; Mirovitskii, V. Y.; Hudson, J. M.; Omary, M. A.; Klokishner, S. I.; Tsukerblat, B. S. *J. Phys. Chem. A.* **2003**, *107*, 11102-11111.

35 Schelter, E. J.; Bera, J. K.; Bacsa, J.; Galán-Mascarós, J. R.; Dunbar, K. R. *Inorg. Chem.* **2003**, *42*, 4256-4258.

36 Schelter, E. J.; Prosvirin, A. V.; Dunbar, K. R. *J. Am. Chem. Soc.* **2004**, *126*, 15004-15005.

37 Schelter, E. J.; Prosvirin, A. V.; Reiff, W. M.; Dunbar, K. R. *Angew. Chem. Int. Ed.* **2004**, *43*, 4912-4915.

38 Qian, K.; Huang, X.-C.; Zhou, C.; You, X.-Z.; Wang, X.-Y.; Dunbar, K. R. *J. Am. Chem. Soc.* **2013**, *135*, 13302-13305.

39 Wu, D.-Q.; Shao, D.; Wei, X.-Q.; Shen, F.-X.; Shi, L.; Kempe, D.; Zhang, Y.-Z.; Dunbar, K. R.; Wang, X.-Y. *J. Am. Chem. Soc.* **2017**, *139*, 11714-11717.

40 Mironov, V. *Inorganics* **2018**, *6*, 58.

41 Schelter, E. J.; Karadas, F.; Avendano, C.; Prosvirin, A. V.; Wernsdorfer, W.; Dunbar, K. R. *J. Am. Chem. Soc.* **2007**, *129*, 8139-8149.

42 Glauber, R. J. *Journal of Mathematical Physics* **1963**, *4*, 294-307.

43 Caneschi, A.; Gatteschi, D.; Lalioti, N.; Sangregorio, C.; Sessoli, R.; Venturi, G.; Vindigni, A.; Rettori, A.; Pini, M. G.; Novak, M. A. *Angew. Chem. Int. Ed.* **2001**, *40*, 1760-1763.

44 Bogani, L.; Vindigni, A.; Sessoli, R.; Gatteschi, D. *Journal of Materials Chemistry* **2008**, *18*, 4750-4758.

45 Sun, H.-L.; Wang, Z.-M.; Gao, S. *Coord. Chem. Rev.* **2010**, *254*, 1081-1100.

46 Kajiwara, T.; Nakano, M.; Kaneko, Y.; Takaishi, S.; Ito, T.; Yamashita, M.; Igashira-Kamiyama, A.; Nojiri, H.; Ono, Y.; Kojima, N. *J. Am. Chem. Soc.* **2005**, *127*, 10150-10151.

47 Lescouëzec, R.; Vaissermann, J.; Ruiz-Pérez, C.; Lloret, F.; Carrasco, R.; Julve, M.; Verdaguer, M.; Dromzee, Y.; Gatteschi, D.; Wernsdorfer, W. *Angew. Chem. Int. Ed.* **2003**, *42*, 1483-1486.

48 Wang, S.; Zuo, J.-L.; Gao, S.; Song, Y.; Zhou, H.-C.; Zhang, Y.-Z.; You, X.-Z. *J. Am. Chem. Soc.* **2004**, *126*, 8900-8901.

49 Ferbinteanu, M.; Miyasaka, H.; Wernsdorfer, W.; Nakata, K.; Sugiura, K.-i.; Yamashita, M.; Coulon, C.; Clérac, R. *J. Am. Chem. Soc.* **2005**, *127*, 3090-3099.

50 Toma, L. M.; Lescouëzec, R.; Pasán, J.; Ruiz-Pérez, C.; Vaissermann, J.; Cano, J.; Carrasco, R.; Wernsdorfer, W.; Lloret, F.; Julve, M. *J. Am. Chem. Soc.* **2006**, *128*, 4842-4853.

51 Wen, H.-R.; Wang, C.-F.; Song, Y.; Gao, S.; Zuo, J.-L.; You, X.-Z. *Inorg. Chem.* **2006**, *45*, 8942-8949.

52 Guo, J.-F.; Wang, X.-T.; Wang, B.-W.; Xu, G.-C.; Gao, S.; Szeto, L.; Wong, W.-T.; Wong, W.-Y.; Lau, T.-C. *Chem. Eur. J.* **2010**, *16*, 3524-3535.

53 Larionova, J.; Clérac, R.; Sanchiz, J.; Kahn, O.; Golhen, S.; Ouahab, L. *J. Am. Chem. Soc.* **1998**, *120*, 13088-13095.

54 Larionova, J.; Sanchiz, J.; Kahn, O.; Gohlen, S.; Ouahab, L. *Chem. Commun.* **1998**, 953-954.

55 Kaur Sra, A.; Andruh, M.; Kahn, O.; Golhen, S.; Ouahab, L.; Yakhmi, J. V. *Angew. Chem. Int. Ed.* **1999**, *38*, 2606-2609.

56 Larionova, J.; Kahn, O.; Bartolome, J.; Burriel, R.; Castro, M.; Ksenofontov, V.; Gütlich, P. *Chem. Mater.* **1999**, *11*, 3400-3405.

57 Larionova, J.; Kahn, O.; Gohlen, S.; Ouahab, L.; Clérac, R. *J. Am. Chem. Soc.* **1999**, *121*, 3349-3356.

58 Sra, A. K.; Rombaut, G.; Lahitete, F.; Golhen, S.; Ouahab, L.; Mathoniere, C.; Yakhmi, J. V.; Kahn, O. *New J. Chem.* **2000**, *24*, 871-876.

59 Larionova, J.; Clérac, R.; Donnadieu, B.; Guérin, C. *Chem. Eur. J.* **2002**, *8*, 2712-2716.

60 Sra, A. K.; Lahitite, F.; Yakhmi, J. V.; Kahn, O. *Physica B.* **2002**, *321*, 87-90.

61 Tanase, S.; Tuna, F.; Guionneau, P.; Maris, T.; Rombaut, G.; Mathonière, C.; Andruh, M.; Kahn, O.; Sutter, J.-P. *Inorg. Chem.* **2003**, *42*, 1625-1631.

62 Le Goff, X. F.; Willemin, S.; Coulon, C.; Larionova, J.; Donnadieu, B.; Clérac, R. *Inorg. Chem.* **2004**, *43*, 4784-4786.

63 Tomono, K.; Tsunobuchi, Y.; Nakabayashi, K.; Kosaka, W.; Matsuda, T.; Ohkoshi, S.-i. *Chem. Lett.* **2009**, *38*, 810-811.

64 Tomono, K.; Tsunobuchi, Y.; Nakabayashi, K.; Ohkoshi, S.-i. *Inorg. Chem.* **2010**, *49*, 1298-1300.

65 Wu, D.-Q.; Kempe, D.; Zhou, Y.; Deng, L.-D.; Shao, D.; Wei, X.-Q.; Shi, L.; Dunbar, K. R.; Wang, X.-Y. *Inorg. Chem.* **2017**, *56*, 7182-7189.

66 Zhao, H.; Lopez, N.; Prosvirin, A.; Chifotides, H. T.; Dunbar, K. R. *Dalton Trans.* **2007**, 878-888.

67 Kempe, D. K.; Dolinar, B. S.; Vignesh, K. R.; Woods, T. J.; Saber, M. R.; Dunbar, K. R. *Chem. Commun.* **2019**, *55*, 2098-2101.

68 Krause, L.; Herbst-Irmer, R.; Sheldrick, G. M.; Stalke, D. *Journal of Applied Crystallography* **2015**, *48*, 3-10.

69 APEX3, 1; Bruker AXS Inc.: Madison, WI, 2016.

70 Sheldrick, G. *Acta Crystallographica Section A* **2015**, *71*, 3-8.

71 Sheldrick, G. *Acta. Cryst.* **2015**, *71*, 3-8.

72 Dolomanov, O. V.; Bourhis, L. J.; Gildea, R. J.; Howard, J. A. K.; Puschmann, H. *Journal of Applied Crystallography* **2009**, *42*, 339-341.

73 Spek, A. *Journal of Applied Crystallography* **2003**, *36*, 7-13.

74 Bain, G. A.; Berry, J. F. *J. Chem. Ed.* **2008**, *85*, 532.

75 Sieklucka, B.; Podgajny, R.; Pinkowicz, D.; Nowicka, B.; Korzeniak, T.; Balanda, M.; Wasiutynski, T.; Pelka, R.; Makarewicz, M.; Czapla, M.; Rams, M.; Gawel, B.; Lasocha, W. *Cryst. Eng. Comm.* **2009**, *11*, 2032-2039.

76 Wang, X.-Y.; Avendano, C.; Dunbar, K. R. *Chem. Soc. Rev.* **2011**, *40*, 3213-3238.

77 Frost, J. M.; Harriman, K. L. M.; Murugesu, M. *Chem. Sci.* **2016**, *7*, 2470-2491.

78 Pinkowicz, D.; Southerland, H.; Wang, X.-Y.; Dunbar, K. R. *J. Am. Chem. Soc.* **2014**, *136*, 9922-9924.

79 Harris, T. D.; Coulon, C.; Clérac, R.; Long, J. R. *J. Am. Chem. Soc.* **2011**, *133*, 123-130.

80 Abu-Nawwas, A.-A. H.; Cano, J.; Christian, P.; Mallah, T.; Rajaraman, G.; Teat, S. J.; Winpenny, R. E. P.; Yukawa, Y. *Chem. Commun.* **2004**, *0*, 314-315.

81 Affronte, M.; Carretta, S.; Timco, G. A.; Winpenny, R. E. P. *Chem. Commun.* **2007**, *0*, 1789-1797.

82 Saalfrank, R. W.; Scheurer, A.; Prakash, R.; Heinemann, F. W.; Nakajima, T.; Hampel, F.; Leppin, R.; Pilawa, B.; Rupp, H.; Müller, P. *Inorg. Chem.* **2007**, *46*, 1586-1592.

83 Hoshino, N.; Ako, A. M.; Powell, A. K.; Oshio, H. *Inorg. Chem.* **2009**, *48*, 3396-3407.

84 Langley, S. K.; Moubaraki, B.; Forsyth, C. M.; Gass, I. A.; Murray, K. S. *Dalton Trans.* **2010**, *39*, 1705-1708.

85 Muche, S.; Levacheva, I.; Samsonova, O.; Pham, L.; Christou, G.; Bakowsky, U.; Hołyńska, M. *Inorg. Chem.* **2014**, *53*, 7642-7649.

86 Vignesh, K. R.; Langley, S. K.; Moubaraki, B.; Murray, K. S.; Rajaraman, G. *Chem. Eur. J.* **2015**, *21*, 16364-16369.

87 Huo, Y.; Chen, Y.-C.; Liu, J.-L.; Jia, J.-H.; Chen, W.-B.; Wu, S.-G.; Tong, M.-L. *Dalton Trans.* **2017**, *46*, 16796-16801.

88 Zheng, X.-Y.; Jiang, Y.-H.; Zhuang, G.-L.; Liu, D.-P.; Liao, H.-G.; Kong, X.-J.; Long, L.-S.; Zheng, L.-S. *J. Am. Chem. Soc.* **2017**, *139*, 18178-18181.

89 Ni, Z.-H.; Kou, H.-Z.; Zhang, L.-F.; Ge, C.; Cui, A.-L.; Wang, R.-J.; Li, Y.; Sato, O. *Angew. Chem. Int. Ed.* **2005**, *44*, 7742-7745.

90 Ni, Z.-H.; Zhang, L.-F.; Tangoulis, V.; Wernsdorfer, W.; Cui, A.-L.; Sato, O.; Kou, H.-Z. *Inorg. Chem.* **2007**, *46*, 6029-6037.

91 Ni, Z.; Zhang, L.; Cui, A.; Kou, H. *Sci. China, Ser. B: Chem.* **2009**, *52*, 1444-1450.

92 Zhang, D.; Kong, L.; Zhang, H.; Wang, P. *Z. Naturforsch. B Chem. Sci.* **2015**, *70*, 527.

93 Zhang, D.-P.; Zhang, L.-F.; Li, G.-L.; Ni, Z.-H. *Chem. Commun.* **2013**, *49*, 9582-9584.

94 Pradhan, R.; Desplanches, C.; Guionneau, P.; Sutter, J.-P. *Inorg. Chem.* **2003**, *42*, 6607-6609.

95 Mironov, V. S. *Inorg. Chem.* **2015**, *54*, 11339-11355.

96 Young, R. C. *J. Am. Chem. Soc.* **1932**, *54*, 1402-1405.

97 Lorenzini, C.; Pelizzi, C.; Pelizzi, G.; Predieri, G. *J. Chem. Soc. Dalton.* **1983**, 721-727.

98 Al-Shihri, A. S. M.; Dilworth, J. R.; Howe, S. D.; Silver, J.; Thompson, R. M.; Davies, J.; Povey, D. C. *Polyhedron* **1993**, *12*, 2297-2305.

99 Pichon, C.; Elrez, B.; Béreau, V.; Duhayon, C.; Sutter, J.-P. *Eur. J. Inorg. Chem.* **2018**, *2018*, 340-348.

100 Maria, S.; Poli, R.; Gallagher, K. J.; Hock, A. S.; Johnson, M. J. A., Ether Complexes of Molybdenum(III) and Molybdenum(IV) chlorides. In Inorganic Syntheses: Volume 36, John Wiley & Sons, Inc.: 2014; pp 15-18.

101 Karn, J. L.; Busch, D. H. *Inorg. Chem.* **1969**, *8*, 1149-1153.

102 Alvarez, S.; Alemany, P.; Casanova, D.; Cirera, J.; Llunell, M.; Avnir, D. *Coord. Chem. Rev.* **2005**, *249*, 1693-1708.

103 Llunell, M.; Casanova, D.; Cirera, J.; Alemany, P.; Alvarez, S. SHAPE, version 2.1; Universitat de Barcelona: Barcelona, Spain, 2010.

104 Mironov, V. S.; Bazhenova, T. A.; Manakin, Y. V.; Lyssenko, K. A.; Talantsev, A. D.; Yagubskii, E. B. *Dalton Trans.* **2017**, *46*, 14083-14087.

105 Jeon, I.-R.; David Harris, T. *Chem. Commun.* **2016**, *52*, 1006-1008.

106 Becke, A. D. *Journal of Chemical Physics* **1993**, *98*, 5648-5652.

107 Schaefer, A.; Horn, H.; Ahlrichs, R. *Journal of Chemical Physics* **1992**, *97*, 2571-2577.

108 Schaefer, A.; Huber, C.; Ahlrichs, R. *Journal of Chemical Physics* **1994**, *100*, 5829-5835.

109 Hay, P. J.; Wadt, W. R. *The Journal of Chemical Physics* **1985**, *82*, 270-283.

110 Frisch, M. J.; Trucks, G. W.; Schlegel, H. B.; Scuseria, G. E.; Robb, M. A.; Cheeseman, J. R.; Scalmani, G.; Barone, V.; Mennucci, B.; Petersson, G. A.;

Nakatsuji, H.; Caricato, M.; Li, X.; Hratchian, H. P.; Izmaylov, A. F.; Bloino, J.; Zheng, G.; Sonnenberg, J. L.; Hada, M.; Ehara, M.; Toyota, K.; Fukuda, R.; Hasegawa, J.; Ishida, M.; Nakajima, T.; Honda, Y.; Kitao, O.; Nakai, H.; Vreven, T.; Montgomery Jr., J. A.; Peralta, J. E.; Ogliaro, F.; Bearpark, M. J.; Heyd, J.; Brothers, E. N.; Kudin, K. N.; Staroverov, V. N.; Kobayashi, R.; Normand, J.; Raghavachari, K.; Rendell, A. P.; Burant, J. C.; Iyengar, S. S.; Tomasi, J.; Cossi, M.; Rega, N.; Millam, N. J.; Klene, M.; Knox, J. E.; Cross, J. B.; Bakken, V.; Adamo, C.; Jaramillo, J.; Gomperts, R.; Stratmann, R. E.; Yazyev, O.; Austin, A. J.; Cammi, R.; Pomelli, C.; Ochterski, J. W.; Martin, R. L.; Morokuma, K.; Zakrzewski, V. G.; Voth, G. A.; Salvador, P.; Dannenberg, J. J.; Dapprich, S.; Daniels, A. D.; Farkas, Ö.; Foresman, J. B.; Ortiz, J. V.; Cioslowski, J.; Fox, D. J. Gaussian 09, Revision A. 02, Gaussian, Inc.: Wallingford, CT, USA, 2009.

111 Noodleman, L. *J. Am. Chem. Soc.* **1981**, *74*, 5737-5743.

112 Christian, P.; Rajaraman, G.; Harrison, A.; Helliwell, M.; McDouall, J. J. W.; Raftery, J.; Winpenny, R. E. P. *Dalton Trans.* **2004**, 2550-2555.

113 Ruiz, E.; Cano, J.; Alvarez, S.; Caneschi, A.; Gatteschi, D. *J. Am. Chem. Soc.* **2003**, *125*, 6791-6794.

114 Berg, N.; Hooper, T. N.; Liu, J.; Beedle, C. C.; Singh, S. K.; Rajaraman, G.; Piligkos, S.; Hill, S.; Brechin, E. K.; Jones, L. F. *Dalton Trans.* **2013**, *42*, 207-216.

115 Rajaraman, G.; Murugesu, M.; Sanudo, E. C.; Soler, M.; Wernsdorfer, W.; Helliwell, M.; Muryn, C.; Raftery, J.; Teat, S. J.; Christou, G.; Brechin, E. K. *J. Am. Chem. Soc.* **2004**, *126*, 15445-15457.

116 Fohlmeister, L.; Vignesh, K. R.; Winter, F.; Moubaraki, B.; Rajaraman, G.; Pöttgen, R.; Murray, K. S.; Jones, C. *Dalton Trans.* **2015**, *44*, 1700-1708.

117 Singh, S. K.; Vignesh, K. R.; Archana, V.; Rajaraman, G. *Dalton Trans.* **2016**, *45*, 8201-8214.

118 Cremades, E.; Cano, J.; Ruiz, E.; Rajaraman, G.; Milios, C. J.; Brechin, E. K. *Inorg. Chem.* **2009**, *48*, 8012-8019.

119 Vignesh, K. R.; Langley, S. K.; Murray, K. S.; Rajaraman, G. *Chem. Eur. J.* **2015**, *21*, 2881-2892.

120 Neese, F. *Wiley Interdisciplinary Reviews: Computational Molecular Science* **2012**, *2*, 73-78.

121 Harris, T. D.; Bennett, M. V.; Clérac, R.; Long, J. R. *J. Am. Chem. Soc.* **2010**, *132*, 3980-3988.

122 Ohkoshi, S.-i.; Hashimoto, K. *Journal of Photochemistry and Photobiology C: Photochemistry Reviews* **2001**, *2*, 71-88.

123 Rombaut, G.; Verelst, M.; Golhen, S.; Ouahab, L.; Mathonière, C.; Kahn, O. *Inorg. Chem.* **2001**, *40*, 1151-1159.

124 Herrera, J. M.; Marvaud, V.; Verdaguer, M.; Marrot, J.; Kalisz, M.; Mathonière, C. *Angew. Chem. Int. Ed.* **2004**, *43*, 5468-5471.

125 Hozumi, T.; Hashimoto, K.; Ohkoshi, S.-i. *J. Am. Chem. Soc.* **2005**, *127*, 3864-3869.

126 Ohkoshi, S.-i.; Tokoro, H. *Acc. Chem. Res.* **2012**, *45*, 1749-1758.

127 Palii, A. V.; Reu, O. S.; Ostrovsky, S. M.; Klokishner, S. I.; Tsukerblat, B. S.; Hilfiger, M.; Shatruk, M.; Prosvirin, A.; Dunbar, K. R. *J. Phys. Chem. A.* **2009**, *113*, 6886-6890.

128 Wang, X.-Y.; Hilfiger, M. G.; Prosvirin, A.; Dunbar, K. R. *Chem. Commun.* **2010**, *46*, 4484-4486.

129 Saber, M. R.; Dunbar, K. R. *Chem. Commun.* **2014**, *50*, 2177-2179.

130 Holt, D. G. L.; Larkworthy, L. F.; Povey, D. C.; Smith, G. W.; Jeffery Leigh, G. *Inorg. Chim. Acta.* **1990**, *169*, 201-205.

131 Cissell, J. A.; Kaur, N.; Nellutla, S.; Dalal, N. S.; Vaid, T. P. *Inorg. Chem.* **2007**, *46*, 9672-9677.

132 Luo, H.-Y.; Zhou, J.; Zou, H.-H. *Dalton Trans.* **2019**, *48*, 3090-3097.

133 Khan, M. I.; Chang, Y.-D.; Chen, Q.; Salta, J.; Lee, Y.-S.; O'Connor, C. J.; Zubieta, J. *Inorg. Chem.* **1994**, *33*, 6340-6350.

134 Mokry, L. M.; Thompson, J.; Bond, M. R.; Otieno, T.; Mohan, M.; Carrano, C. J. *Inorg. Chem.* **1994**, *33*, 2705-2706.

135 Yang, W.; Lu, C. *Inorg. Chem.* **2002**, *41*, 5638-5640.

136 Brouca-Cabarrecq, C.; Mohanu, A.; Millet, P.; Trombe, J. C. *Journal of Solid State Chemistry* **2004**, *177*, 2575-2583.